TECHNISCHE UNIVERSITÄT MÜNCHEN

Fakultät für Informatik
I-16 / Computer Aided Medical Procedures

Improving Reconstruction of Dynamic PET Imaging by Utilizing Temporal Coherence and Pharmacokinetics

Xiaoyin Cheng

Vollständiger Abdruck der von der Fakultät für Informatik der Technischen Universität München zur Erlangung des akademischen Grades eines

Doktors der Naturwissenschaften (Dr. rer. nat.)

genehmigten Dissertation.

Vorsitzender: Univ.-Prof. Dr. K. A. Kuhn

Prüfer der Dissertation:
1. Univ.-Prof. Dr. N. Navab
2. apl. Prof. Dr. S. Ziegler
3. Lecturer Dr. C. Tsoumpas
   University of Leeds

Die Dissertation wurde am 19.12.2014 bei der Technischen Universität München eingereicht und durch die Fakultät für Informatik am 15.05.2015 angenommen.

Abstract

Positron emission tomography (PET) has contributed greatly to the medicine field over the last decade, since it provides bio-functional information in vivo which can improve clinical diagnosis and treatment management. In contrast to a static scan, dynamic PET offers us an opportunity to understand the evolution of a radioactive tracer, analyze the underlying pharmacokinetics and quantitatively estimate corresponding physiologies from reconstructed images. However, the reconstruction quality is often limited by the low signal-to-noise (SNR) ratio of PET acquisitions. The frame-by-frame estimation of dynamic PET images suffers from inconsistent SNR and poor reconstruction quality.

This thesis focuses on the development and validation of dynamic PET reconstruction. It explores the integration of temporal coherence and tracer pharmacokinetics to reduce reconstruction artifacts and enhance image quality. The impact on physiological quantification resulting from these improvements in reconstruction is investigated as well.

Due to finite acquisition angles, a streak artifact typically appears in filtered back projection (FBP) reconstructed images. The strong streak artifact due to extremely high signals usually affects anatomical identification and clinical diagnosis. This thesis has proposed a framework based on the temporal coherence of PET measurements for artifact reduction. The framework was evaluated using realistic simulations as well as a physical phantom. Clear improvements in artifact reduction and quantitative analysis were observed in the corrected images.

The limited SNR of PET acquisitions hampers the development of simultaneous multi-tracer PET imaging. Though tracer separation is feasible by exploring its distinct pharmacokinetics, the quantification accuracy is affected when a multi-tracer kinetic model with a large number of fitting parameters is adopted. In this thesis, an algorithm has been proposed for tracer separation, which integrates the multi-tracer model in reduced parameter space into the reconstruction. Evaluations were performed for validating the algorithm using numerical phantoms as well as preclinical PET data. Enhanced reconstruction and reliable recovery of individual tracer components were observed.

A better estimation of PET images can be achieved when additional temporal information is incorporated into reconstruction. However, whether these improvements in reconstruction can give additional value to physiological quantification is

not yet clear. In this thesis, preclinical PET images generated with/without the incorporation of temporal information were compared with a biological reference. Evaluation results demonstrate that the reconstruction combining temporal data leads to a better quantification of tumor physiology.

Overall, this thesis utilizes temporal coherence and tracer pharmacokinetics to cope with image reconstruction for improving PET quantification. The temporal information was used to reduce streak artifacts and to achieve simultaneous spatial-temporal reconstruction for SNR optimization. In particular, this thesis has confirmed that improvements in reconstruction can enhance PET quantification of pathological features and have the potential to improve clinical diagnosis.

Zusammenfassung

Die Positronen-Emissions-Tomographie (PET) hat im medizinischen Fachgebiet besonders dazu beigetragen, dass in den letzten 10 Jahren, seit sie bio-funktionelle Informationen in vivo zur Verfügung stellt, die klinische Diagnostik und das Behandlungsmanagement verbessert werden konnten. Im Gegensatz zum statischen Scannen bietet uns das dynamische PET die Gelegenheit, die Entwicklung eines radioaktiven Tracer nachzuvollziehen, die zugrunde liegende Pharmakokinetik zu analysieren und entsprechende Physiologien anhand der rekonstruierten Bilder quantitativ einzuschätzen. Allerdings ist die Rekonstruktionsqualität oft aufgrund des niedrigen Signal-Rausch-Verhältnisses (signal-to-noise-ratio: SNR) der PET Aufnahmen begrenzt. Die Bild-basierte der dynamische PET-Analyse leidet an inkonsistentem SNR und mangelhafter Rekonstruktionsqualität.

Diese Arbeit konzentriert sich auf die Entwicklung und Überprüfung der dynamischen PET-Rekonstruktion. Sie erforscht die Integration der temporalen Kohärenz und Tracer-Pharmakokinetik, um die Rekonstruktionsartefakte zu reduzieren und die Bildqualität zu verbessern. Außerdem ist die Auswirkung auf die physiologische Quantifizierung, die sich aus den Verbesserungen in der Rekonstruktion ergeben hat, untersucht worden.

Infolge von begrenzten Messwinkeln erscheint normalerweise ein Streifen in den rekonstruierten Bildern als Störung in der gefilterten Rückprojektion (FBP). Der große Streifenartefakt beeinflusst aufgrund von extrem hohen Signalen im Normalfall die anatomische Identifizierung und die klinische Diagnose. Die Verfasserin dieser Arbeit hat ein Rahmenwerk vorgeschlagen, das auf der temporalen Kohärenz der PET-Messungen für die Verminderung der Artefakte basiert. Das Rahmenwerk wurde sowohl mit realistischen Simulationen als auch mit physikalischen Phantomen ausgewertet. In den korrigierten Bildern sind klare Verbesserungen in der Reduzierung der Artefakte und der quantitativen Analyse beobachtet worden.

Die begrenzte SNR der PET-Messungen erschwert die Entwicklung der simultanen Multi-Tracer-PET-Bildgebung. Obwohl die Trennung der Tracer aufgrund ihrer ausgeprägten Pharmakokinetik durchführbar ist, ist die Genauigkeit der Quantifizierung betroffen, wenn ein kinetisches Multi-Tracer-Modell mit einer hohen Anzahl an zu bestimmenden Parametern angenommen worden ist. In dieser Arbeit wurde ein Algorithmus für die Tracer-Trennung vorgeschlagen, welcher das Multi-Tracer-Modell im reduzierten Parameter-Raum in die Rekonstruktion integriert hat.

Die Berechnungen für die Bewertung der Algorithmen wurden sowohl mit numerischen Phantomen als auch mit präklinischen PET-Daten durchgeführt. Eine verbesserte Rekonstruktion und zuverlässige Wiederherstellung der individuellen Tracer Komponenten wurde beobachtet.

Eine bessere Beurteilung der PET-Bilder kann dadurch erreicht werden, wenn zusätzliche temporale Information in die Rekonstruktion eingebunden wird. Jedoch, ob Verbesserungen in der Rekonstruktion einen zusätzlichen Wert für die physiologische Quantifizierung geben können, ist noch nicht klar. In dieser Arbeit wurden präklinische PET-Bilder, mit bzw. ohne die Einbindung der temporalen Information erzeugt, mit einer biologischen Referenz verglichen. Die Bewertungsergebnisse demonstrieren, dass die Rekonstruktion, verbunden mit temporalen Daten, zu einer besseren Quantifizierung der Tumorphysiologie führt.

In dieser Arbeit werden temporale Kohärenz und Tracer-Pharmakokinetik verwendet, um die Bildrekonstruktion und gleichzeitig die Quantifizierung zu verbessen. Temporale Information wurde benutzt, um Streifenartefakte zu reduzieren und simultane sowie räumlich-temporale Rekonstruktion verbesserte das Bildtauschen. Im Besonderen bestätigt diese Arbeit, dass Verbesserungen in der Rekonstruktion Merkmale aufwerten können und das Potenzial haben, klinische Diagnosen zu unterstützen.

Acknowledgements

Last four years in München were a bittersweet symphony for me. Sometimes it was blue, but more often it was cool. This unique piece, the co-composers, and the performers who made the performance a success etch in my memory that shall never fade away. Here I would like to take this opportunity to express my deepest gratitude to those who have enabled me to accomplish this work with their continuously supports, patience, guidance and encouragements.

I want to express my respects and gratitude to my supervisors, Prof. Dr. Sibylle Ziegler and Prof. Dr. Nassir Navab. Thank you Sibylle, for giving me the opportunity to be a member of nuclear medicine, for your constant support, kind directions and suggestions, and for all the valuable insights that you shared with me, from which I learn and benefit a lot. Thank you Nassir, for giving me the chance to participate in different kinds of interesting academic activities, where I can exchange my experiences and learn from others.

I'm very grateful to my mentor Dr. Kuangyu Shi. Thank you for taking me into the field of nuclear medicine, for your very patient guidance, friendly communications, and timely advices throughout the whole period of my study. Thank you for everything you did for me. It has been a pleasure to cooperate with you. Your aspiration, creativity and diligence in work always motivate me. Thank you also for trusting and supporting me to try out crazy ideas and always inspiring me with your unique insights.

I would also like to thank all the colleague at the nuclear medicine department for their unconditional advices and assistance. In particular, I want to thank Qian Wang, Zhen Liu, Jakob Vogel and Yuxiang Chen for the delightfully discussions and collaborations. I also want to express my respects to Sybille Reder, Marco Lehmann and Markus Mittelhäusen for their professional work and continuous help.

Last but not the least, I would like to thank my father and mother for supporting me to chase my dream career aboard, teaching me to be optimistic and independent, and making me brave in the face of difficulties and frustrations. I want to especially thank my husband Bohao for always being my stress reliever and always being tolerant to my bad mood. I also want to thank Wentao Song, Shulei Zhu, Ying Luan and all the friends for the joyful time we spent together.

List of Symbols

Symbol	Quantity	Dimension
α	Attenuation correction factor	$N_{LOR} \times 1$
β	Regularization constant	1×1
λ	Radioactivity decay constant	1×1
μ	Attenuation coefficients	1×1
C	Radioactive concentration in tissue (Time activity curve, or TAC)	$N_T \times 1$
$\hat{C}$	Modeled time activity curve	$N_T \times 1$
$\hat{C}_P$	Radioactivity concentration in whole blood (Arterial input function, or AIF)	$N_T \times 1$
$\mathbf{k}$	Tracer exchange rates between compartments	$N_K \times 1$
V_B	Fractional blood volume	1×1
$\mathbf{p}$	Kinetic parameters, containing $\mathbf{k}$ and V_B	$(N_K + 1) \times 1$
$\mathbf{w}$	Weighting factors	$N_T \times 1$
i	Index of lines-of-response (LORs)	1×1
j	Index of voxels	1×1
k	Index of kinetic parameters	1×1
t	Index of frames/measured time points	1×1
I	Set of LORs	1×1
I_j	Set of LORs across the j^{th} voxel	1×1
J	Set of voxels	1×1
J_i	Set of voxels relevant to the i^{th} LOR	1×1
N_{LOR}	Number of LORs	1×1
N_T	Number of frames / time points	1×1
N_{vox}	Number of image voxels	1×1
N_K	Number of kinetic parameters	1×1
$\mathbf{A} = \{a_{ij}\}$	System matrix	$N_{LOR} \times N_{vox}$
$\mathbf{P} = \{p_{jk}\}$	Parametric images	$N_{vox} \times N_K$
$\mathbf{X} = \{x_{jt}\}$	True tracer activity distribution	$N_{vox} \times N_T$
$\hat{\mathbf{X}} = \{\hat{x}_{jt}\}$	Modeled tracer activity distribution	$N_{vox} \times N_T$
$\mathbf{Y} = \{y_{it}\}$	Projection data; PET measurements	$N_{LOR} \times N_T$
$\mathbf{Y} = \{y_{it}\}$	Modeled projection data	$N_{LOR} \times N_T$
$\mathbf{R} = \{r_{it}\}$	Random events	$N_{LOR} \times N_T$
$\mathbf{S} = \{s_{it}\}$	Scattered events	$N_{LOR} \times N_T$

Contents

1

Introduction

1.1 Positron Emission Tomography

Positron emission tomography (PET) is a nuclear medicine imaging technique [1]. Differing from computed tomography (CT) or magnetic resonance imaging (MRI) for acquiring anatomical information, PET utilizes injected radioactive isotopes (tracers) to acquire the underlying biological and functional information *in vivo*.

The procedure of PET imaging is sketched in Fig. 1.1. Before the patient is imaged, a radioactive tracer is administrated. As the tracer circulates with the blood, it may concentrate and chemically incorporate into the tissue "regions of interest" (ROIs). During the interaction procedure, a series of physical reactions occur: the radioisotope undergoes beta decay and generates positron particles, which immediately annihilate electrons within a short distance [2]. In theory, the annihilation produces a pair of photons with the same energy ($\sim$511 KeV) traveling in the opposite directions along a line (called the "line-of-response", or LOR). It may be detected by the PET scanner as a true coincident event (or a coincidence) and 1 count at a certain LOR is recorded. As photon pairs are continuously detected during the emission scan, the number of events accumulates. In the end, PET measures the count of coincident events per time unit per volume, at each detector pair (LOR) [3]. With this information, PET images that reflect the radioactivity distribution[1] within the patient can be generated using proper reconstruction methods [4–8].

Photon information can be grouped into a "sinogram". This format characterizes a LOR by its viewing angle θ and distance d to the center. As plotted in Fig. 1.2a, when the point source within the patient is detected at the LOR of the angle θ_0 and the distance d_0, the corresponding count rate of coincident events at this LOR is recorded at the point (θ_0, d_0) in the sinogram coordinate system. As the point source is imaged from all angles, a sine-shape curve is formed in the sinogram image

[1]The PET image has a unit of becquerel/ml (or Bq/ml). One Bq is defined as one radioactive decay per second.

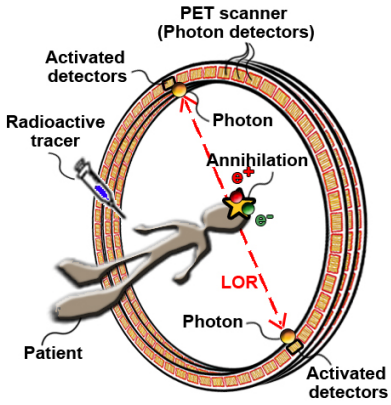

Figure 1.1: A sketch of the PET scan procedure

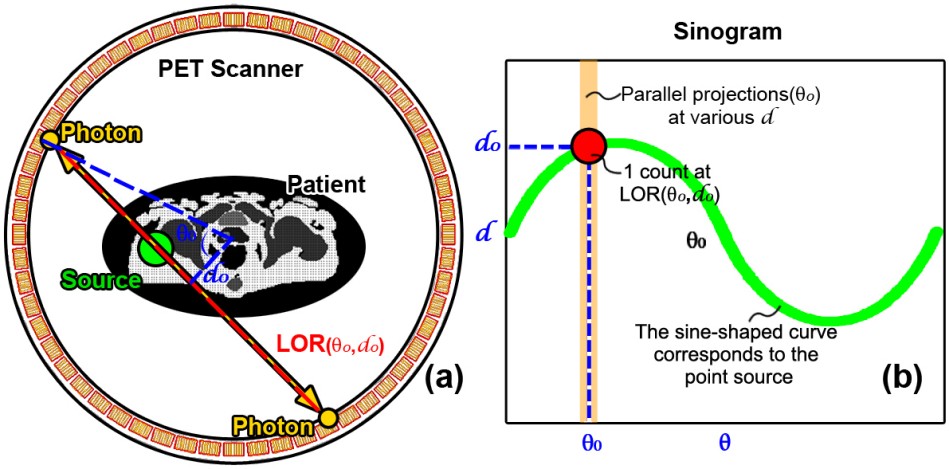

Figure 1.2: Sketches of (a) the coincident event from a point source detected at a line-of-response (LOR) and (b) the sinogram image corresponding to the source

as shown in Fig. 1.2b. Therefore this format for storing data is named as the sinogram. In practice, a tracer is normally uptaken by the whole body of the patient. The body image is discretized into fine voxels, each of which can approximate a point source. By imaging all these sources, the sine-shaped curves for each voxel are added and make up the final sinogram corresponding to the whole body image. From another point of view, the sinogram coordinate system is also termed "the projection space". As a viewing angle θ_0 is specified, the counts at various d form a parallel projection of the source signal along this angle, and the whole sinogram consists of sets of parallel projections at each angle (0-180°). PET image reconstruction can be

achieved based on either the LOR measurements or the sinogram data. This thesis focuses on the latter which is commonly used in the clinic.

In practice, the signal-to-noise (SNR) ratio of a PET measurement is often affected by several physical effects. Besides the true coincidences (Fig. 1.3a), other types of coincident events also occur during PET imaging. For instance, a "scattered event" (Fig. 1.3b) arises when one or both of the photons from a single positron annihilation is scattered by the patient. A "random event" (Fig. 1.3c) takes place when two photons originating from different annihilations are detected as a true coincidence. These events lead to incorrect estimations of LORs and adds statistical noise into PET measurements [9–11]. An accurate measurement of the scattered and random events is challenging. Nowadays, these effects are often modeled from the measurements or simulations of PET and CT [12–16].

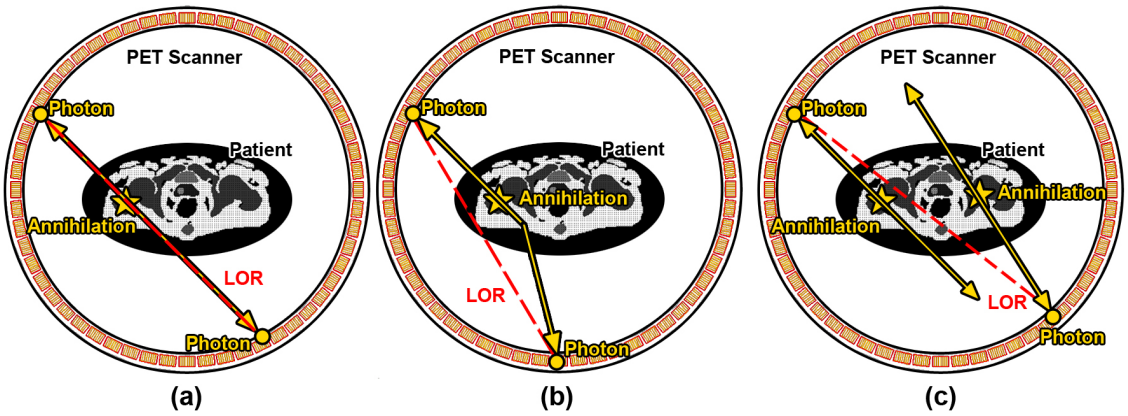

Figure 1.3: Sketches showing different types of coincident events: (a)a true event; (b)a scattered event and (c)a random event

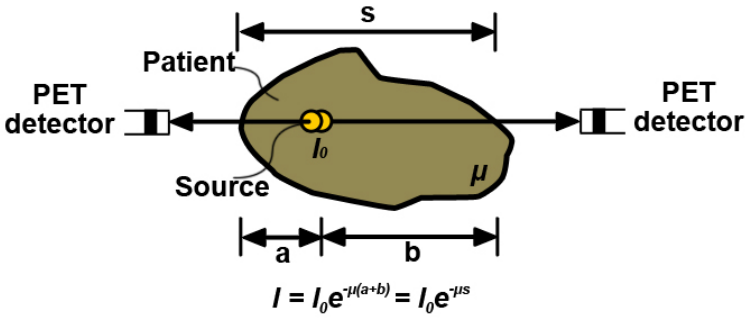

Figure 1.4: A sketch of the attenuation effect

On the other hand, the PET signal is attenuated during the acquisition process. As the photon beam interacts with the patient, its intensity is reduced by scattering and absorption, resulting in a reduced count rate of events [3]. As shown in Fig 1.4, the extent of attenuation depends on the "attenuation coefficient" (μ, unit: cm^{-1}) of a certain material and the total thickness of the attenuator where the photon pair passes through. Attenuation correction is often required in clinical practice. Given the attenuated signal I, the original signal intensity I_0 can be recovered when the corresponding μ-map of the imaged patient is provided [17–20].

The application of PET in the clinic is being promoted by the fast development of radioactive tracers. Each tracer is designed to investigate a distinct aspect of the tumor phenotype and to acquire specific physiological and diagnostic information of living organisms. For instance, [^{18}F]Fluordeoxyglucose (FDG) is used in daily practice to show the glucose metabolism *in vivo*, which enhances the diagnosis of tumor and neurodegenerative diseases [21]. 3'-[^{18}F]fluoro-3'-deoxythymidine (FLT) is employed for imaging cell proliferations and it exhibits a relatively higher tumor specificity than [^{18}F]FDG [22]. [^{18}F]Fluoromisonidazole (FMISO) is designed to be trapped in tissues with a low oxygenation level to detect tumor hypoxia [23]. [^{11}C]L-methionine (MET) can be applied as for imaging glioma [24].

1.2 PET Image Reconstruction

Medical image reconstruction is a technique to estimate the tomographic image of the patient from data measured using medical scanners. From the mathematical point of view, image reconstruction techniques aim to solve an inverse problem, which is, from the observations (or acquisitions) $\mathbf{Y}$, to compute the source $\mathbf{X}$ that most likely leads to such observations. For PET applications, $\mathbf{Y}$ includes the count rate of coincident events and $\mathbf{X}$ is the distribution of radioactivity in the patient. The estimation of $\mathbf{X}$ can be achieved using an analytical method or iterative techniques [4,25]. The main difference between these two categories is the mathematical model used for mapping the source $\mathbf{X}$ to the acquisition $\mathbf{Y}$.

1.2.1 Analytical reconstruction

1.2.1.1 The Radon transform

Conventionally, the detection of photon pairs in PET naturally leads to a line-integral model for estimating the acquisition $\mathbf{Y}$ at each LOR from the source $\mathbf{X}$. The model is based on the assumption that the total count of coincidences at a LOR is proportional to the integral of the source density along this LOR. When $\mathbf{Y}$ is considered as parallel projections, the model is given by the Radon transform [7]:

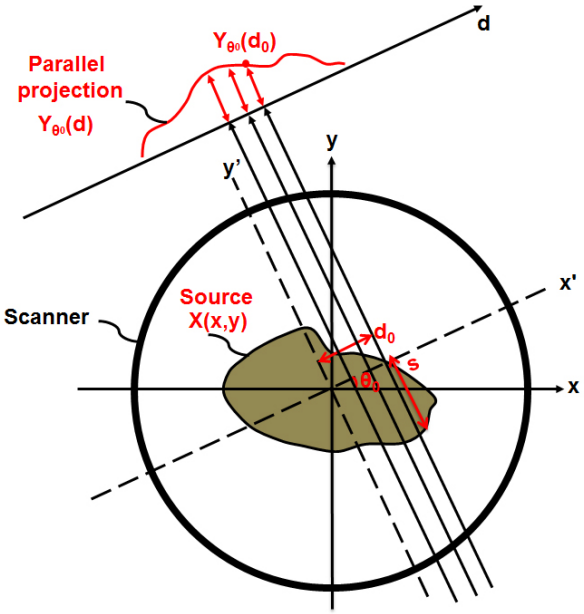

Figure 1.5: A sketch illustrating the Radon transform

$$\mathbf{Y}_\theta(d) = \int_{(\theta,d)line} \mathbf{X}(x,y)ds = \int_{-\infty}^{\infty}\int_{-\infty}^{\infty} \mathbf{X}(x,y)\delta(xcos\theta + ysin\theta - d)dxdy \quad (1.1)$$

where δ is the Dirac delta function, which is used to retrieve the projection at a certain d.

As illustrated in Fig. 1.5, the value of the point $\mathbf{Y}_{\theta_0}(d_0)$ in the projection space is modeled as the line integral of $\mathbf{X}$ along the straight line s specified by the corresponding θ_0 and d_0 in the image space.

With the relationship between the acquisition and source (captured in Eqn. 1.1), PET images can be reconstructed using analytic inversion methods. Among these methods, the filtered back projection (FBP) algorithm achieves accurate reconstruction with high efficiency and is routinely used in clinical practice.

1.2.1.2 Filtered back projection

FBP was developed based on the Fourier slice theorem [25], which states that the Fourier transformation of a parallel projection of the source at a specified viewing angle, gives values of a slice of the 2D Fourier transformation of the source at this angle. Mathematically, it is expressed as:

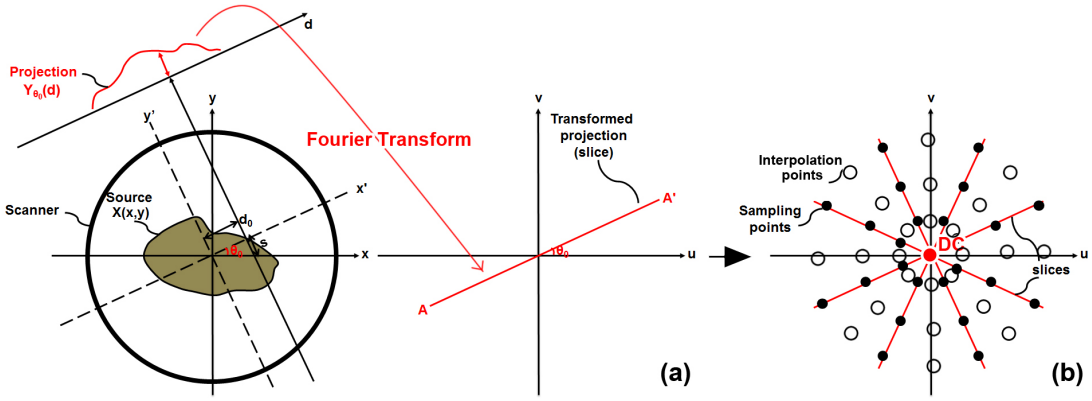

Figure 1.6: Sketches (a) explaining the Fourier slice theorem: the Fourier transformation of the parallel projection $\mathbf{Y}_{\theta_0}(d)$ gives the value of the slice AA', which is a slice of the 2D Fourier transformation of the source; (b) showing slices at different viewing angles and the numerical interpolation points for estimating gaps in between slices

$$\begin{aligned} S_\theta(w) &= \int_{-\infty}^{\infty} \mathbf{Y}_\theta(d) e^{-j2\pi wd} d(d) \\ F(u,v) = F(wcos\theta, wsin\theta) &= \int_{-\infty}^{\infty}\int_{-\infty}^{\infty} \mathbf{X}(x,y) e^{-j2\pi w(xcos\theta, ysin\theta)} dxdy \\ S_\theta(w) &= F(u,v) \end{aligned} \tag{1.2}$$

where $S_\theta(w)$ is the 1D Fourier transformation of the parallel projection $\mathbf{Y}_\theta(d)$ at an angle θ, and $F(u,v)$ is the 2D Fourier transformation of the source $\mathbf{X}(x,y)$ at the same angle θ.

Therefore, by transforming a parallel projection at a certain angle, values of $F(u,v)$ in the frequency space can be partially recovered as a slice, as illustrated in Fig. 1.6a. With an infinite number of parallel projections, the estimated source image $\hat{\mathbf{X}}(x,y)$ can be accurately recovered by directly calculating the inverse 2D Fourier transform of $F(u,v)$. In practice, the number of projections is limited. Thus numerical interpolation is required to fill the gaps between slices as shown in Fig. 1.6b. However, radial points get sparser as one gets farther away from the center of $F(u,v)$, and larger errors are introduced to $\hat{\mathbf{X}}$'s components at higher frequencies.

Based on the projection model and the theorem, FBP was developed to achieve faster and more accurate reconstruction than the interpolation methods [25]. As shown in Fig. 1.6b, all slices in the Fourier space are independent of each other except for the common DC (or direct current) component. This enables FBP to employ a filter on individual slice assuming other slices are zero and inversely transforms the nonzero slice back to the image space. This filter is defined as $2\pi|w|N_a$ (where N_a is the number of projections), resulting in a filtered slice $(2\pi|w|N_a)S_\theta(w)$ of the

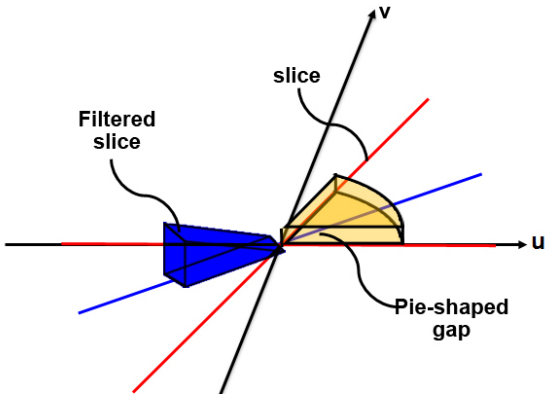

Figure 1.7: A sketch showing the effect of using the filter which results in the filtered slice having the same "mass" as the pie-shape gap between slices

same "mass" as the pie-shaped gap in between the two adjacent slices (shown in Fig. 1.7). This approximation of the gap has been proved to be more accurate than the approximation using interpolation methods [25]. With the filtered slice, "the filtered projection" $Q_\theta(d)$ is calculated by using the inverse Fourier transform:

$$Q_\theta(d) = \int_{-\infty}^{\infty} S_\theta(w)|w|e^{j2\pi wt}dw \tag{1.3}$$

The reconstruction of filtered projections from the projection space to the image space is a *back projection* procedure [25], as described in Eqn. 1.4:

$$\hat{\mathbf{X}}(x,y) = \int_0^{\pi} Q_\theta(xcos\theta + ysin\theta)d\theta \tag{1.4}$$

During the back projection procedure, $Q_{\theta_0}(d)$ equally spread back over the image plane. For instance, as shown in Fig. 1.8, the intensity of the point $Q_{\theta_0}(d_0)$ is equally divided across all points (x, y) on the line MN. The final FBP image is the summation of all the image planes reconstructed from the filtered projections acquired at all viewing angles.

FBP has gained its reputation in tomographic reconstruction mainly owing to its high efficiency [26], which is achieved by the analytical calculation of images from the projection data. Especially for the applications using CT (or PET/CT in the nuclear medicine area), which measures projection data angle by angle, the efficiency of reconstruction can be further improved. As FBP is employed each time for a single projection, it enables reconstruction as soon as a projection (at a certain angle) is acquired and can therefore be applied during a CT measurement.

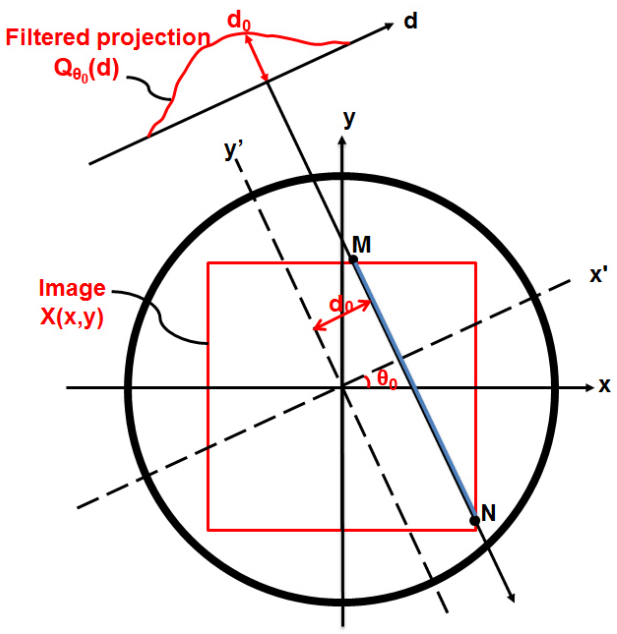

Figure 1.8: A sketch explaining the back projection procedure

1.2.2 Iterative methods

1.2.2.1 The system matrix

Though the analytical methods normally result in effective reconstruction, the image quality is limited by using the fixed line-integral model. The model does not take account of the statistical variations inherent in PET acquisitions, and may not be accurate enough to describe the physical effects in the photon detection procedure.

Alternatively, the iterative methods relates the acquisition $\mathbf{Y}$ with the source $\mathbf{X}$ through a linear model (or "the system matrix") $\mathbf{A}$:

$$\mathbf{Y} = \mathbf{AX} \tag{1.5}$$

where $\mathbf{Y} = \{y_i\} \in \mathbb{R}^{N_{LOR}}$, $\mathbf{X} = \{x_j\} \in \mathbb{R}^{N_{vox}}$, and $\mathbf{A} = \{a_{ij}\} \in \mathbb{R}^{N_{LOR} \times N_{vox}}$; N_{LOR} is the total number of LORs and N_{vox} is the number of voxels.

The idea behind iterative methods is rather intuitive. Eqn. 1.5 presents a *forward projection* process: given the initial estimation $\hat{\mathbf{X}}^{(0)} = \{\hat{x}_j^{(0)}\}$ and the system matrix $\mathbf{A}$, $\mathbf{Y}$ can be modeled from Eqn. 1.5. By comparing the modeled projection $\hat{\mathbf{Y}}^{(0)} = \{\hat{y}_i^{(0)}\}$ and the real measurement $\mathbf{Y}$, $\hat{\mathbf{X}}$ is reversely adjusted (*backward projection*). The updated estimation $\hat{\mathbf{X}}^{(1)}$ is used in the next iteration to calculate $\hat{\mathbf{Y}}^{(1)}$ for the comparison. Convergence is reached when the difference between $\mathbf{Y}$ and $\hat{\mathbf{Y}}$ is reduced to an acceptable level, and $\hat{\mathbf{X}}^{(n)}$ is considered the best approximation of $\mathbf{X}$.

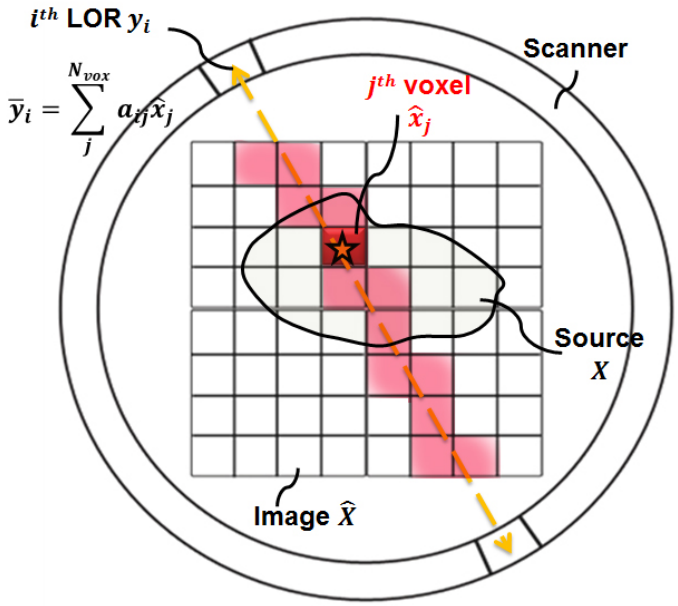

Figure 1.9: A sketch showing the photon emission and detection processes

To achieve a modeled projection $\hat{\mathbf{Y}}$ that can best resemble the real acquisition, the matrix $\mathbf{A}$ is desired to be as realistic as possible. Generally, $\mathbf{A}$ models the probability of a photon emission from the a certain image voxel being detected by a certain LOR, based on the geometric information of the PET scanner. Particularly, in order to handle the statistical variations in the photon emission process, the system matrix has been developed to include the noise model of the PET data, which is normally considered to have a Poisson distribution, using a maximum-likelihood (ML) method [27]. Detailed discussions are given below.

As illustrated in Fig. 1.9, it is assumed that a photon originating from the j^{th} voxel has a Bernoulli distribution and the average emission rate is $\hat{x}_j$ within a unit time interval. Then photons arising from the j^{th} voxel have a Poisson distribution with the expectation $\bar{x}_j$ [28]. It should be noted that $\bar{\mathbf{X}} = \{\bar{x}_j\}$ and $\hat{\mathbf{X}}$ are equivalent, since the image of the expected photo emission rate (or the count rate of the coincidences, or radioactivity) of the source is exactly the image that needs to be reconstructed. Therefore, $\bar{\mathbf{X}}$ is used instead of $\hat{\mathbf{X}}$ throughout this section. Given the probability a_{ij} for an emission from the j^{th} voxel being detected by the i^{th} LOR, the measurement y_i also has a Poisson distribution with the expectation $\bar{y}_i$, which is equivalent to the total count rate of all voxels across the i^{th} LOR [28]:

$$\begin{aligned} Pr(y_i|\bar{x}) &\sim Poisson(\textstyle\sum_{j\in J_i}^{N_{vox}} a_{ij}\bar{x}_j) \\ y_i &= e^{-\bar{y}_i}(\bar{y}_i)^{y_i}/(y_i!) \\ \bar{y}_i &= \textstyle\sum_{j\in J_i}^{N_{vox}} a_{ij}\hat{x}_j \end{aligned} \tag{1.6}$$

where J_i denotes the set of image voxels that are crossed by the i^{th} LOR (red voxels in Fig. 1.9).

Eqn. 1.6 gives the conditional probability (or the likelihood function) $Pr(y_i|\bar{x})$ at the i^{th} LOR, and the conditional probability with respect to all LORs is given by $Pr(\mathbf{Y}|\bar{\mathbf{X}}) = \prod_i (Pr(y_i|\bar{x}))$. The best approximation $\bar{\mathbf{X}}$ of the source is considered the one that maximizes the likelihood $Pr(\mathbf{Y}|\bar{\mathbf{X}})$, or maximizes the equivalent log-likelihood function of $Pr(\mathbf{Y}|\bar{\mathbf{X}})$, which is expressed as:

$$\mathcal{LL}(\bar{\mathbf{X}}|\mathbf{Y}) = \ln(Pr(\mathbf{Y}|\bar{\mathbf{X}})) = \sum_i^{N_{LOR}} [y_i \ln(\sum_j^{N_{vox}} a_{ij}\bar{x}_j) - \sum_j^{N_{vox}} a_{ij}\bar{x}_j - \ln(y_i!)] \tag{1.7}$$

where $\mathcal{LL}$ denotes the log-likelihood function and ln is the natural logarithm.

1.2.2.2 Maximum likelihood expectation maximization

The maximization of the first ln term in Eqn. 1.7 with respect to $\bar{x}_j$ is challenging. Expectation Maximization (EM) is a general approach to solve the ML problem [29]. This approach has been adopted for iterative PET image reconstruction, and is known as the "Maximum likelihood expectation maximization (MLEM)" reconstruction [4, 30, 31].

In general, EM consists of an "expectation-step (E-step)" and a "maximization-step (M-step)". In the E-step, this approach introduces a set of "complete data", which simplifies the likelihood function and make the ML problem solvable. Then the M-step is used to iteratively optimize the expectation of the simplified likelihood function. Detailed discussions are given below.

E-Step (expectation-step): The condition $\mathbf{Y}$ in Eqn. 1.7 is considered the "incomplete data set" as it only provides the information of the number of counts of coincidences at a certain LOR but no knowledge of the origins of photon pairs. Therefore, in the E-step, a complete data set $\mathbf{X} = \{x_{ij}\}$ is introduced, which includes information of the origins (the j^{th} voxel) as well as the destinations (the i^{th} LOR) of detected photon pairs. With $\mathbf{X}$, a log-likelihood function that is easier to optimize is then constructed:

$$\mathcal{LL}(\bar{\mathbf{X}}|\mathbf{X}) = \ln(Pr(\mathbf{X}|\bar{\mathbf{X}})) = \sum_i^{N_{LOR}} \sum_{j\in J_i} [-a_{ij}\bar{x}_j + x_{ij} \ln(a_{ij}\bar{x}_j) - \ln(x_{ij}!)] \tag{1.8}$$

Given $\mathbf{Y}$ and current estimation $\bar{\mathbf{X}}^{(n)}$, the expectation of $\mathcal{LL}(\bar{\mathbf{X}}|\mathbf{X})$ with respect to x_{ij} is deduced:

$$E(\mathcal{LL}(\bar{\mathbf{X}}|\mathbf{X})|\mathbf{Y},\bar{\mathbf{X}}^{(n)}) = \sum_{i}^{N_{LOR}} \sum_{j\in J_i} [-a_{ij}\bar{x}_j + \ln(a_{ij}\bar{x}_j)\frac{a_{ij}\bar{x}_j^{(n)}y_i}{\sum_{l\in J_i} a_{il}\bar{x}_l^{(n)}}] + Constant \quad (1.9)$$

where the constant term which is irrelevant to $\bar{\mathbf{X}}$ is omitted during the optimization.

M-Step (maximization/minimization-step): To optimize Eqn 1.9, the partial derivative of the function in regard to each image voxel $\bar{x}_j$ is calculated and set to zero:

$$\frac{\partial E(\mathcal{LL}(\bar{\mathbf{X}}|\mathbf{X})|\mathbf{Y},\bar{\mathbf{X}}^{(n)})}{\partial \bar{x}_j} = 0 \quad (1.10)$$

Eqn. 1.10 deduces a closed-form update function for estimating $\bar{\mathbf{X}}$ at each iteration:

$$\bar{x}_j^{(n+1)} = \frac{\bar{x}_j^{(n)}}{\sum_{i\in I_j} a_{ij}} \sum_{i\in I_j} a_{ij} \frac{y_i}{\sum_{l\in J_i} a_{il}\bar{x}_l^{(n)}} \quad (1.11)$$

where I_j denotes the set of LORs crossing the j^{th} voxel.

Eqn. 1.11 can be explained explicitly. $\sum_{l\in J_i} a_{il}\bar{x}_l^{(n)}$ represents the forward projection procedure to model y_i. By comparing the model to measurements, a ratio sinogram $(\frac{y_i}{\hat{y}_i})$ is acquired and back projected to the image space by inner multiplying with a_{ij}, resulting in a ratio image to update the current estimation $\bar{x}_j^{(n)}$ [4]. $\sum_{i\in I_j} a_{ij}$ is the normalization term.

The system matrix $\mathbf{A}$ based on the Poisson noise model was introduced. A more realistic model may take into account of other effects, such as the estimated attenuation correction factors α, scattered ($\mathbf{S} = \{s_i\}$) and random events ($\mathbf{R} = \{r_i\}$) [3]:

$$\bar{x}_j^{(n+1)} = \frac{\bar{x}_j^{(n)}}{\sum_{i\in I_j} a_{ij}/\alpha_i} \sum_{i\in I_j} a_{ij} \frac{\alpha_i y_i}{\sum_{l\in J_i} a_{il}\bar{x}_l^{(n)}/\alpha_i + r_i + s_i} \quad (1.12)$$

In addition, the convergence speed of MLEM can be improved using ordered subsets expectation maximization (OSEM) [32] which groups projections into subsets for simultaneous calculations:

$$\bar{x}_j^{(n+1)} = \frac{\bar{x}_j^{(n)}}{\sum_{i\in I_S} a_{ij}/\alpha_i} \sum_{i\in I_S} a_{ij} \frac{\alpha_i y_i}{\sum_{l\in J_i} a_{il}\bar{x}_l^{(n)}/\alpha_i + r_i + s_i} \quad (1.13)$$

where I_S are ordered subsets of LORs specified for reconstruction.

However, due to the use of subsets, the OSEM optimization function circles around but will not achieve the MLEM solution [33]. Nevertheless, as the convergence speed of OSEM is number-of-subsets times faster than MLEM, it is more frequently applied in practice [3].

1.2.3 Comparison between analytical and iterative reconstruction methods

Both FBP and MLEM (or OSEM) are routinely used in the clinic. To compare their performances, an example is presented here based on the numerical phantom shown in Fig. 1.10a. To simulate a PET acquisition, the phantom was forward projected into the projection space using the Radon transform (Eqn. 1.1). For simplicity, noise, scattered/random events, or the attenuation effect were not considered in the simulation. The resulting sinogram (Fig. 1.10b) was reconstructed using the FBP and MLEM algorithms.

To illustrate the back projection procedure of FBP, the reconstructed image planes with the increasing number of projections are exhibited in Fig. 1.10c-f. With limited projections, a streak artifact is shown in the reconstructed images (Fig. 1.10c-e). This artifact was caused by the improper combinations of the positive and negative components of the filtered projections, which were projected back to the image plane. The artifact was reduced when more projections were used. Usually, as the artifact has an intensity that is far smaller than the intensity of the rest of the image, it does not strongly affect visual diagnosis or ROI-based quantitative analysis [34]. However, when a small area has a much higher intensity than the rest of the image, the artifact around that area becomes severe and hampers anatomical identifications and physiological quantifications. This problem is further discussed in chapter. 2.

For iterative algorithms, the iteration number needs to be set carefully to achieve reliable reconstruction. As shown in Fig. 1.10g&h, with the limited number of iterations, the likelihood function of MLEM was far from convergent and the resulting images are therefore blurry. As the iteration number increased, the reconstructed images resembled the phantom more closely. However, image noise also increased as the iteration proceeded. To balance the tradeoff between the noise and reconstruction accuracy, an early stopping rule is often performed [35,36] which stops the optimization procedure before convergence, to ensure the quality of the reconstruction is sufficient for diagnosis.

In summary, FBP and MLEM have respective strengths and limitations. FBP is computationally effective and able to produce unique results due to the analytical calculation. However, when a severe streak artifact appears in reconstructed images, it may influence clinical diagnosis [37]. MLEM, on the other hand, provides better image quality, as it integrates the scanner geometry, noise model, and physical effects

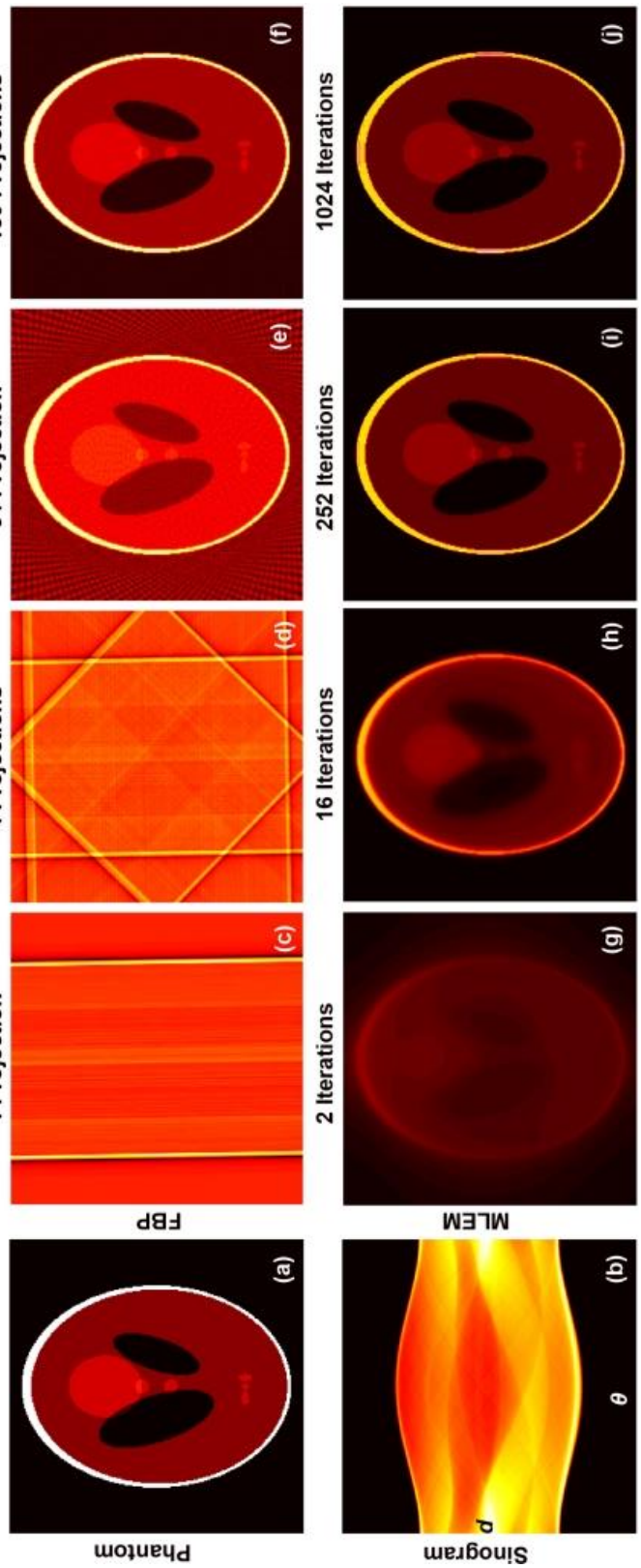

Figure 1.10: Plots of (a) a phantom with a regular shape; (b) the corresponding sinogram, including projections at each angle θ; reconstructed images using FBP with (c) 1, (d) 4, (e) 64, and (f) 180 projections; reconstructed images using MLEM with (g) 2, (h) 16, (i) 252 or (j) 1024 iterations

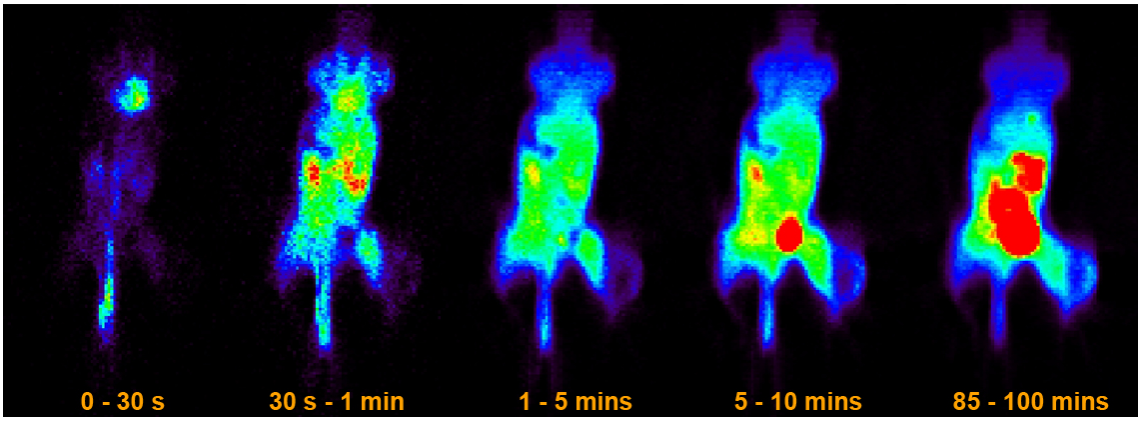

Figure 1.11: [^{18}F]Fmiso PET images (coronal view) of a mouse at different time intervals

among others into iterative reconstruction. However, the intensities of image voxels changes over iterations and the convergence rate depends on the individual data set. Since a common iteration number for all cases is difficult to find, a convergence evaluation is normally recommended before the final reconstruction, as discussed in chapter. 4.

1.3 Pharmacokinetic Modeling

After injection of a radioactive tracer into a living organism, it interacts with the organism through many processes. These interactions can be characterized by the pharmacokinetics of the injected substance, reflecting the intrinsic reaction of the specific tracer in a living organism [38]. PET is able to record these pharmacokinetic processes by scanning the organism dynamically. The measured coincident events are assigned to pre-defined time frames according to their acquisition time, forming a series of sinograms [3]. By reconstructing these sinograms, dynamic PET images are generated. These images record the changes of tracer activity distribution over time in the living organism (Fig. 1.11). Investigating the variations of a voxel or a ROI shown on the dynamic images, a "time-activity curve" (TAC) is drawn, reflecting the temporal development of the tracer on local tissue [3].

1.3.1 The 2-tissue compartment models

A TAC can be mathematically described by a pharmacokinetic model [38], which usually takes into account of the delivery, metabolism and clearance of the tracer in target tissues. For different tracers and their distinct physiologies, various kinetic

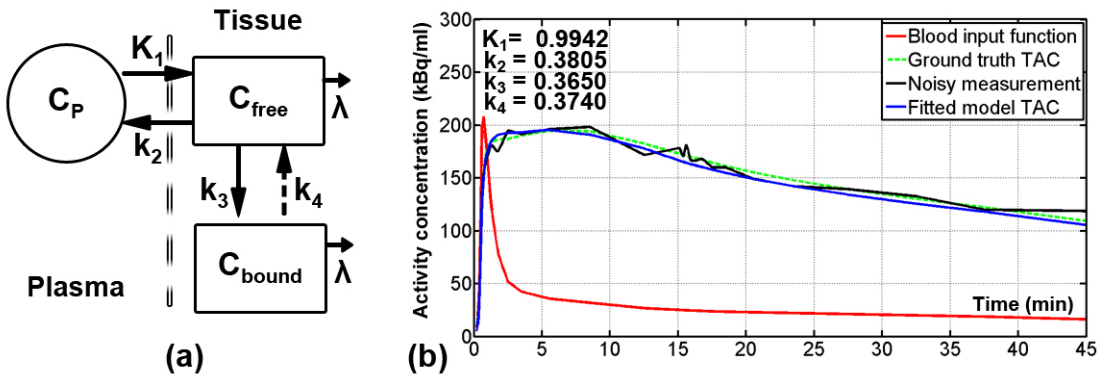

Figure 1.12: (a) A sketch of the two-tissue compartment model and (b) a plot of an exemplary curve fitting procedure

models have been developed. Here the two-tissue compartment model is introduced. This model is suitable for modeling popularly applied PET tracers in clinic practice and covers a wide range of applications (e.g., [^{18}F]FDG, [^{18}F]FLT, [^{18}F]FET, [^{11}C]MET, [^{11}C]PiB and [^{18}F]Florbetapir) [39–44].

As shown in Fig. 1.12a, the two-tissue compartment model describes the following situation: when the tracer enters into tissue from plasma, a portion incorporates into biologically active molecules due to chemical reactions and the other portion diffuses back into the plasma [3]. These situations are captured by the two-tissue compartment model using compartments: C_P represents the concentration of tracer in the whole blood ("the arterial input function", or AIF); C_{bound} denotes the tracer concentration interacting with surrounding tissue; and C_{free} denotes the unbound tracer concentration exchange between C_P and C_{bound}. Mathematically, the interactions between tracer and tissue compartments are expressed by the following differential equations:

$$\begin{cases} \frac{dC_{free}}{dt} = K_1 C_P - (k_2 + k_3) C_{free} + k_4 C_{bound} \\ \frac{dC_{bound}}{dt} = k_3 C_{free} - k_4 C_{bound} \end{cases} \tag{1.14}$$

$\mathbf{p} = \{K_1, k_2, k_3, k_4\}$ are "kinetic parameters" which are constants describing tracer exchange rates between tissue compartments.

By solving Eqn. 1.14, C_{free} and C_{bound} are acquired. The modeled tissue TAC

$\hat{C}$ is specified as:

$$\begin{aligned}&\hat{C}(t) = C_{free} + C_{bound} \\ &= \frac{K_1}{\alpha_2-\alpha_1}[(k_3+k_4-\alpha_1)e^{-(\alpha_1+\lambda)t} + (\alpha_2-k_3-k_4)e^{-(\alpha_2+\lambda)t}] \otimes C_P(t) + V_B C_P(t)\end{aligned}$$

$$\begin{cases}\alpha_1 = \frac{1}{2}[(k_2+k_3+k_4) - \sqrt{(k_2+k_3+k_4)^2 - 4k_2k_4}] \\ \alpha_2 = \frac{1}{2}[(k_2+k_3+k_4) + \sqrt{(k_2+k_3+k_4)^2 - 4k_2k_4}]\end{cases} \tag{1.15}$$

where t is the index of measured time points, the additional term V_B is the fractional blood volume, λ is the decay constant of the radioactive isotope, and "$\otimes$" denotes the convolution operator.

The tracer trapped in C_{bound} has undergone chemical reactions such as phosphorylation. However, these reactions may be reversed (e.g., dephosphorylation) and part of the tracer may be released back into C_{free}. In this case, $k_4 > 0$ and the model is referred to as a "reversible two-tissue compartment model". On the other hand, when these reactions are not reversible ($k_4 = 0$), the model is regarded as an "irreversible two-tissue compartment model". As $k_4 = 0$, the irreversible model has a simpler expression as follows:

$$\hat{C}(t) = K_1[\frac{k_2}{k_2+k_3}e^{-(k_2+k_3+\lambda)t} + \frac{k_3}{k_2+k_3}] \otimes C_P(t) + V_B C_P(t) \tag{1.16}$$

1.3.2 Model fitting

In practice, we are dealing with the inverse problem of kinetic modeling, i.e., given the model configuration, estimate the kinetic parameters. These parameters are distinct for different tissue/tracer types and contain the underlying functional information of the physiological processes [38]. With the knowledge of the model configuration, the AIF C_P and the measured TAC C, kinetic parameters $\mathbf{p} = \{K_1, k_2, k_3, k_4, V_B\}$ can be estimated using the commonly known least-squares optimization [3, 45]:

$$\arg\min_{\mathbf{p}} = \sum_{t}^{N_T} w_t(C_t - \hat{C}_t(\mathbf{p}))^2 \tag{1.17}$$

where N_T is the total number of measured time points and $\mathbf{w} = \{w_t\}$ denotes the weightings factors.

Quantitatively, Eqn. 1.17 aims to find an optimal set of $\mathbf{p}$, which minimizes the sum squared difference between $\hat{C}$ and C. It is equivalent to finding the $\mathbf{p}$ that results in a specific model prediction, which can best fit the measured curve. The weighting factor is optionally imposed on each fitting point according to prior knowledge of variance [45]. For instance, $\mathbf{w}$ can be set to be positively proportional to the measurement duration for each data point. Therefore, a longer measurement,

which is expected to have a higher SNR, gains more weight (authority) for model fitting. More frequently, $\mathbf{w}$ is set to be uniform ($\mathbf{w} = 1.0$), and no preference is imposed during model fitting [45]. The optimization of Eqn. 1.17 is commonly achieved using numerical nonlinear regression methods, such as trust region or Levenberg-Marquardt [46]. A sample fitting result is given in Fig. 1.12b. With the AIF (red) and the noisy measurement (black), the modeled TAC (blue) calculated from the estimated $\mathbf{p}$ fits the measurement well and can reflect the truth TAC (green).

1.4 Direct Parametric Image Reconstruction

As introduced above, pharmacokinetic parameters $\mathbf{p}$ are estimated by applying a kinetic model to TACs extracted from reconstructed dynamic PET images. When the model fitting is applied to TACs for each voxel ("the voxel-wise modeling"), a set of parametric images are generated. Different from a PET image, the parametric images give the spatial distribution of each kinetic parameter. This reconstruction-modeling two-step method is often referred to as the "indirect parametric image generation" method [47, 48].

In practice, the coincidences acquired during PET imaging are limited in numbers, and errors are introduced due to attenuation, scattering, and random effects. Thus, a PET measurement is usually considered to have a relatively low SNR [3]. This makes the voxel-wise modeling procedure challenging. To improve the quality of model fitting, a "direct parametric image reconstruction" (DPIR) method has been proposed [47]. It combines reconstruction and modeling into one step and enables the parameter estimation directly from the projection data. In principle, DPIR integrates a temporal model into the iterative reconstruction model [47, 49]. The dynamic images $\hat{\mathbf{X}}$ is then expressed as a temporal function multiplying with model parameters ($\hat{x}_{jt} = f_{jt}(\mathbf{p})$). When a pharmacokinetic model is used as the temporal function, the model parameters are then equivalent to the pharmacokinetic parameters.

By substituting $\hat{\mathbf{X}}$ in Eqn. 1.8 as the function of $\mathbf{p}$, the objective function with respect to the kinetic parametric images $\mathbf{P} = \{\mathbf{p}_{jk}\} \in \mathbb{R}^{N_{vox} \times N_K}$ (N_K is the number of kinetic parameters) is written as:

$$\mathbf{p}^{(n+1)} = \arg\max_{\mathbf{p}} \sum_{i \in I_j} \frac{a_{ij}}{\alpha_i} \sum_{t}^{N_T} (-f_{jt}(\mathbf{p}) + \frac{f_{jt}^{(n)}(\mathbf{p}) y_i}{\sum_{l \in J_i} a_{il} f_{lt}^{(n)}(\mathbf{p}) / \alpha_i + \mathbf{r}_i + \mathbf{s}_i}) \tag{1.18}$$

The optimizing difficulty in Eqn. 1.18 depends on the complexity of $f(\mathbf{p})$. For linear models, $\mathbf{p}$ is separable from the temporal basis function $\mathbf{f}$, enabling the expression of $\hat{\mathbf{X}}$ as the inner production of $\mathbf{p}$ and $\mathbf{f}$ [47, 50]:

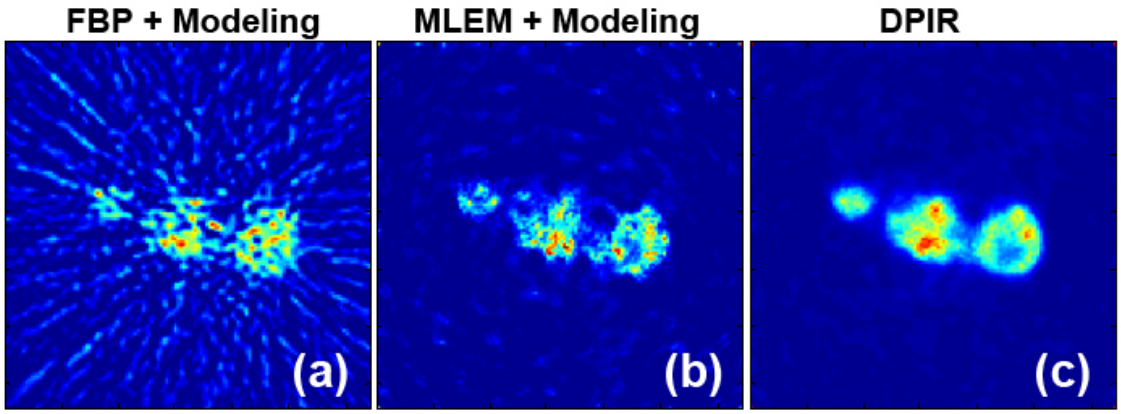

Figure 1.13: Sample parametric images reconstructed by (a) the indirect FBP+kinetic modeling method, (b) the indirect MLEM+kinetic modeling method and (c) the direct parametric image reconstruction method

$$\hat{\mathbf{X}} = \sum_{k}^{N_K} \mathbf{p}_{jk} \mathbf{f}_{kt} \tag{1.19}$$

where **k** is the subscript of kinetic parameters.

As later discussed in chapter. 4, the integration of Eqn. 1.19 will result in a closed-form update function for iteratively updating the kinetic parameters **p** [47–54]. However, as most kinetic models are nonlinear, the optimization procedure becomes challenging and may be limited to a specific model [55, 56]. Approximations and functional substitution are often required for optimization as discussed in chapter. 3 [49, 57–59].

Recently, DPIR has drawn more and more attention [60]. It has been proven to generate parametric images with improved image quality and fewer statistical errors, compared to the indirect parametric image generation methods [47–63]. Fig. 1.13 presents an example illustrating the effects of using DPIR for parametric image reconstruction. As shown, the image generated by DPIR has the highest SNR compared to those obtained from indirect methods. A possible explanation is: for indirect methods, reconstruction and modeling are separate steps, and only partial data with limited SNR has been used in each individual procedure. In the reconstruction step, image frames are calculated independently. In the voxel-wise fitting step, TACs are modeled independently. On the other hand, DPIR is applied simultaneously to the complete 4D (3D spatial + 1D temporal) PET data of the maximized SNR for both reconstruction and modeling [48]. Thus DPIR can provide parametric images of higher quality.

Though DPIR has shown promising potential to be applied in clinical practice,

there are remaining challenges. For instance, a kinetic model with a large parameter dimensionality (e.g., multi-tracer models) may limit the performance of DPIR (discussed in chapter. 3). In addition, though DPIR enables the improvement of image quality, whether this gives additional value to physiological quantification in clinical diagnosis is not yet clear. These issues require further investigations.

1.5 Thesis outline

This thesis proposes mathematical algorithms to improve dynamic PET reconstruction by utilizing temporal coherence and pharmacokinetics. An overview of PET imaging, reconstruction methods, and pharmacokinetic modeling is presented in chapter. 1. This thesis makes efforts to improve the two types of the reconstruction methods. Chapter. 2 proposes a framework to reduce sever streak artifacts, which arises from the analytically FBP reconstruction. On the other hand, an iterative DPIR method is proposed in chapter. 3 to particularly deal with a multi-tracer model of a large parameter dimensionality and improve tracer separation. In addition, the physiological value resulting from the improvements of PET reconstruction is initially evaluated in chapter. 4. Conclusions are given in chapter. 5.

2

Streak Artifact Reduction in Filtered Back Projection

Filtered backprojection (FBP) is an analytical image reconstruction method for computing tomographic images. It is widely used in practice for its high computational efficiency and high reliability for PET physiological quantification [64]. However, an intrinsic artifact appearing as a streaking effect ("the streak artifact") overspreads all FBP images. This artifact does not influence clinical diagnosis unless it becomes severe, due to the overwhelmingly high tracer uptake in some organs, a situation which often occurs in practice. To reduce the severe streak artifacts in dynamic FBP images, a framework is proposed in this chapter, which utilizes the temporal information of PET data for artifact reduction in the image space. Both simulations and real measurements were used for method validation. Tomographic images generated from the proposed framework were quantitatively compared with those calculated by using the original FBP method.

Part of this work has been published in [65].

2.1 The Streak Artifact

The streak artifact is typically seen in FBP images. It arises from the back projection procedure during reconstruction. After a filtered projection is inversely transformed from the Fourier domain, negative and positive contributions are projected back to the image plane. Ideally, with an infinitesimal projection angle interval ($\triangle\ \theta \to 0$), both contributions between neighboring lines counteract properly and the streak artifact is avoided. In reality, due to the limited angle sampling, streak artifacts appear in FBP images. However, they are usually far smaller than the normal signal (Fig 2.1b), which is acceptable for clinical diagnosis. Nevertheless, when the reconstructed image contains one or more regions of overwhelmingly high signals,

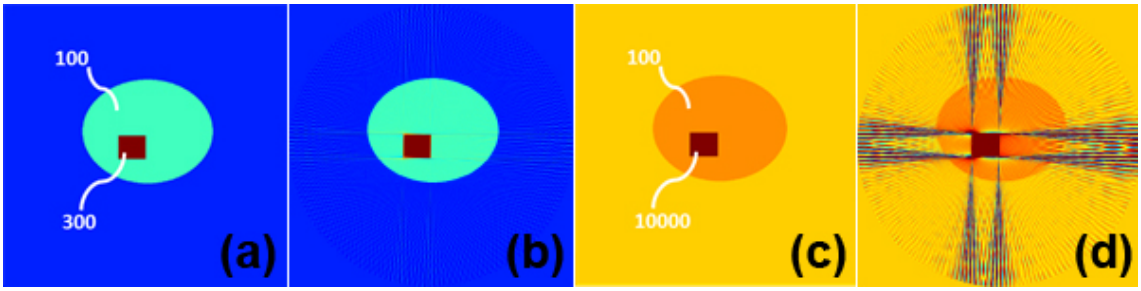

Figure 2.1: Plots of: (a) a phantom image consisting of two ROIs which have comparable signal levels; (b) the corresponding FBP image of (a); (c) a phantom image consisting of two ROIs which have incomparable signal levels; (d) the corresponding FBP image of (c)

the striking contrasts at the regions' borders result in an amplified streak effect, destroying the rest of the image dramatically (Fig 2.1d).

In practice, the severe streak artifact hampers the application of FBP. For instances, in CT imaging, the artifact is caused by metallic implants (e.g., hip prostheses or dental fillings), which degrades the accuracy of examinations and influences dose calculations [66]; In the area of nuclear medicine, the artifact is mainly due to tracer accumulation in e.g., the bladder, which leads to severe distortions of the abdomen image and complicates the diagnosis of prostate or cervical cancer [37].

Many approaches have been proposed to reduce the streak effect. Efforts have been focused on either linear or higher order interpolations between two successive projections [67, 68] or on the incorporation of modified iterative expectation maximization (EM) algorithms with additional constraints [69, 70]. However, with most interpolation methods, areas around high signal intensity regions are still distorted. For the modified iterative methods, the imposed non-negative constraints may lead to biased reconstructions with less quantitative value.

In addition, there has been constant debate and comparison between FBP and iterative algorithms [64, 71–73]. As discussed in Sec. 1.2.3, both methods have their respective strengths and limitations. Iterative reconstruction may provide better visual quality. However, FBP has superior computational efficiency and quantitative stability. These merits are desired for dynamic PET applications and pharmacokinetic estimations.

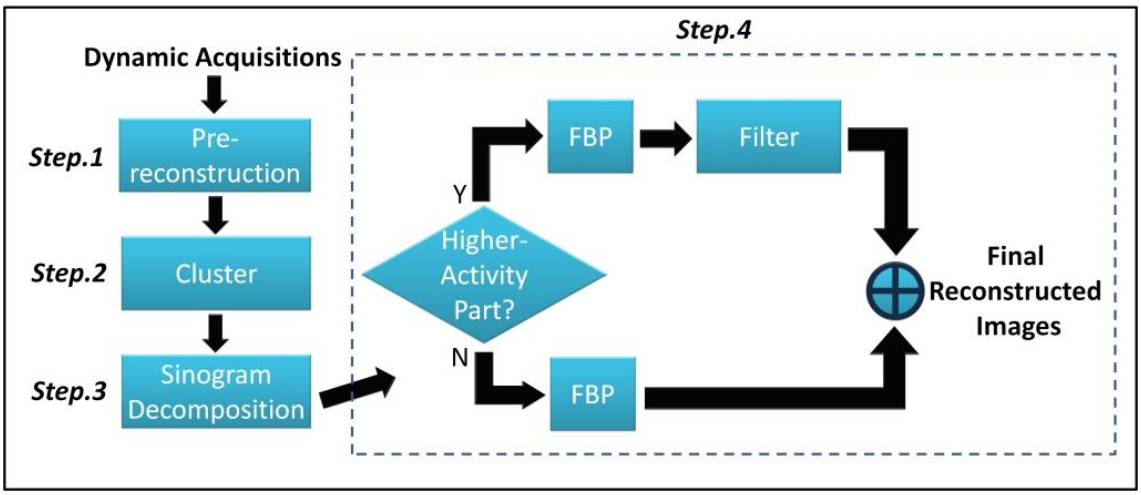

Figure 2.2: A plot of the flow chart of the proposed framework

2.2 Time-Activity Curve based Sinogram Decomposition for Streak Artifacts Reduction

This chapter proposes a framework to automatically reduce the severe streak artifacts in dynamic PET images which are reconstructed using FBP. Concerning the severe artifact arising due to the existence of incomparable signal levels in the image plane, the new method utilizes the temporal information of dynamic PET data to distinguish signal levels and accordingly decompose the data in the projection space (sinogram). The decomposed sinograms corresponding to higher signal levels are particularly processed to reduce severe streak artifacts before the final reconstruction.

More specifically, the framework consists of 4 steps as illustrated in Fig. 2.2: 1. pre-reconstruction; 2. clustering TACs of comparable levels; 3. decomposition in the projection space based on the mean clustered TACs; 4. reconstruction of the decomposed sinograms and reassembling. A detailed explanation of each step is given below.

2.2.1 Pre-reconstruction of dynamic PET acquisitions

The proposed method utilizes TACs extracted from dynamic PET images to identify incomparable signal levels. Pre-reconstruction is thus required and can be achieved effectively using the original FBP method described in Sec. 1.2.1. It is assumed that reconstructed images $\hat{\mathbf{X}}(t)$ contains in total T temporal frames and N_{vox} voxels per frame. The intensity of the j^{th} voxel over time $\mathbf{x}_j(t) = [x_j(1), x_j(2), \cdots, x_j(L)]^T \in$

$\mathbb{R}^T$ represents a TAC of length T. Therefore $\hat{\mathbf{X}}$ is also considered as a vector set of N_{vox} TACs of length T. When incomparable signal levels exist, this pre-reconstructed $\hat{\mathbf{X}}$ is ruined by severe streak artifacts.

2.2.2 Extraction of characteristic TACs

To differentiate incomparable signal levels, characteristic temporal courses of individual signal levels with comparable intensities are extracted from the N_{vox} TACs by clustering areas of similar temporal development in the image plane. Clustering is achieved using the K-Mean algorithm with the Euclidean distance as similarity metrics [74]. The N_{vox} TACs are grouped into M clusters, with the mean curve $\bar{\mathbf{C}}_m(t)$ and the variance σ_m of each cluster m ($m = 1, 2, \cdots, M, M \ll N_{vox}$) under the condition:

$$\sigma_m \ll \sigma/M$$

where σ is the variance of $\hat{\mathbf{x}}_j(t)$.

As the result, TACs of similar variance (i.e., similar signal intensities) are classified into one group. Different groups are considered at different signal levels. $\bar{\mathbf{C}}(t) = \{\bar{\mathbf{c}}_m(t)\}$ represents the characteristic TACs of each group and are used to guide the decomposition of PET data in the projection space.

2.2.3 Decomposition in projection space

For 4D PET data, individual TACs are associated with spatial regions of specific physiological properties, relating to distinct components in the projection space. With the clustering of TACs in the temporal domain, sinograms in the projection space can be distinguished [75].

Recalling that the dynamic PET acquisitions in the projection space $\mathbf{Y}(t) = \{\mathbf{y}_i(t)\} \in \mathbb{R}^{N_{LOR}}$ are related to the source $\mathbf{X}(t)$ using radon transformations as described in Eqn. 1.5. The projection model $\mathbf{A}$ maps the intensity of each image voxel to the projection space to form projections. Therefore with the knowledge of $\mathbf{A}$, it is able to back retrieve for each voxel or group of voxels the corresponding sinogram portions from the projection space.

By grouping voxels in a physiological region according to the similarity of their temporal development, each sinogram that corresponds to the respective characteristic TAC is extracted. From the mathematical point of view, the characteristic TACs representing each physiological region in the image plane are considered as temporal basis functions. The sinogram $\mathbf{Y}(t)$ in the projection space is decomposed into weights to each basis function:

$$\begin{pmatrix} \mathbf{y}_1(t) \\ \mathbf{y}_2(t) \\ \vdots \\ \mathbf{y}_{N_{LOR}}(t) \end{pmatrix} = \begin{pmatrix} b_{1,1} & b_{1,2} & \cdots & b_{1,M} \\ b_{2,1} & b_{2,2} & \cdots & b_{2,M} \\ \vdots & \vdots & \cdots & \vdots \\ b_{N_{LOR},1} & b_{N_{LOR},2} & \cdots & b_{N_{LOR},M} \end{pmatrix} \begin{pmatrix} \mathbf{z}_1(t) \\ \mathbf{z}_2(t) \\ \vdots \\ \mathbf{z}_M(t) \end{pmatrix} \tag{2.1}$$

or in the matrix format:

$$\mathbf{Y}(t) = \mathbf{B}\mathbf{Z}(t) \tag{2.2}$$

where $\mathbf{Z}(t) \in \mathbb{R}^M$ is a set of M characteristic TACs. Each TAC $\mathbf{z}_m(t) = [z_m(1), z_m(2), \cdots, z_m(T)]$ is considered a temporal basis function corresponding to a physiological region. $\mathbf{B} = \{b_{i,m}\} \in \mathbb{R}^{N_{LOR} \times M}$ and $b_{i,m}$ is the weight for voxels detected by the i^{th} LOR, meanwhile possessing the same m^{th} characteristic TAC. Thus the matrix $\mathbf{B}$ contains the decomposed sinograms corresponding to each of the M TACs.

The sinograms at the same signal level have similar intensities. Therefore $\mathbf{B}$ at each signal level is considered to be rather smooth. This prior expectation is included in Eqn. 2.3 by adding the ℓ_2-norm to regularize the solution of $\mathbf{B}$, leading to a minimization of the following term [76]:

$$\arg\min_{\mathbf{B}}(\|\mathbf{Y} - \mathbf{B}\mathbf{z}\|_2 + \beta\|\mathbf{B}\|_2) \tag{2.3}$$

where β is the constant term for regularization.

With the additional regularization term, the solution $\mathbf{B}$ is preferred to have a low norm (i.e., to be smooth) such that the cost function in Eqn. 2.3 can be optimized. Optimizing Eqn. 2.3 results in a closed-form function for calculating $\mathbf{B}$:

$$\mathbf{B}_{im} = (\sum_t \mathbf{Y}_{it}\mathbf{z}_{mt}^T)/(\sum_{mt} \mathbf{z}_{mt}\mathbf{z}_{mt}^T + \beta); \tag{2.4}$$

where T is the transpose operator.

As $\mathbf{B}$ is acquired, the weight is normalized to $[0, 1.0]$ for each sinogram frame. Sinogram decomposition is then achieved by multiplying the original $\mathbf{Y}$ with the decomposed weight $\mathbf{B}$ at each frame.

Here, the clustered mean curves $\bar{C}_m(t)$ in Sec. 2.2.2 are taken as characteristic TACs for the sinogram decomposition. Considering that the incomparable signals usually appear after a few minutes when the radioactive tracer has metabolized for a while, the decomposition starts from the frame l_0 when obvious incomparable signals appear ($max(\bar{\mathbf{c}}_{m,l_0})/min(\bar{\mathbf{c}}_{m,l_0}) > \phi$, ϕ is a constant).

2.2.4 Resembling of reconstructions

When the sinogram has decomposed into parts with different signal levels, each part can be reconstructed individually using FBP. The sinograms with high signal

levels will still result in strong streak artifacts in the reconstructed images, but these artifacts can be easily filtered out using standard algorithms such as clustering or thresholding. Reconstructing the rest of the sinogram with FBP leads to normal images. Though streak artifacts remain in these images, but they are comparatively small. The final images are reassembled from all the reconstructions of decomposed sinograms.

2.3 Algorithm Evaluation

To evaluate the performance of the proposed algorithm, both numerical simulations as well as real PET data were acquired. The artifacts-corrected images are compared with traditional FBP images. This section presents the data acquisition procedures and quantification methods for analyzing results.

2.3.1 Simulation study

As shown in Fig.2.3, a numerical abdomen phantom was constructed with realistic anatomical structures including bladder, prostate, etc. A ^{18}F-FDG dynamic PET for 60 minutes was simulated, where TACs associated with each tissue area except for the bladder were calculated using the irreversible two-tissue compartmental model (Eqn. 1.16) based on physiological parameters taken from literature as listed in Tab. 2.1. The bladder TAC cannot be described by the irreversible model and thus it is extracted from a preclinical PET data. For proof of concept, the TAC was normalized and interpolated to the measurement points consistent with other tissue TACs. Over all, the phantom consists of 256×256 pixels and 43 frames (frame duration: 1s - 2.5 min) according to a real PET protocol. The tracer was continuously cleaned during metabolism and accumulated in the bladder, leading to at least 30 times higher activity concentration than in other tissues over 20 minutes. Each image slice was forward-projected and binned into a sinogram (128 bins, 64 projection views). Poisson noise was generated in each LOR. In total, the simulated acquisition consisted of 43 frames and 128×64 LORs per frame.

Table 2.1: Kinetic parameters of each tissue ROI

	Fat	Crassum	Muscle	Prostate	Bone	Spine	Tumor
K_1	0.018	0.150	0.027	0.251	0.160	0.260	0.522
k_2	0.102	0.433	0.154	0.328	0.400	0.378	0.999
k_3	0.055	0.112	0.076	0.190	0.083	0.114	0.438

Units: K_1: mL/min/g; k_2&k_3: min^{-1}

The sinogram acquisition was pre-reconstructed into an image series ($256 \times 256 \times$

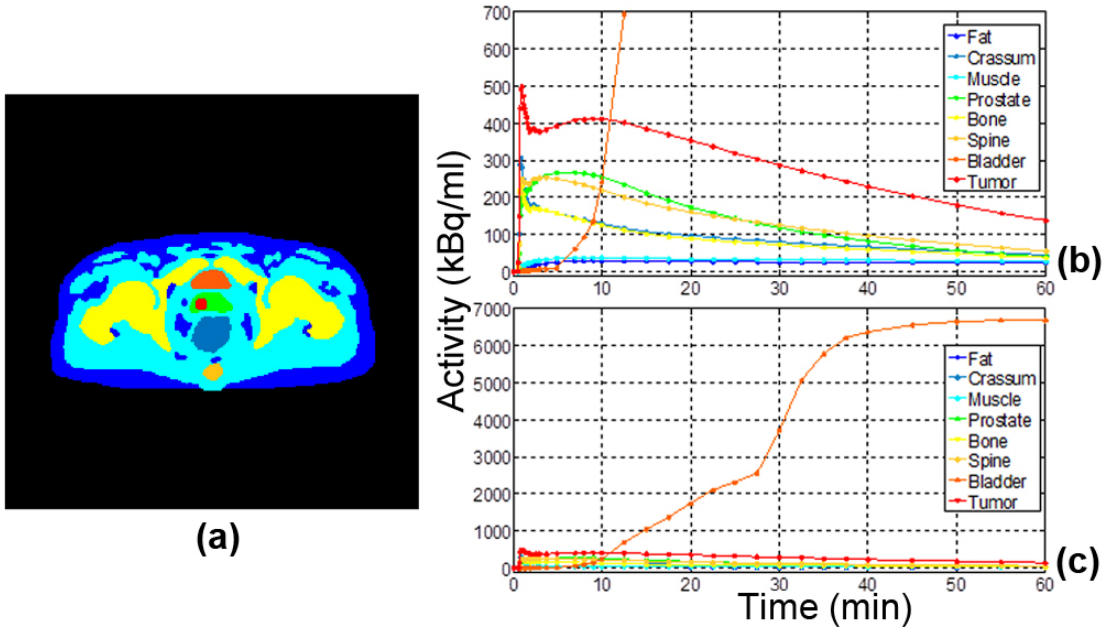

Figure 2.3: (a) A plot of an abdomen phantom; (b) a zoom-in plot of TACs assigned to tissues and (c) a full-view plot of the TACs (The color of each TAC is consistent with the color of corresponding tissue regions.)

43) using the traditional FBP. Here the proposed algorithm was applied with a $\phi = 20$. Thus for each frame, when the maximum intensity of the high signal level is 20 times larger than the minimum intensity of low signal level, the new algorithm will be executed. The regularization parameter β was set to be 270 for sinogram decomposition.

The dynamic PET images of the phantom were reconstructed using the proposed method as well as the traditional FBP algorithm. Results from both methods were quantitatively compared with the ground truth (GT) in terms of root mean square error (RMSE, Eqn. 2.5). Here we focused on tissue ROIs of normal signal level to evaluate the influence of streak artifacts.

$$RMSE = \sqrt{\frac{1}{N_j} \sum_{j \in ROIs} (Img_j - GT_j)^2} \tag{2.5}$$

where N_j denotes the number of voxels within ROIs and Img stands for the reconstructed tracer activity distributions (over all frames) or parametric images.

In addition, for dynamic PET study, tracer pharmacokinetics are of interests for investigating the underlying physiological properties of target tissues. The physiological accuracy may be affected by the reconstruction method and the artifacts.

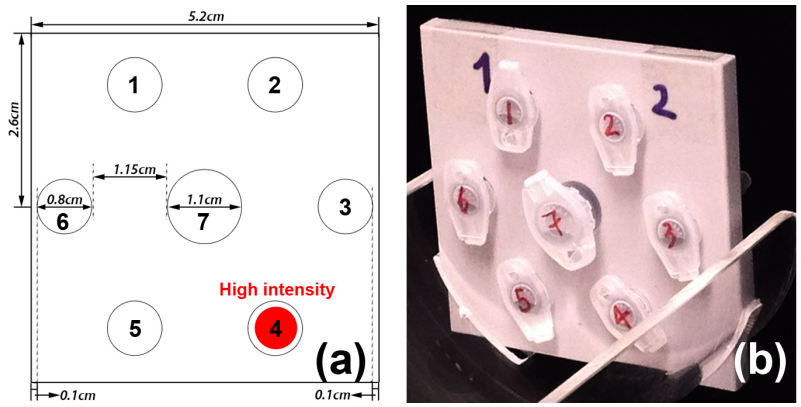

Figure 2.4: (a) A sketch of the phantom design with parameters and (b) a photo of the physical phantom inserted with Eppendorf tubes with ^{18}F-FDG

Thus the parametric images were generated for further evaluation of both methods, by applying the irreversible two-tissue compartmental model to the reconstructed images. The interesting K_1 and k_3 parametric images from both methods were assessed in RMSE.

Furthermore, additional tests were designed to study the influence of the projection number on the performance of the proposed method. Thus data sets with 32 or 128 projections were also simulated and reconstructed under the same conditions for comparison. Note that the parameter β in Eqn. 2.3 is case-dependent. The accuracy of the reconstruction may vary as β changes. Thus various values of β coving a wide range (from 0 to 1000) have been tested to optimize the regularization term in Eqn. 2.3. Similarly, the results obtained from both methods were compared in terms of RMSE.

2.3.2 Real data validation

To evaluate the algorithm for real applications, a dynamic scan of a physical phantom was performed with a Siemens Inveon PET. The dynamic scan was created by static measurements and each acquisition served as a period of dynamic measurements framing up to a certain time point. The physical phantom consists of 7 holes for insertable Eppendorf tubes (Fig. 2.4). These tubes were filled with ^{18}F-FDG tracer of different concentrations. For each scan, tracer activities were manually changed in each tube according to realistic TACs. In total, the dynamic scan contains 35 frames: 8 x 5 s, 2 x 10 s, 8 x 30s, 12 x 150s, and 5 x 300s. The resulting acquisition consists of 128×160 LORs and 159 planes per frame. Data were corrected for decay to the starting time point of the experiment. Due to lack of ground truth, the results of real measurements were evaluated mainly by visual comparisons.

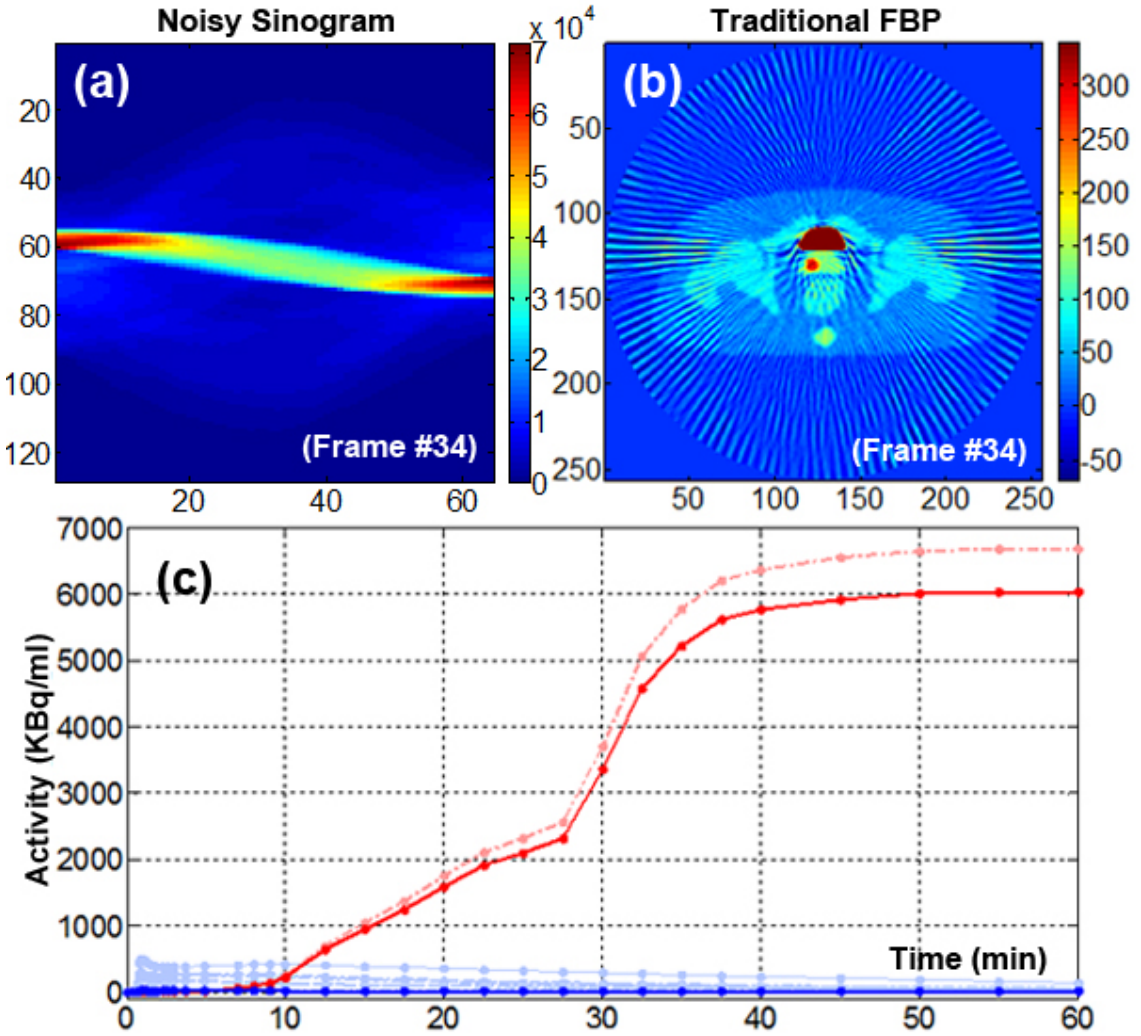

Figure 2.5: An exemplary frame (frame #34) of (a) noisy sinograms and (b) FBP reconstructed images; (c) a plot of two mean characteristic TACs (solid) of incomparable signal levels compared to the true TACs (dash)

2.4 Results

2.4.1 Performance evaluation on simulation data

Fig. 2.5b presents a sample frame (frame #34) of the normal FBP images prereconstructed from the noisy sinogram (Fig. 2.5a). The image contains server streak artifacts due to the high intensity of the bladder image. Panel c demonstrates the clustering results where two mean characteristic TACs were extracted from the dyn-

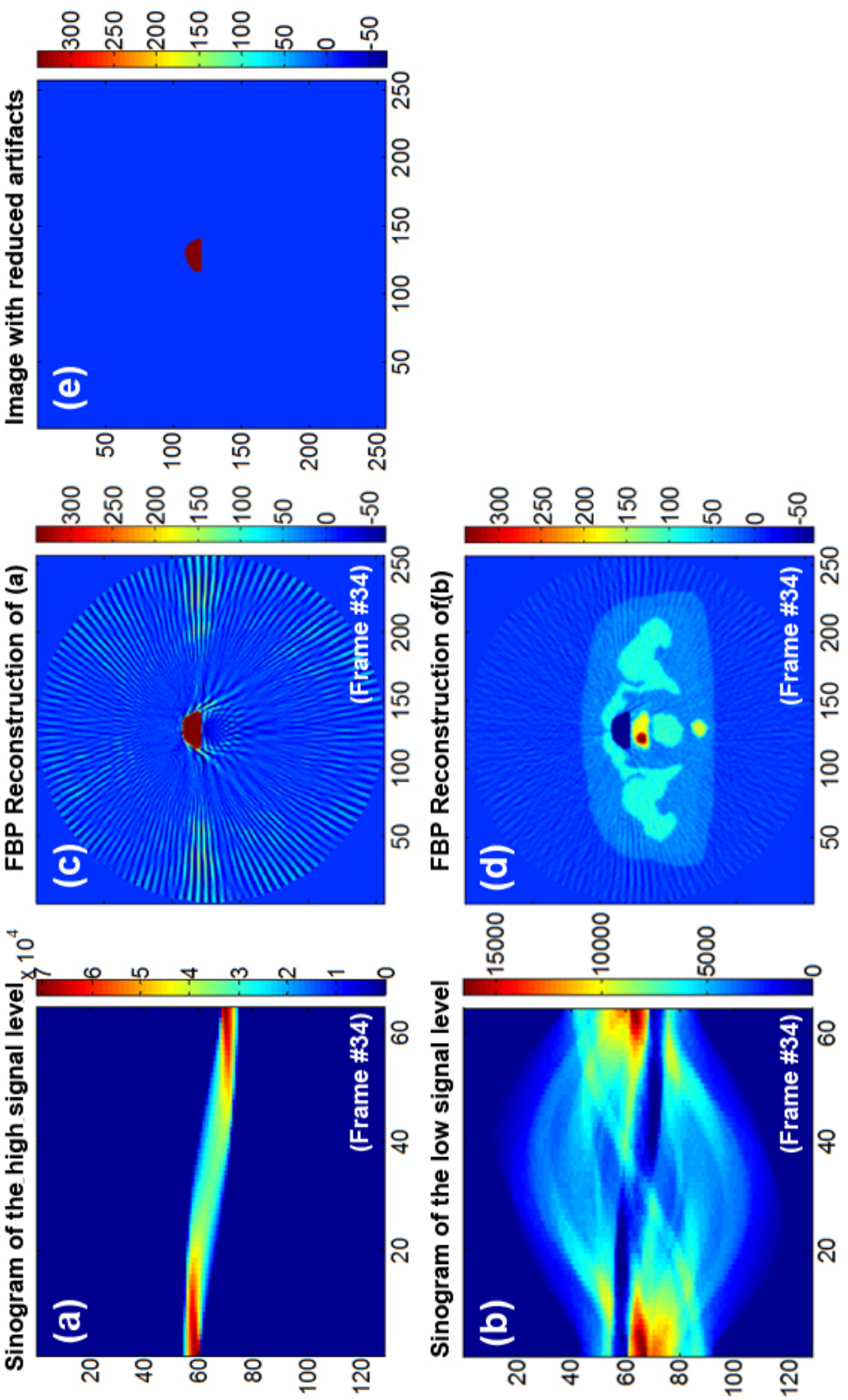

Figure 2.6: An exemplary frame (frame #34) of (a) the decomposed sinogram corresponding to tissue of high tracer activity concentrations (bladder); (b) the decomposed sinogram corresponding to the rest of the tissue areas of the phantom; the reconstruction of (c) the bladder area and (d) the rest of the tissue areas; (e) a clean image of the bladder with reduced artifacts

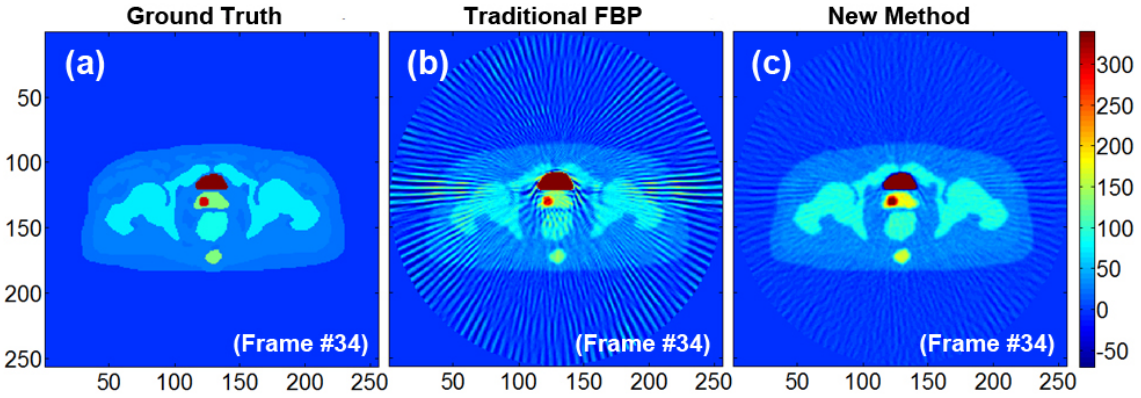

Figure 2.7: An exemplary frame (frame #34) of (a) the ground truth; the reconstructed images obtained from (b) traditional FBP and (c) the proposed method

amic FBP image, representing two incomparable signal levels (bladder and normal tissue) of the tracer activity distributions. The clustered TACs were taken as the basis function for sinogram decomposition. Here $\phi = 20$ led to the decomposition of frames 28 to 43.

As shown in Fig. 2.6, the decomposed sinogram with ($\beta = 270$) includes a high activity concentration part (panel a) corresponding to the bladder, and a normal activity concentration part (panel b) corresponding to the rest of the tissues. The decomposed sinograms were reconstructed using the traditional FBP. The streak artifacts in panel c of the high activity part were filtered out using a clustering algorithm. The cleaned bladder image (panel e) was added to the reconstruction obtained from the normal intensities (panel d), yielding the final result.

Fig. 2.7 shows a comparison between the final reconstructed images obtained from the proposed algorithm and the traditional FBP. The proposed method has achieved a significant reduction of artifacts compared to FBP. Quantitatively, as compared to the phantom GT, the RMSE of the traditional method was 58% and it has been reduced to 15% using the proposed method. A 75% improvements in RMSE was thus achieved by the proposed method.

The exemplary K_1 images generated from different methods are illustrated in Fig. 2.8. In the traditional FBP image (panel b), regions such as the border of the bladder are affected by the severe artifacts, which is not noticeable using the new method. For quantitative analysis, the result shows that the reconstruction using the new method has a better quantification accuracy than FBP. A 37% and 55% improvement in RMSE was gained for the interesting parameters K_1 and k_3 respectively. It should be noted that the bladder is not applicable for the two-tissue compartment model which is usually excluded from quantitative analysis. Thus we did not consider the bladder for RMSE.

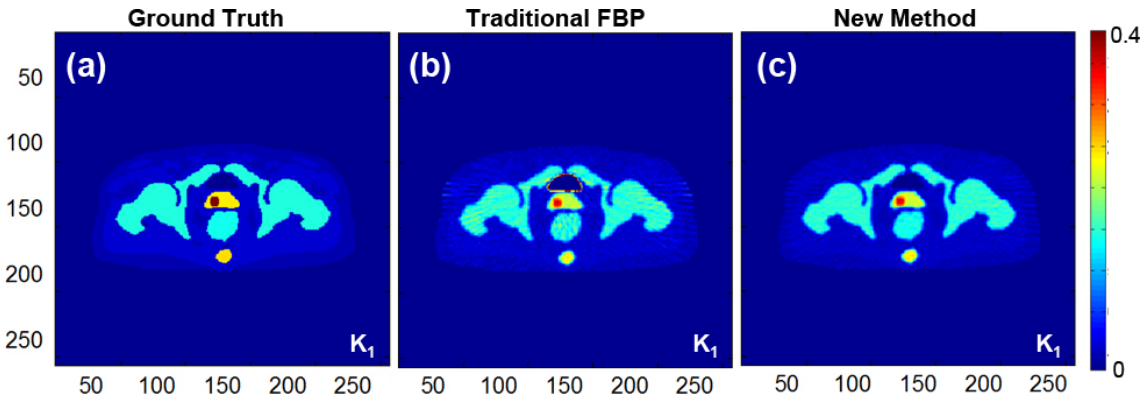

Figure 2.8: The K_1 parametric images generated from (a) the GT (b) the traditional FBP method and (c) the proposed method

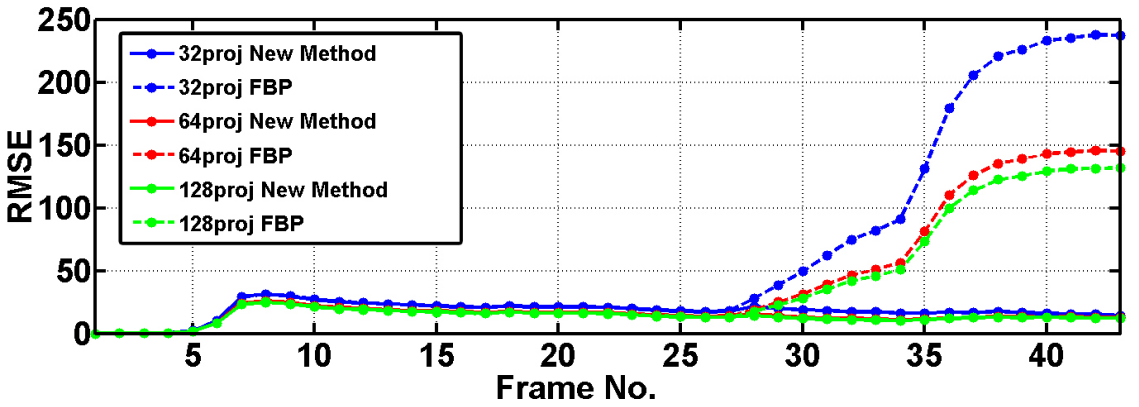

Figure 2.9: A plot of the RMSE of tracer activity concentration of each time frame between the ground truth, FBP(dash) and the new method (solid) using 32 (blue), 64 (red) or 128 projections (green)

Table 2.2: RMSE of kinetic parameters and tracer activity distributions

	K_1			k_3			tracer activity distributions		
Projections	32	64	128	32	64	128	32	64	128
FBP	0.039	0.032	0.030	0.435	0.293	0.141	102.78	63.70	57.77
New Method	0.022	0.019	0.019	0.069	0.064	0.064	19.24	15.19	14.55
Improvement(%)	43.59	40.63	36.67	84.14	78.16	54.62	81.28	76.15	74.81

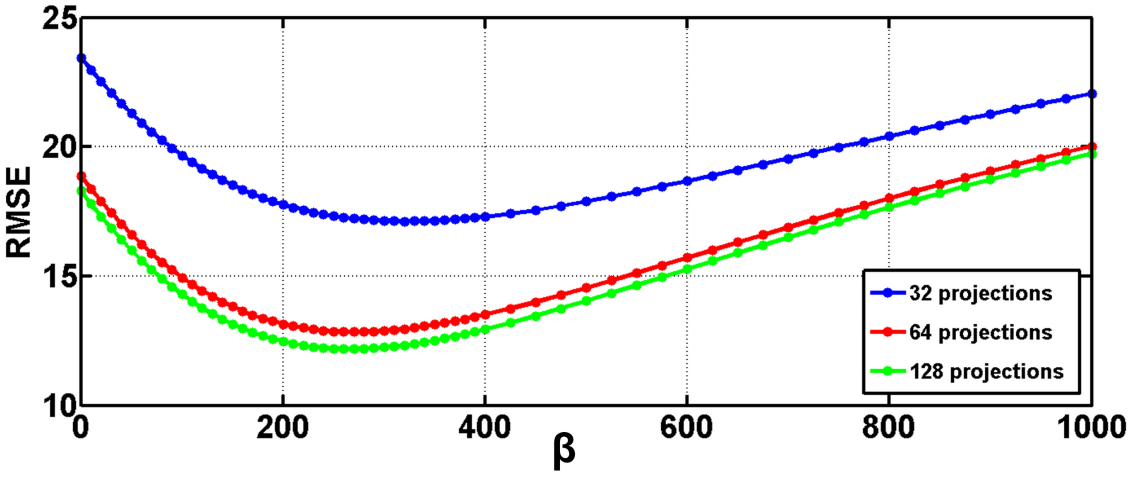

Figure 2.10: A plot of the mean RMSE of tracer activity distributions over frames as β changes, using 32 (blue), 64 (red) and 128 (green) projections

Regardless of the projection numbers (32, 64 or 128) investigated, RMSE improvements were achieved with the proposed method on the tracer activity distributions as well as the parametric images as listed in Tab. 2.2. The improvement is more obvious as fewer numbers of projections were used. This can be further confirmed by Fig. 2.9, where the RMSE was measured for every image frame reconstructed with 32 (blue), 64 (red) or 128 (green) projections. For both methods, RMSE can be improved to some extent by including more projections. For the traditional method, a larger RMSE was observed as the frame index increased and the error curve reflects the increasing differences between signal levels. For the proposed method, RMSE was relatively low ($RMSE \approx 15$) for all applied frames (frame # 28 to # 43) and all investigated projection numbers.

Fig. 2.10 evaluated the effects of the regularization parameter β. As shown, the accuracy of the reconstructed tracer activity distribution varies as β changes. For all projection numbers investigated, an optimum β that leads to the minimal RMSE can be found within a relatively wide range ($\beta : 220 - 330$).

2.4.2 Performance evaluation on real measurements

As shown in Fig. 2.11a, two characteristic TACs with incomparable signal levels were extracted using K-Mean clustering from pre-reconstructed phantom images. The red TAC corresponds to the high intensity area (Tube #4) while the blue TAC represents the mean TAC of the remaining phantom regions. Sinograms were accordingly decomposed into the low and high activity parts as presented in Fig. 2.11b&c.

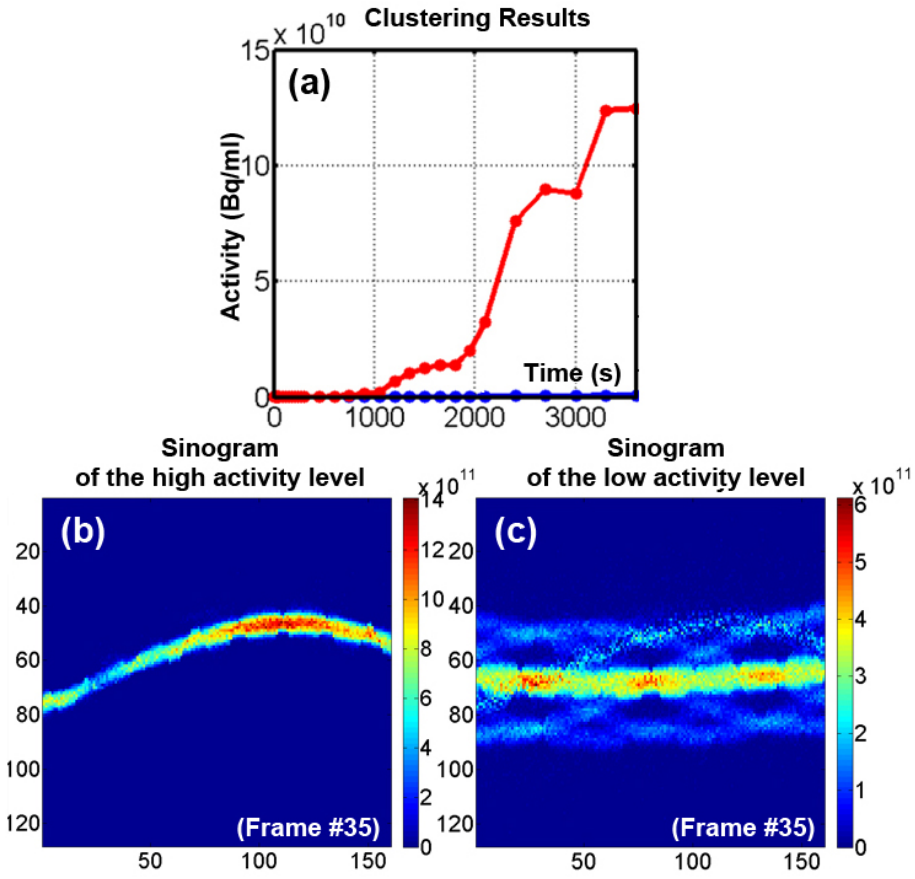

Figure 2.11: (a) A plot of the clustering result extracted from the pre-reconstructed dynamic PET images of the physical phantom; (b) the decomposed sinogram corresponding to the (red) characteristic TAC and the high activity area of the phantom; (c) the decomposed sinogram corresponding to the (blue) characteristic TAC and the low activity areas of the phantom

The reconstructed images using the traditional FBP method and the proposed method are compared in Fig. 2.12. The image obtained from the proposed method ($\phi = 20; \beta = 270$) shows a clear improvement in image quality in comparison with the results of the traditional FBP. With the proposed method, all of the seven rounds of FDG activity are seen and are no longer covered by the severe streak artifacts seen in the FBP images. Due to the technical problems of this complicated experiment, a small portion of data is missing and is completed by interpolation. However, for proof-of-concept, the reconstruction of this physical phantom has confirmed that a better image quality can be obtained with the proposed algorithm.

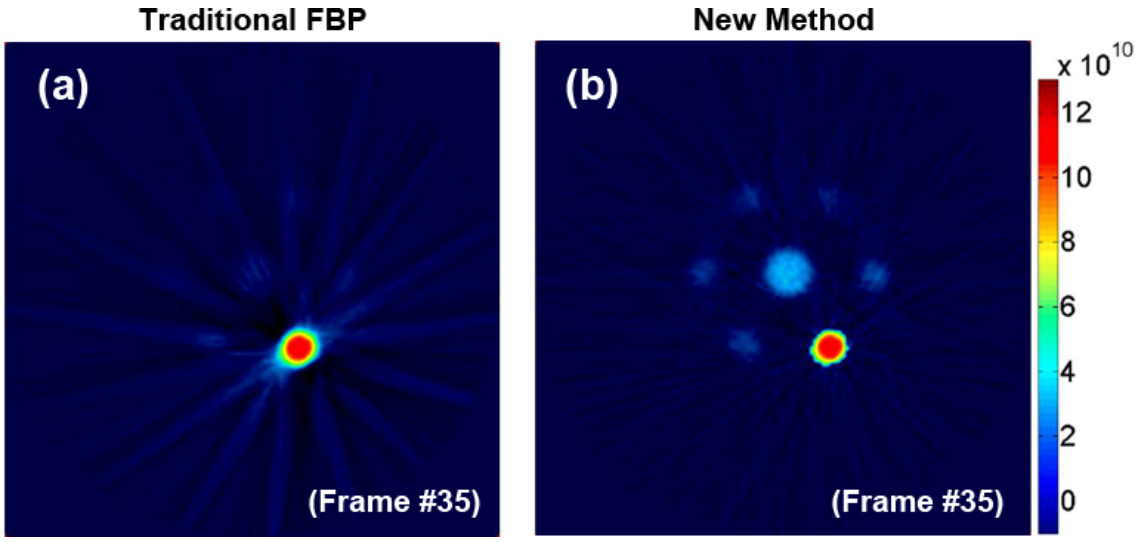

Figure 2.12: An exemplary frame (frame #35) of the reconstructed images using (a) the traditional FBP method and (b) the proposed method.

2.5 Discussion

This chapter proposes a framework to reduce severe streak artifacts in PET images reconstructed using FBP. The framework utilizes the temporal information of tracer *in vivo* to identify, extract and process part of the PET data, which normally lead to severe artifacts, before the final image generation. The evaluation results of simulation and phantom studies show a clear improvement in image quality as well as in quantitative accuracy, as compared to the results from the original FBP method.

Generally, the new method is effective for reducing severe streak artifacts. As shown in Fig. 2.3, when the tracer accumulates in the bladder over time, the difference between incomparable signal levels increases. Consequently a stronger streak effect and a larger RMSE are shown in the traditional FBP images as time goes by (Fig. 2.9). By employing the framework, the streak artifacts in the reconstructed images are consistently suppressed regardless of time and the RMSE is kept at a low level.

It is known that the fewer number of projections used in FBP reconstruction, the more severe streak artifacts will be observed in the images. Our evaluation results show that the performance of the new method is less affected by the projection number. For example, for the tracer activity distributions, an increment of RMSE by 78% was obtained when the projection number decreased from 128 to 32 using the traditional FBP, while for the proposed method, the RMSE was increased by 32%. Thus the proposed methods was found more effective for correcting FBP images when fewer projections were used. For 128 projections, a 75% reduction in

RMSE of the reconstructed tracer activity distribution images was achieved using the proposed method. For 32 projections, this number was increased to 81%. Consistent results have been observed for the investigated parametric images; the improvements in RMSE were more obvious when 32 projections was used for estimating K_1 and k_3.

The ℓ_2-norm regularization term in Eqn. 2.3 was introduced to achieve a better decomposition of the sinogram and consequently a better artifacts reduction. As shown in Fig. 2.10, less RMSE may be achieved when the regularization term $\beta > 0$. In addition, though β is case dependent, an optimum can be usually found within a relatively wide range (in this simulation study, $\beta : 220 \sim 330$); thus, the selection of β does not influence the result significantly.

To sum up, this chapter proposes a time-activity curve based sinogram decomposition algorithm for the reduction of streak artifacts in FBP reconstructions. The simulation as well as physical phantom results have shown that the proposed method can effectively reduce the severe artifacts caused by the incomparable signal levels existing in the reconstructed images. The corrected images are of better visual quality as well as quantification accuracy (with lower RMSE). The proposed method is limited to applications when dynamic imaging is available. However, dynamic measure is gaining more and more attention for PET applications as well as for other imaging modalities. For instance, the dynamic contrast-enhanced imaging techniques (e.g., DCE-MRI or DCE-CT) also requires the temporal information of biomarks for physiological investigations [77,78]. Thus the proposed method has the potential to be extended to other fields and applications.

3

Direct Parametric Image Reconstruction for Rapid Multi-tracer PET

Multi-tracer PET aims to investigate the tumor phenotype from different perspectives. The complementary tracer physiologies can significantly improve in tumor detection and diagnosis [79–83]. However, multi-tracer PET imaging is achieved in practice by separate scans, since overlapping tracers cannot be physically differentiated. Recently, a rapid multi-tracer PET technique was developed, enabling the detection of multiple tracers within one scan. The recovery of individual components is achieved by investigating physiologically distinct tracer pharmacokinetics. Nevertheless, this technique is limited by the low SNR of PET measurements and the high complexity of kinetic models. This chapter presents a direct parametric image reconstruction for the rapid multi-tracer PET (MT-DPIR) method to overcome these problems. Following the idea of DPIR, MT-DPIR utilizes the temporal information of the mixed signal and integrates it into iterative reconstruction. The proposed MT-DPIR method has been verified using numerical simulations as well as preclinical PET data. Its performance was compared with indirect parametric image generation methods.

Part of this work has been published in [84, 85].

3.1 Multi-Tracer PET imaging

The physiological features of the tumor microenvironment, such as glycolysis, angiogenesis, proliferation, and hypoxia, can be captured by PET imaging using different radiolabeled tracers. In practice, multiple tracers targeted to distinct physiologies

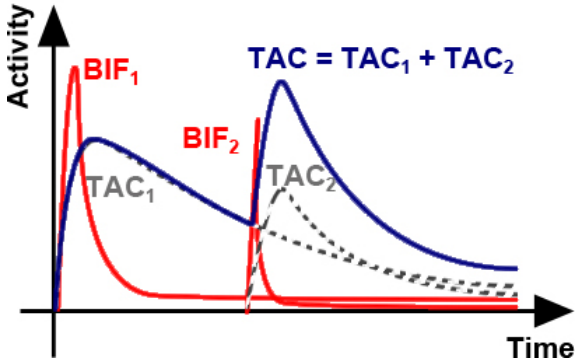

Figure 3.1: A sketch of the rapid multi-tracer PET imaging protocol (AIFs indicates tracer injections within a short time interval and a tracer TAC is measured by the summation of single tracer responses (dash lines) to the AIFs.)

can be injected into patients to obtain complementary diagnostic and therapeutic information. The clinical value of combining tracers in oncological detection, staging, localization, and individualization of cancer therapy has been confirmed in several clinical studies [79–82]. For example, the combination of [^{18}F]FDG and [^{18}F]FLT has significantly improved sensitivity and specificity in the diagnosis of lung nodules [83].

However, as photons originating from different PET tracers will be detected at the same energy level (∼511 KeV), the overlapping sources cannot be physically discriminated. In practice, multi-tracer PET imaging is achieved by scanning tracers separately, which involves waiting for the full decay and clearance of each tracer, meaning the whole procedure takes days. This also imposes additional doses on the patient due to multiple CT scans of PET/CT as well as increased labor and financial costs. The possible physiological and anatomical discrepancy due to separate scans may even reduce the expected clinical value. These limitations hamper a wider application of multi-tracer PET imaging.

Dynamic rapid multi-tracer PET imaging aims to distinguish the physically identical signals of different tracers, based on the intrinsic differences of tracer pharmacokinetics. As shown in Fig. 3.1, in practice tracers are injected sequentially with a short time interval (e.g., 10-15 mins) in between the administrations. The activities of different tracers are separated by fitting a traditional multi-tracer model [86–88] (Sec. 3.2) to reconstructed dynamic PET images [86–96]. However, this method suffers from the high complexity of the multi-tracer model and the low SNR of TACs. The poor quality of the model fitting makes the separation of tracers unstable and failure prone.

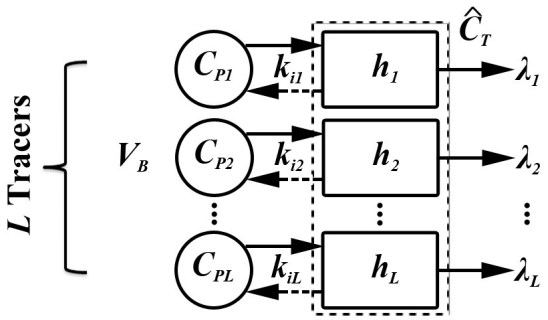

Figure 3.2: A sketch illustrating the multi-tracer model

3.2 Multi-Tracer Pharmacokinetic Model

With the application of rapid multi-tracer PET imaging, the tracer separation task becomes a mathematical fitting problem. To model the temporal development of the mixed uptake of L tracers, the pharmacokinetic model is defined as the linear superposition of the corresponding L single tracer models [90, 93] as illustrated in Fig. 3.2. The measured tracer activity concentrations C_t for each voxel at time t is then expressed as:

$$\hat{C}_t(\mathbf{p}) = V_B \bar{C}_{Pt} + \sum_{l=1}^{L} h_{lt}(\mathbf{p}_l, \lambda_l) \otimes C_{Plt} \tag{3.1}$$

where $h_{lt}(\mathbf{p}_l, \lambda_l)$ is the impulse response function of the l^{th} tracer, specified by a given kinetic model and corresponding parameters $\mathbf{p}_l$, and the radioactive decay rate λ_l (min^{-1}) and $\bar{C}_{Pt} \triangleq \sum_{l=1}^{L} C_{Plt}$ denotes the superposition of AIFs.

Eqn. 3.1 is specified by certain tracer combinations. The model complexity is decided by the involved single tracer models. Approximations have been made to simplify the mathematical description of tracer kinetics. However, a pharmacokinetic model for a single tracer needs to consider factors such as delivery, metabolism, and excretion of the tracer to achieve acceptable accuracy [45]. When more than one tracer is involved, the model complexity quickly increases along with the expansion of the parameter space. Kinetic fitting of such a complicated multi-tracer model is known to be challenging for typical optimization algorithms.

3.3 Direct Parametric Image Reconstruction for Rapid Multi-Tracer PET

This section presents a direct parametric image reconstruction for multi-tracer PET (MT-DPIR) algorithm. This proposed method aims to improve the separation of rapid multi-tracer PET signals by reducing the model complexity meanwhile enhancing the SNR for parametric image estimations. In general, it is achieved by integrating a nonlinear multi-tracer model into the reconstruction procedure to estimate parametric images directly from projection data (DPIR, refer to Sec. 1.4). Particularly, the model is beforehand analytically transformed into a "reduced parameter space" (RPS reformulation) to achieve the reduction of parameter dimensionality. By evaluating the estimated kinetic parameters, individual tracer components are recovered from the mixed measurements through modeling. The new algorithm, including the RPS reformulation technique and the DPIR method for integrating nonlinear multi-tracer models, is described as follows.

3.3.1 RPS reformulation

The formulation of pharmacokinetic models in the reduced parameter space is a concept meant to improve the nonlinear model fitting [97, 98]. It utilizes the measured TAC as prior knowledge to regularize the model in Eqn. 3.1. The linear parameters of the model can therefore be analytically expressed using nonlinear parameters to achieve dimensionality reduction. The resulting RPS model usually possesses an objective function with less than half of the original number of fitting parameters. With a lower parameter dimension and a consequently less complicated fitting environment, the optimization procedure of kinetic modeling has been reported to reach fitting solutions quickly and robustly.

The mathematical descriptions of the RPS reformulation are presented here. To achieve parameter reduction, the kinetic model $\hat{C}_t$ in Eqn. 3.1 is expressed using the generalized kinetic model formulation, which enables the maximal separation of the linear and nonlinear terms of the kinetic model [97, 99]:

$$\hat{C}_t(\boldsymbol{\theta}, \boldsymbol{\nu}) = \theta_B \bar{C}_{Pt} + \sum_{l=1}^{L} [\theta_{Pl} \tilde{C}_{Plt} + \theta_{al} F_{alt}(\nu_{al}) + \theta_{bl} F_{blt}(\nu_{bl})] \tag{3.2}$$

$$\begin{cases} \tilde{C}_{Plt} \triangleq e^{-\lambda_l t} \otimes C_{Plt} \\ F_{alt}(\nu_{al}) \triangleq e^{-(\nu_{al})t} \otimes C_{Plt} \\ F_{blt}(\nu_{bl}) \triangleq e^{-(\nu_{bl})t} \otimes C_{Plt} \end{cases} \tag{3.3}$$

where $[\theta_B, \theta_{Pl}, \theta_{al}, \theta_{bl}]^T$ and $[\nu_{al}, \nu_{bl}]^T$ are intermediate parameters composed of traditional kinetic constants $\mathbf{p}_l$; T is the transpose operator. The modeled $\hat{C}_t(\boldsymbol{\theta}, \boldsymbol{\nu})$ is then expressed in the matrix format:

$$\hat{C}_t(\boldsymbol{\theta}, \boldsymbol{\nu}) = \boldsymbol{\theta}^T \mathbf{f}_t(\boldsymbol{\nu}) = \underbrace{[\theta_B, \theta_{P1}, \theta_{a1}, \theta_{b1}, \cdots, \theta_{PL}, \theta_{aL}, \theta_{bL}]}_{\boldsymbol{\theta}} \underbrace{\begin{bmatrix} \bar{C}_{Pt} \\ \tilde{C}_{P1t} \\ F_{a1t} \\ F_{b1t} \\ \cdots \\ \tilde{C}_{PLt} \\ F_{aL} \\ F_{bLt} \end{bmatrix}}_{\mathbf{f}} \tag{3.4}$$

where $\boldsymbol{\theta} = [\theta_B, \theta_{P1}, \theta_{a1}, \theta_{b1}, \cdots, \theta_{PL}, \theta_{aL}, \theta_{bL}]^T$ denotes the linear parameters of the L tracers; $\mathbf{f}_t(\boldsymbol{\nu})$ denotes the nonlinear parts $([\bar{C}_{Pt}, \tilde{C}_{P1t}, F_{a1t}, F_{b1t}, \cdots, \tilde{C}_{PLt}, F_{aL}, F_{bLt}]^T)$, as a function of nonlinear parameters $\boldsymbol{\nu} = [\nu_{a1}, \nu_{b1}, \cdots, \nu_{aL}, \nu_{bL}]$.

As shown in Eqn. 3.4, by presenting the model $\hat{C}$ with intermediate parameters, the linear parts $\boldsymbol{\theta}$ and nonlinear parts $\mathbf{f}_t$ are separable for RPS reformulation. To express linear parameters with nonlinear ones, additional information is required to set up the relationship between parameters. The RPS technique employs the measured curve C_t. Ideally, C_t is noise-free and represents the ground truth (GT). The weighted sum square error (WSSE) of the modeled $\hat{C}_t$ with respect to GT is then measured by:

$$WSSE = \sum_{t=1}^{N_T} w_t (C_t - \hat{C}_t)^2 \tag{3.5}$$

To minimize Eqn. 3.5, the derivative of WSSE to each linear parameter in vector $\boldsymbol{\theta}$ is measured and set to 0. It deduces:

$$\mathbf{M}\boldsymbol{\theta} = \mathbf{z} \tag{3.6}$$

where $\mathbf{M}$ is a symmetric matrix and $\mathbf{z}$ is a vector containing C_t for the estimation of the linear parameter $\boldsymbol{\theta}$:

$$\mathbf{M} = \sum_t^{N_T} w_t \begin{bmatrix} (\bar{C}_{Pt})^2 & \tilde{C}_{P1t}\bar{C}_{Pt} & F_{a1t}\bar{C}_{Pt} & F_{b1t}\bar{C}_{Pt} & \dots \\ . & (\tilde{C}_{P1t})^2 & F_{a1t}\tilde{C}_{P1t} & F_{b1t}\tilde{C}_{P1t} & \dots \\ . & . & (F_{a1t})^2 & F_{b1t}F_{a1t} & \dots \\ . & . & . & (F_{b1t})^2 & \dots \\ \vdots & \vdots & \vdots & \vdots & \dots \end{bmatrix} \tag{3.7}$$

$$\mathbf{z} = \sum_t^{N_T} w_t C_t [\ \bar{C}_{Pt} \quad \tilde{C}_{P1t} \quad F_{a1t} \quad F_{b1t} \quad \dots\ ]^T \tag{3.8}$$

By substituting the linear parameters $\boldsymbol{\theta}$ in Eqn. 3.4 with $\mathbf{M}^{-1}\mathbf{z}$, the reformulated mode is expressed as:

$$\hat{C}_t(\boldsymbol{\nu}) = [\mathbf{M}^{-1}\mathbf{z}]^T \mathbf{f}_t(\boldsymbol{\nu}) \tag{3.9}$$

Compared to the traditional model (referred to "the Trad-Model" for short) in Eqn. 3.1, the reformulated multi-tracer model ("the RPS-Model") $\hat{C}_t(\boldsymbol{\nu})$ is reduced to only non-linear parameters $\boldsymbol{\nu}$.

The reduced parameter space formulation is in general not restricted to a special type of pharmacokinetic model, and it can be applied to various tracers with different pharmacokinetics. In clinical practice, the most popularly applied PET tracers are those with specific binding, which can be typically modeled with the general two-tissue compartment model as introduced in Sec. 1.3.1. Thus, an exemplary realization is demonstrated of the combination of L tracers modeled with two-tissue compartment models. It is suitable for the combination of a variety of PET tracers, such as [^{18}F]FDG, [^{18}F]FLT, [^{18}F]FET, [^{11}C]MET, [^{11}C]PiB and [^{18}F]Florbetapir, which cover a wide scope of applications in oncology and neurology.

3.3.1.1 RPS reformulation of the multi-tracer irreversible two-tissue compartment model

The traditional irreversible two-tissue compartment model for the l^{th} tracer is presented in Eqn. 1.16, Sec. 1.3. Considering the L tracers' case, the model is expressed as:

$$\begin{aligned}
\hat{C}_t &= V_B \textstyle\sum_{l=1}^{L} C_{Plt} + \sum_{l=1}^{L} \{ \frac{K_{1l}k_{3l}}{k_{2l}+k_{3l}} \int_0^t C_{Plt} dt + \frac{K_{1l}k_{2l}}{k_{2l}+k_{3l}} \int_0^t C_{Plt} e^{-(k_{2l}+k_{3l}+\lambda_l)(t-\tau)} d\tau \} \\
&= [V_B, \tfrac{K_{11}k_{31}}{k_{21}+k_{31}}, \tfrac{K_{11}k_{21}}{k_{21}+k_{31}}, \cdots, \tfrac{K_{1L}k_{3L}}{k_{2L}+k_{3L}}, \tfrac{K_{1L}k_{2L}}{k_{2L}+k_{3L}}] \begin{bmatrix} \sum_{l=1}^{L} C_{Plt} \\ \int_0^t C_{P1t} dt \\ \int_0^t C_{Plt} e^{-(k_{2l}+k_{3l}+\lambda_l)(t-\tau)} d\tau \\ \cdots \\ \int_0^t C_{PLt} dt \\ \int_0^t C_{PLt} e^{-(k_{2L}+k_{3L}+\lambda_L)(t-\tau)} d\tau \end{bmatrix} \\
&= [\theta_B, \theta_{P1}, \theta_{a1}, \cdots, \theta_{PL}, \theta_{aL}] \begin{bmatrix} \bar{C}_{Pt} \\ \tilde{C}_{P1t} \\ F_{a1t}(\nu_{a1}) \\ \cdots \\ \tilde{C}_{PLt} \\ F_{aLt}(\nu_{aL}) \end{bmatrix}
\end{aligned} \tag{3.10}$$

Therefore the parameters $\boldsymbol{\theta}$ and $\boldsymbol{\nu}$ in the reduced parameter space are expressed as follows, considering the original kinetic parameters $\mathbf{p}$:

$$\begin{cases} \nu_{al} = k_{2l} + k_{3l} + \lambda_l \\ \nu_{bl} = 0 \\ \theta_B = V_B \\ \theta_{Pl} = \frac{K_{1l}k_{3l}}{k_{2l}+k_{3l}} \\ \theta_{al} = \frac{K_{1l}k_{21}}{k_{2l}+k_{3l}} \\ \theta_{bl} = 0 \end{cases} \tag{3.11}$$

As the parameter $\theta_{bl} = 0$, elements containing θ_{bl} in $\mathbf{M}$, $\mathbf{z}$ and $\mathbf{f}$ are omitted. In this case, $\hat{C}_t$ is reformulated to be expressed by the L nonlinear parameter $\boldsymbol{\nu} = [\nu_{a1}, \nu_{a2}, \cdots, \nu_{aL}]^T$ instead of the original $3L+1$ parameters (3 k of each tracer plus a common V_B).

The upper and lower bounds of $\boldsymbol{\nu}$ can be accordingly calculated as the constraints of $\mathbf{p}$ are given. For instance, for $\mathbf{k} \in (0, 1.0]$, the corresponding ν_{al} of the irreversible two-tissue compartment model then belong to $(\lambda_l, 1.0 + \lambda_l]$ and $(\lambda_l, 2.0 + \lambda_l]$, respectively.

3.3.1.2 RPS reformulation of the multi-tracer reversible two-tissue compartment model

The traditional reversible two-tissue compartment model for the l^{th} tracer is given in Eqn. 1.15, Sec. 1.3. Similarly, the relationship between intermediate parameters $\boldsymbol{\theta}$ and $\boldsymbol{\nu}$ with respect to $\mathbf{p}$ is given by:

$$\begin{cases} \nu_{al,bl} = \alpha_{al,bl} + \lambda_l \\ \theta_B = V_B \\ \theta_{Pl} = 0 \\ \theta_{al} = \frac{K_{1l}}{\alpha_{bl}-\alpha_{al}}(k_{3l} + k_{4l} - \alpha_{al}) \\ \theta_{bl} = \frac{K_{1l}}{\alpha_{bl}-\alpha_{al}}(\alpha_{bl} - k_{3l} - k_{4l}) \end{cases} \tag{3.12}$$

As the parameter $\theta_{Pl} = 0$, elements containing $\tilde{C}_{Plt}$ in $\mathbf{M}$, $\mathbf{z}$ and $\mathbf{f}$ are omitted. In this case, $\hat{C}_t$ is reformulated to be expressed by the $2L$ nonlinear parameter $\boldsymbol{\nu} = [\nu_{a1}, \nu_{b1}, \nu_{a2}, \nu_{b2}]^T$ instead of the original $8L+1$ parameters (4 k of each tracer plus a common V_B).

The upper and lower bounds of $\boldsymbol{\nu}$ are calculated according to the constraints of $\mathbf{k}$. For $\mathbf{k} \in (0, 1.0]$, the corresponding ν_{al} and ν_{bl} of the reversible two-tissue compartment model are given by $(\lambda_l, 1.0 + \lambda_l]$ and $(\lambda_l, 2.6180 + \lambda_l]$, respectively.

Given the model configuration, $\mathbf{M}$, $\mathbf{z}$ and $\mathbf{f}(\boldsymbol{\nu})$ can be specified for constructing the model $\hat{C}(\boldsymbol{\nu})$ with Eqn. 3.9. Usually, the parameters $\boldsymbol{\nu}$ are estimated from reconstructed PET images using typical nonlinear regression solutions [100], such as least square fitting. Once $\boldsymbol{\nu}$ is calculated, $\boldsymbol{\theta}$ is obtained from Eqn. 3.6 with the numerical inversion of matrix $\mathbf{M}$. At last, original kinetic parameters $\mathbf{p}$ can be retrieved from $\boldsymbol{\nu}$ and $\boldsymbol{\theta}$ using their relation equations.

3.3.2 DPIR for multi-tracer modeling

Though RPS reformulation can reduce parameters, the fitting quality is still not guaranteed due to the low SNR of PET measurements. The individual TACs for indirect voxel-wise fitting are of even lower SNR due to this ignorance of spatial correlations between voxels. As is known, DPIR is able to improve parameter estimations in the single tracer cases [31, 47–63, 101]. Therefore the RPS reformulation technique is integrated here with DPIR to further improve the model fitting and eventually, tracer separation.

The relationship between PET image intensity $x_m(\boldsymbol{\nu}_j)$ and activity concentration $\hat{C}(\boldsymbol{\nu}_j)$ in Eqn. 3.9 at voxel j is given by:

$$x_t(\boldsymbol{\nu}_j) = \int_{t_s}^{t_e} \hat{C}_\tau(\boldsymbol{\nu}_j) d\tau \tag{3.13}$$

where t_s and t_e are the start and end times of frame t.

To estimate the parametric images $\boldsymbol{\nu}$ from the dynamic PET measurements $\mathbf{y}$, $\hat{\boldsymbol{\nu}}$ is sought to maximize the following log-likelihood function $\mathcal{LL}(\mathbf{y}|\boldsymbol{\nu})$:

$$\mathcal{LL}(\mathbf{y}|\boldsymbol{\nu}) = \sum_{t=1}^{N_T} \sum_{i=1}^{N_{LOR}} y_{it} \log \bar{y}_{it}(\boldsymbol{\nu}) - \bar{y}_{it}(\boldsymbol{\nu}) \tag{3.14}$$

In this work, the iterative parametric image estimation algorithm proposed by Reader et al., [49] and Matthews et al., [57] is employed to approximate the log-likelihood function. The algorithm performs a voxel-wise weighted nonlinear least square (WNLS) fitting after each round of expectation-maximization (EM) reconstruction of the dynamic data set. Here the ordered-subset version of the EM update function is given [49, 57]:

$$\hat{x}_{jt}^{(n+1)} = \frac{x_t(\boldsymbol{\nu}_j^{(n)})}{\sum_{i \in I_S} a_{ij}/\alpha_i} \sum_{i \in I_S} a_{ij} \frac{\alpha_i y_{it}}{\sum_{j'} a_{ij'} x_t(\boldsymbol{\nu}_{j'}^{(n)})/\alpha_i + \mathbf{r}_t + \mathbf{s}_t} \tag{3.15}$$

and $\boldsymbol{\nu}$ is then updated by:

$$\hat{\boldsymbol{\nu}}_j = \arg\min_{\boldsymbol{\nu}} \sum_{jt} w_{jt} (\hat{x}_{jt}^{(n+1)} - x_t(\boldsymbol{\nu}_j^{(n)}))^2 \tag{3.16}$$

By substituting Eqn. 3.13 into Eqn. 3.16, the multi-tracer model $\hat{C}_t(\boldsymbol{\nu})$ is integrated into the dynamic PET reconstruction procedure. Eqn. 3.16 resembles a 1D curve fitting problem and can be solved using numerical optimization methods. Here, the weighted nonlinear least square fitting is performed, for each iteration directly after the update of all OSEM subsets. The weighting factor is defined as $w_{jt} = (x_t(\boldsymbol{\nu}_j^{(n)}))^{-1}$ [57]. After updating $\boldsymbol{\nu}$, the $\hat{C}_t(\boldsymbol{\nu})$ for each image voxel is calculated with Eqn. 3.9 to estimate $x_t(\boldsymbol{\nu}_j^{(n)})$ as the input of the next EM iteration.

3.3.3 Single tracer recovery

After regression, linear parameters $\boldsymbol{\theta}$ are calculated by $\mathbf{M}^{-1}\mathbf{z}$. The inversion of $\mathbf{M}$ can be computed with common numerical methods. Here the singular value decomposition (SVD) [46] is used. Kinetic constants $\mathbf{p}$ can then be retrieved accordingly from $\boldsymbol{\theta}$ and $\boldsymbol{\nu}$ with their relative equations specified by the tracer models.

The dynamic activity distributions of individual tracers are recovered by applying the corresponding single tracer models to the estimated parameter sets. This can be performed on either the RPS-Model with intermediate parameters $\boldsymbol{\theta}$ and $\boldsymbol{\nu}$ using Eqn. 3.9, or on the Trad-Model with the retrieved $\mathbf{p}$ using Eqn. 3.1. In this work single tracer activity distributions are calculated directly from $\boldsymbol{\theta}$ and $\boldsymbol{\nu}$ to avoid possible numerical errors due to the calculation of $\mathbf{p}$.

3.4 Evaluation of the Algorithm

The proposed direct parametric image reconstruction method for multi-tracer PET imaging (MT-DPIR) was validated using numerical simulations as well as preclinical PET measurements. The respective contributions of using RPS reformulation and DPIR on multi-tracer separation are tested in Sec. 3.4.1& 3.4.2. Following by the evaluation of the integral performance of MT-DPIR as compared to the state-off-art indirect parametric image generation method with the traditional multi-tracer model based on simulation data in Sec. 3.4.3. In addition, MT-DPIR was further evaluated using the [^{18}F]FLT + [^{18}F]FDG PET measurements of 4 mice in Sec. 3.4.4 The results were compared with corresponding single [^{18}F]FDG scans of the same mice measured on 1 day before the dual tracer scan.

For proof of concept, we focused on the combination of two tracers of different isotopes (here F-18 and C-11) in simulation experiments, which requires the integration of decay constants ($\lambda_{[^{18}F]} = 6.3 \times 10^{-3}$ min^{-1}; $\lambda_{[^{11}C]} = 3.4 \times 10^{-2}$ min^{-1}) into pharmacokinetic modeling [93] and the respective corrections of decay on the recovered single tracer activity concentrations. For both tracer, the reversible two-tissue compartment model was considered for the performance evaluation. Mathematically, the implementation of the algorithm for the combination of tracers of the same

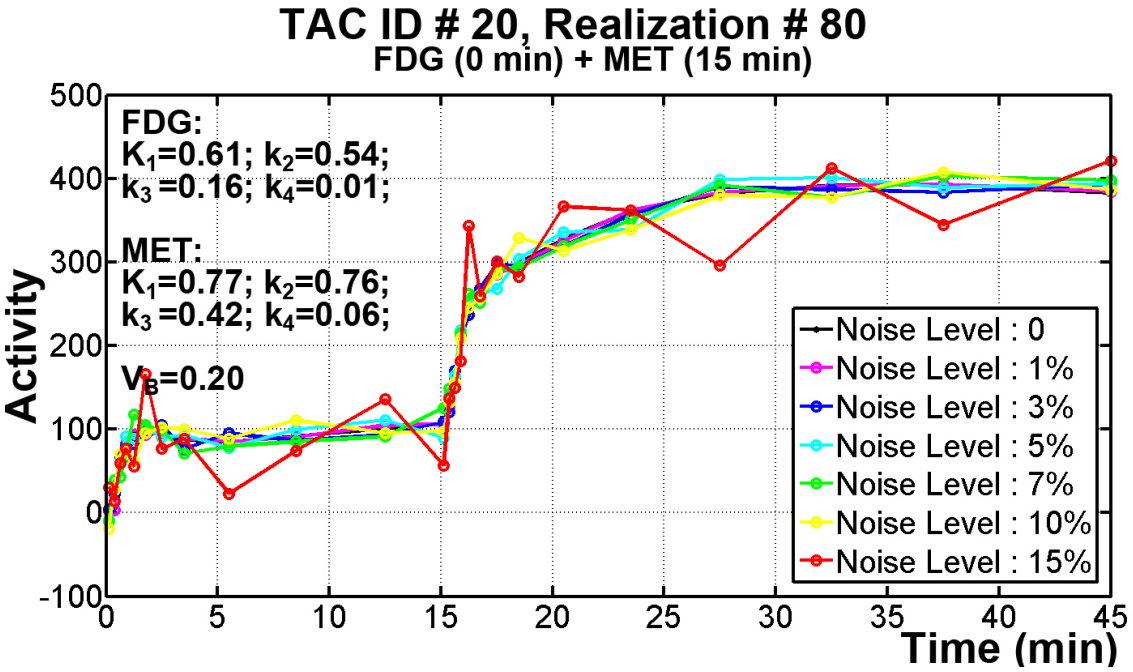

Figure 3.3: A plot of simulated TAC (TAC ID # 20, noise realization ID # 80) imposed with Gaussian noise of 6 levels (1%, 3%, 5%, 7%, 10% and 15%)

isotope or for the application of the irreversible model can be achieved with less complexity. In addition, a constant time interval (15 mins) between tracer injections was set for all tests. The influence of various time interval on tracer separations has been studied in [88].

3.4.1 Evaluation of the RPS-Model

The proposed MT-DPIR integrates a RPS-Model to reduce the modeling complexity. Although the reduction can improve the performance of the optimization procedure as presented in [97], the objective function may be sensitive to noise due to the compression of parameter space.

To investigate the influence of noise on the RPS-Model for multi-tracer signal separation, the performance of the dual tracer RPS-Model for fitting TACs with different noise levels was evaluated and compared to the performance of Trad-Model. In total, 32 sets of different FDG and MET pharmacokinetic parameters were generated randomly (0-1 for all $\mathbf{p}$ and V_B). 32 noise-free TACs were then calculated accordingly using the two reversible two-tissue compartment models. Gaussian noise of 6 noise levels (1%, 3%, 5%, 7%, 10% and 15%) was imposed [102,103] as illustrated

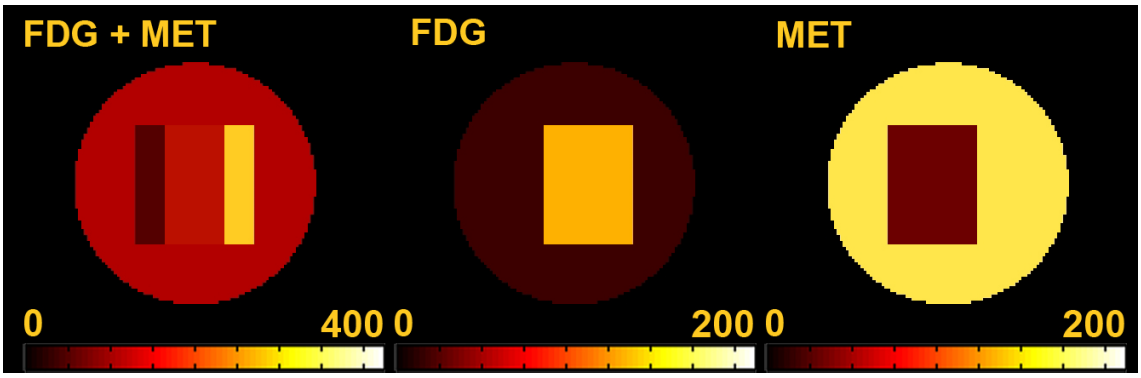

Figure 3.4: An exemplary frame of the phantom with a regular shape and different pharmacokinetics

in Fig. 3.3. For each TAC 100 noise realizations were simulated at each noise level.

Kinetic parameter estimation was achieved using nonlinear least squares method with an uniform weighting factor ($w = 1.0$) for all time points. The optimization was achieved using the trust region algorithm [104] with pre-defined stopping criteria: the maximum iterations was set to be 1000 and the optimization stopped when the variation of objective function was less than 0.00001. The initial values of $\mathbf{k}$ and V_B were set to be 0.5 and $\boldsymbol{\nu}$ values were calculated accordingly.

Individual tracer TACs were recovered with the estimated parameters and were evaluated in terms of the mean percentage error (MPE%). MPE is calculated for each investigated TAC by:

$$MPE\% = \frac{1}{N_T} \sum_{t=0}^{N_T} \frac{|\hat{C}_t - GT_t|}{GT_t} \times 100\% \tag{3.17}$$

In addition, Chi-square was measured to assess the fitting quality for each TAC. Finally, the mean and Std Dev of MPE and Chi-square were computed over 100 realizations for each TAC set. The results obtained from the RPS-Model and the Trad-Model were compared at different noise levels.

3.4.2 Evaluation of DPIR with the RPS-Model

Direct parametric image reconstruction (DPIR) has been applied to improve the performance of kinetic parameter estimations [47–63]. Here we aimed to clarify whether or not this advantage can bring additional value to the RPS-Model fitting and sequentially to tracer separation.

To investigate the complementary effect of DPIR to the RPS formulation, 50 2D phantoms with a regular structure of different FDG and MET pharmacokinet-

Table 3.1: Kinetic parameters of tissue ROIs

		Caudate	GM1	GM2	Putamen	Skin	Skull	Thalamus	WM	Tumor
FDG	K_1	0.12	0.10	0.09	0.13	0.04	0.03	0.13	0.05	0.11
	k_2	0.17	0.14	0.13	0.16	0.18	0.37	0.16	0.11	0.10
	k_3	0.19	0.17	0.18	0.17	0.01	0.02	0.14	0.05	0.15
	k_4	0.016	0.013	0.013	0.010	0.007	0.001	0.012	0.006	0.015
MET	K_1	0.06	0.08	0.11	0.09	0.16	0.07	0.07	0.04	0.13
	k_2	0.03	0.08	0.14	0.08	0.33	0.64	0.06	0.06	0.03
	k_3	0.07	0.10	0.20	0.13	0.003	0.004	0.12	0.04	0.06
	k_4	0.009	0.017	0.007	0.017	0.047	0.001	0.021	0.028	0.012
	V_B	0.101	0.103	0.140	0.092	0.042	0.047	0.152	0.026	0.173

Units: K_1: mL/min/g; k_2-k_4: min^{-1}; V_B: unitless.

ics were constructed as presented in Fig. 3.4. For each phantom the corresponding PET acquisitions were simulated with various count statistics. The phantom contains a simple square in the center with a round shape as background. To test signal separation, half of the square is assumed to take up both FDG and MET, thus an overlapping signal appears in the middle of the square. The rest takes up either FDG or MET. 50 different kinetic parameters of FDG and MET were selected randomly (0-1). Tracer TACs were generated with a dual reversible two-tissue compartment model and were assigned to corresponding ROIs of the phantom. For each phantom, dynamic PET measurements of five different count levels (6M, 30M, 60M, 120M, 600M) were simulated (20% background events) by forward projection. The simulated data were reconstructed by MT-DPIR. The post-fitting RPS-Model combined with OSEM reconstructed images was used for comparison. The simulation procedures and reconstruction configurations were the same as described later in Sec. 3.4.3.

For each phantom, the reconstructed and separated tracer activity distributions for FDG and MET were evaluated. Quantitatively, RMSE of the separated tracer activity distributions was measured with the reference GT and normalized for each dataset at the same count level. At last, the averaged results acquired from MT-DPIR and the indirect method were compared at different count statistics.

3.4.3 Evaluation of MT-DPIR

Previous tests were carried out to evaluate the respective effects of RPS-Model and DPIR on multi-tracer separations. This section presents the evaluation procedure of the integral performance of MT-DPIR, based on a slice of the realistic Zubal brain phantom [105] as shown in Fig. 3.5a. The 2D phantom (128 x 128 voxels) includes

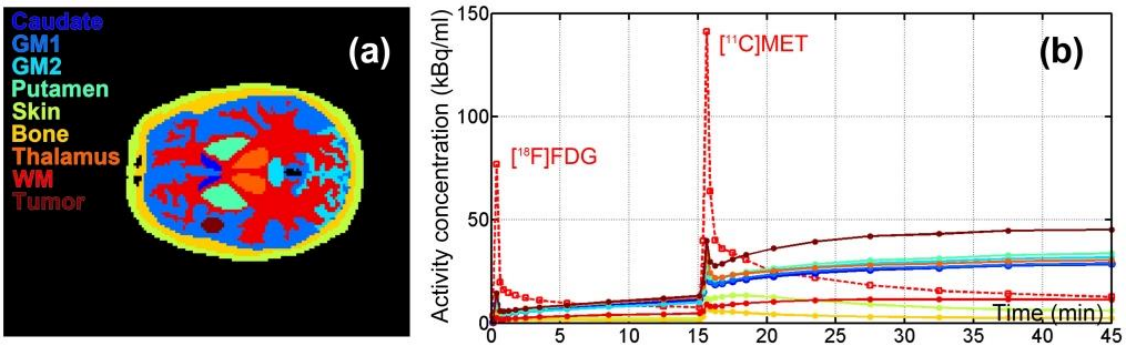

Figure 3.5: (a) The 2D brain phantom with an additional tumor; (b) a plot of AIFs (dashed line) and dual-tracer TACs for each tissue type. (A TAC's color corresponds to the region where the TAC is associated to in (a).)

gray matter (2 types), white matter, caudate, putamen, skin, skull, thalamus. A region representing a tumor was added. A set of pharmacokinetic parameters of [^{18}F]FDG and [^{11}C]MET for the phantom tissues as well as the blood input functions of each tracer were derived from literature and clinical data as listed in Tab. 3.1. Artificial blood input functions of both tracers were created along the shape of real measured AIF curves. Temporal development of tracer signals (TACs) was generated by the reversible two-tissue compartment model from the assigned kinetics for 50 minutes (25 measurement points) with an interval of 15 minutes between the tracer injections. AIFs and the obtained tissue TACs without radioactive decay correction are shown in Fig. 3.5b.

Dynamic PET measurements of the phantom were simulated using a forward projection model following the procedures described in [55, 57, 59]. The model includes object attenuation as well as the system geometry resembling the characteristics of a real clinical scanner (Siemens biograph mMR [106], spatial resolution FWHM$\sim$4.0 mm). With the scanner geometry described above, scatter events within the phantom and detectors were simulated using GATE V6 [107]. These events were then sorted out from the GATE output and formed the expectation of scatter sinogram. In this simulation, 20% scatter and 20% uniformly distributed random events were included. Poisson noise was then generated in each sinogram bin. At last, a set of dynamic sinograms (90 bins, 160 projection views and 25 frames) was generated with the expectation of total counts to be 60 million. The frame widths were set according to the measurement points and are of varying durations: 4×0.25 mins, 2×0.5 mins, 2×1 mins, 2×3 mins, 1×5 mins, 4×0.25 mins, 2×0.5 mins, 2×1 mins, 2×3 mins, 3×5 mins, and 1×10 mins. In total, fifty datasets with different noise realizations were simulated.

Based on the simulated dual-tracer acquisitions, we evaluated the performance

of MT-DPIR for tracer separation and compared with the indirect method using the Trad-Model in Eqn. 3.1. For the kinetic fitting procedure, nonlinear regression was performed using the trust region algorithm [104]. Stopping criteria were set such that the optimization procedure stopped when the variation of the objective function was less than 0.0001 or the maximum iteration number was achieved. The maximum iteration number for fitting each TAC was set to be 10 for MT-DPIR and 10 $\times$ effective iteration number $\div$ subsets number for the indirect method [59]. For the traditional kinetic model, the initial values of $\mathbf{k}$ of were set to be 0.01 for all voxels and the lower and upper bounds of each parameter were set to be 0 and 1.0. Equivalent initial values and fitting boundaries were set for the proposed method using Eqn. 3.12.

The iteration number of OSEM reconstruction may influence the performance of investigated methods on tracer separation. To compare different methods at similar bias or variance level, various effective iteration numbers (from 32 to 512 iterations) [48, 57] were evaluated. With the application of the two methods on the simulation data, the respective FDG and MET tracer information was recovered from mixed measurements. The separation results were assessed with respect to the phantom ground truth (GT). We examined the tracer activity distribution images and measured the reconstruction errors by investigating the bias-variance tradeoff [59]. Bias^2 was calculated by the squared differences between the expectation of reconstructed images and GT, while variance was the squared standard deviation at each image voxel. The calculated quantities were normalized by frames and the mean values were computed over all voxels for each investigated iteration number [108]. For PET image quantifications, we also evaluated the bias-variance tradeoff within the interested tumor region, taking into account the spatial correlation between voxels [59].

MT-DPIR and the traditional method were compared at similar bias levels with fixed iteration numbers. By evaluating the bias-variation trade-off in Fig. 3.9, 240 iterations (15×16 subsets) and 192 iterations (12×16 subsets) were used for MT-DPIR (FDG+MET Bias^2 : 0.083) and the traditional method (FDG+MET Bias^2 : 0.0832) respectively. For either method, the reconstruction at selected iteration numbers represent a relative stable result (The change of log-likelihood function $<$ 1 x 10^{-4}%).

The tracer separation results at fixed iteration numbers were then compared with GT . Spatially, we investigated the bias and standard deviation (Std Dev) images of separated tracer activity distributions. Temporally, we evaluated the separated tracer TACs from the dynamic reconstructions. Root mean square error (RMSE) was measured for the retrieved FDG and MET TACs within each region-of-interest (ROI) of the brain phantom. The parametric images ($\mathbf{k}$ and V_B) of DPIR for FDG and MET were estimated using the estimates of $\boldsymbol{\nu}$ and $\boldsymbol{\theta}$. We measured bias and standard deviation of parametric image voxels over all simulation datasets.

3.4.4 Real data validation

The performance of MT-DPIR was further evaluated on real PET scans of 4 mice with SUDHL-1 xenograft tumor using a preclinical PET/CT (Siemens, Inveon micro PET/CT). On day 1, [^{18}F]FDG (10-15 MBq) alone was injected after a CT scan. Dynamically PET data were acquired for 50 minutes. On day 2, both [^{18}F]FLT (10-15 MBq, at 0 min) and [^{18}F]FDG (10-15 MBq, at 15 min) were injected after CT for another PET acquisition of 65 minutes. 2 venous blood samples ($\approx 10\mu$L per sample) were taken and weighted directly after scanning. The activity concentration of mixed FDG+FLT isotope in the blood was measured in a gamma-counter. The activities of left ventricle (0-16 min) were extracted from the mouse data and concatenated with blood activities. A combined three exponential model [109] were applied to obtain individual AIFs of FLT and FDG. The separation of AIFs were verified by analyzing the proportion of individual tracer components in the blood using the thin layer chromatography (TLC) technique. All PET measurements were corrected for non-uniform system response, physical decay, dead time and randoms. Attenuation coefficients were generated based on the acquired CT data. For each mouse, dynamic acquisitions were rebinned into 2D sinograms using single-slice rebinning (SSRB) with 128 radial bins, 160 views, 159 direct planes and 65 frames (day 1: 39 frames) of varying durations.

For tracer separation, both MT-DPIR and the traditional methods were investigated. The iteration number of OSEM reconstruction was set to be 128 (8×16 subsets) for both methods. The derived images were composed of 128×128×159 voxels per frame at a voxel size of 0.78×0.78×0.80 mm^3. For the kinetic fitting procedure, the dual reversible two-tissue compartment model and the corresponding RPS-Model were employed. The maximum iteration number for nonlinear fitting was set to be 10 for MT-DPIR and 80 for the indirect method [59]. The initial value of $\mathbf{k}$ were set to be 0.5. Other configurations were the same as in Sec. 3.4.3.

The separated FDG and FLT activity distributions were evaluated, by comparing the FDG data acquired from single-tracer scans as a physiological reference. Tumor volumes were manually outlined based on the fusion of CT and PET images using PMOD software (version 3.2; PMOD Technologies, Zurich, Switzerland). The standardized uptake value (SUV) of outlined volumes were measured from the last frame of the FDG images separated from the mixed reconstruction. The FDG SUV results obtained from MT-DPIR and the traditional method were compared, with respect to the SUV measured from the FDG images of the single-tracer scan. It is known that normal brain has very low uptake of FLT due to the blood-brain barrier (BBB) [110,111] while it has generally high uptake of FDG. Therefore the brain SUV from separated FDG images was additionally measured to physiologically verify the separation results.

3.5 Results

3.5.1 Performance evaluation of the RPS formulation

For the tests on *the performance of the RPS-Model at different noise levels* (Sec. 3.4.1), the separation of 32 sets of noisy dual-tracer TACs with the RPS-Model was compared with the Trad-Model. As shown in Fig. 3.6, columns 1, 2 and & 3 show the results at noise levels 1%, 7% and 15%, indicating that MPE increased for both methods as the noise level increases. For low noise levels, the RPS-Model exhibites generally better performance than the traditional model at noise level 1% (noise level 7%) with on average 47% (4%) lower MPE for the mixed and separated TACs. However, as noise increases, MPE of the RPS-Model increases more quickly and the performance of the RPS-Model may be even worse than the Trad-Model.

In addition, the dual-tracer TAC fitting quality of nonlinear regression was measured by chi-square as shown in plots (d), (h) and (l). The Trad-Model may fall into local minima and resulting in bad fitting quality even when the noise level is low (noise level 1% for instance). While RPS-Model achieved constantly lower chi-square values regardless of noise levels.

3.5.2 Effect of direct parametric image reconstruction

For evaluating *the effects of DPIR on the RPS formulation and tracer separations* (Sec. 3.4.2), example tracer activity distributions of a phantom with 6 million (6M) measured counts are shown in Fig 3.7. With the limited acquisition, the indirect method may fail to separate the tracers in some voxels as demonstrated in this example. The direct method performed better and can recover single tracer information in the low SNR case. The corresponding mean absolute residual images (averaged over frames) further confirm that results from the direct method exhibit smaller differences between recovered single tracer images and the reference GT.

The mean RMSE of the recovered individual tracers at each counts level is illustrated in Fig. 3.8. The integration of DPIR generally reduced the RMSE of all the investigated situations. The improvement for the RPS-Model with DPIR is larger for the low count level than the high count level. For instance, the mean reductions of RMSE for FDG and MET respectively are 0.06 and 0.17 at 6M count level, while 83% and 65% less reductions are observed at 600M level.

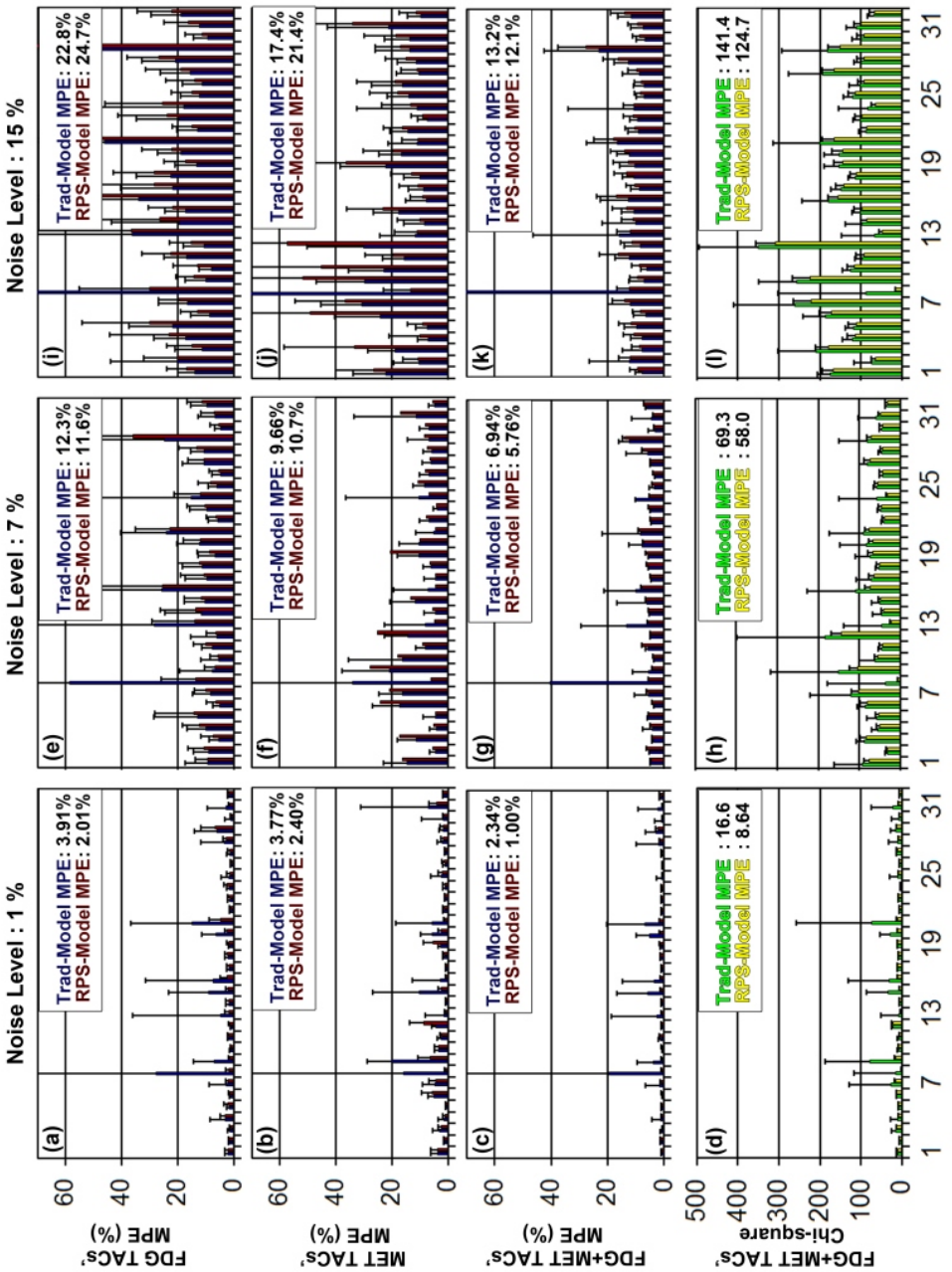

Figure 3.6: Bar plots of the normalized mean absolute error (MPE) and Chi-square of 32 TAC sets over the 100 noise realizations, investigating different noise levels: (a) noise level 1%, (b) noise level 7 % and (c) noise level 15 %

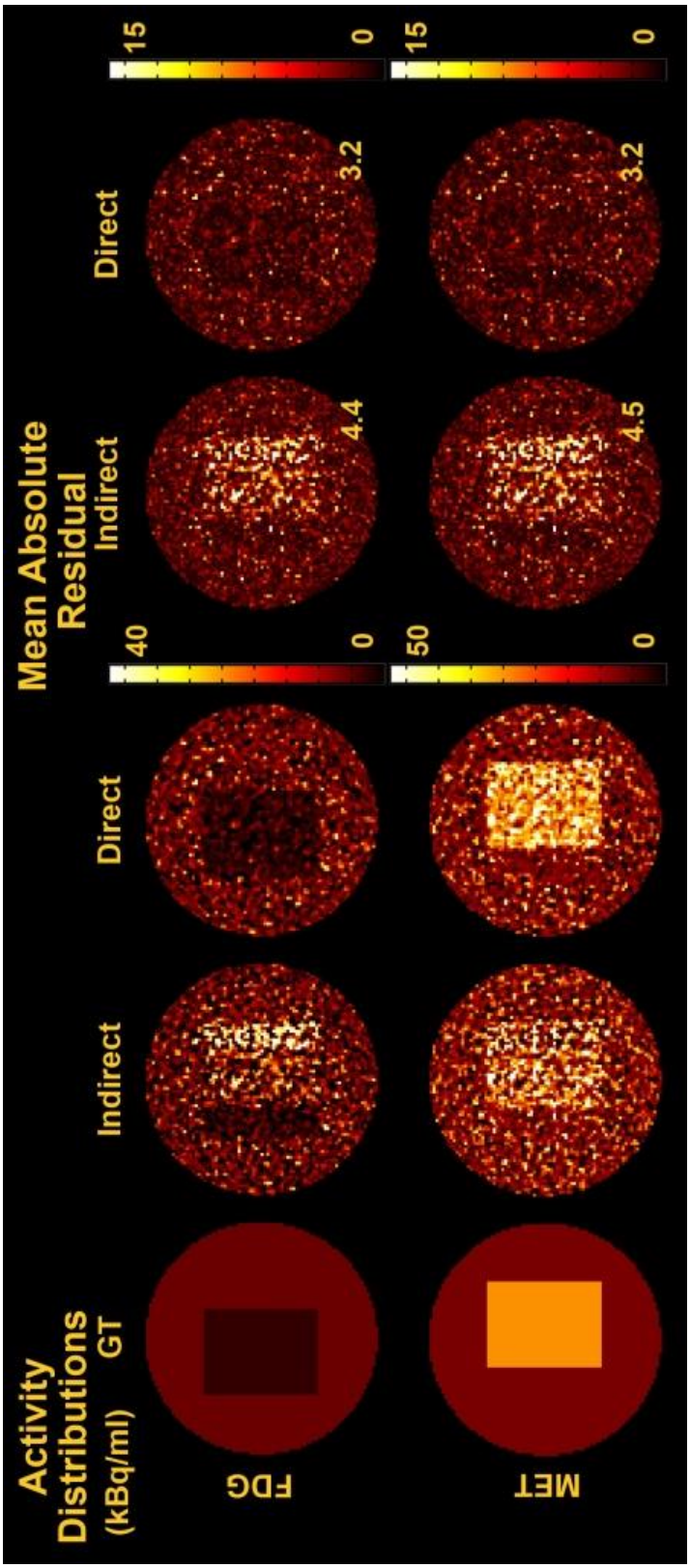

Figure 3.7: An exemplary frame ($t = 27.5$ min) of separated tracer activity distributions reconstructed from simulated measurements of 6M counts using indirect and direct methods (128 iterations) with kinetic modeling in the reduced parameter space

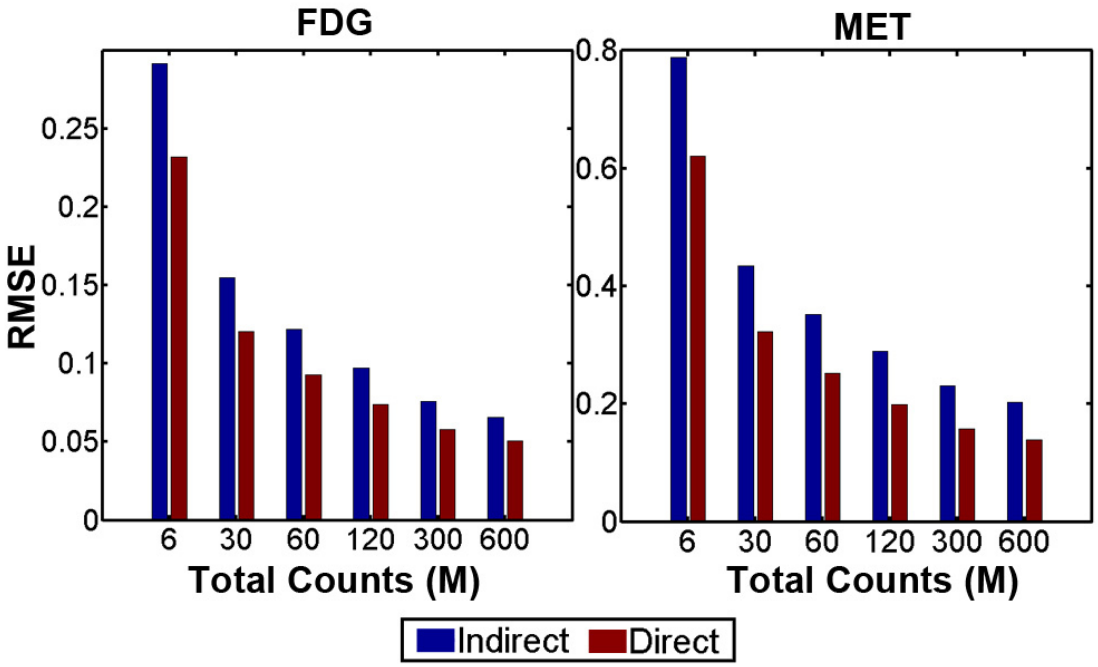

Figure 3.8: Plots of normalized RMSE calculated from separated tracer activity distributions at each count level over 50 datasets

3.5.3 MT-DPIR for tracer separations

The effect of increasing number of iterations on tracer separation is presented in Fig. 3.9a. For both MT-DPIR and the traditional methods, a decreasing bias and an increasing variance of the mixed/separated tracer images are observed as iteration proceeds. While comparing MT-DPIR and the traditional method at similar bias levels, MT-DPIR consistently has lower variance than the traditional method regardless of iteration numbers. Similar results are observed in the bias-variance trade-off plots of the tumor ROI as shown in Fig. 3.9b. To compare MT-DPIR and the traditional method at similar bias levels, 240 (FDG+MET Bias^2 : 0.0830) and 192 iterations (FDG+MET Bias^2 : 0.0832) were employed respectively in the performance evaluations.

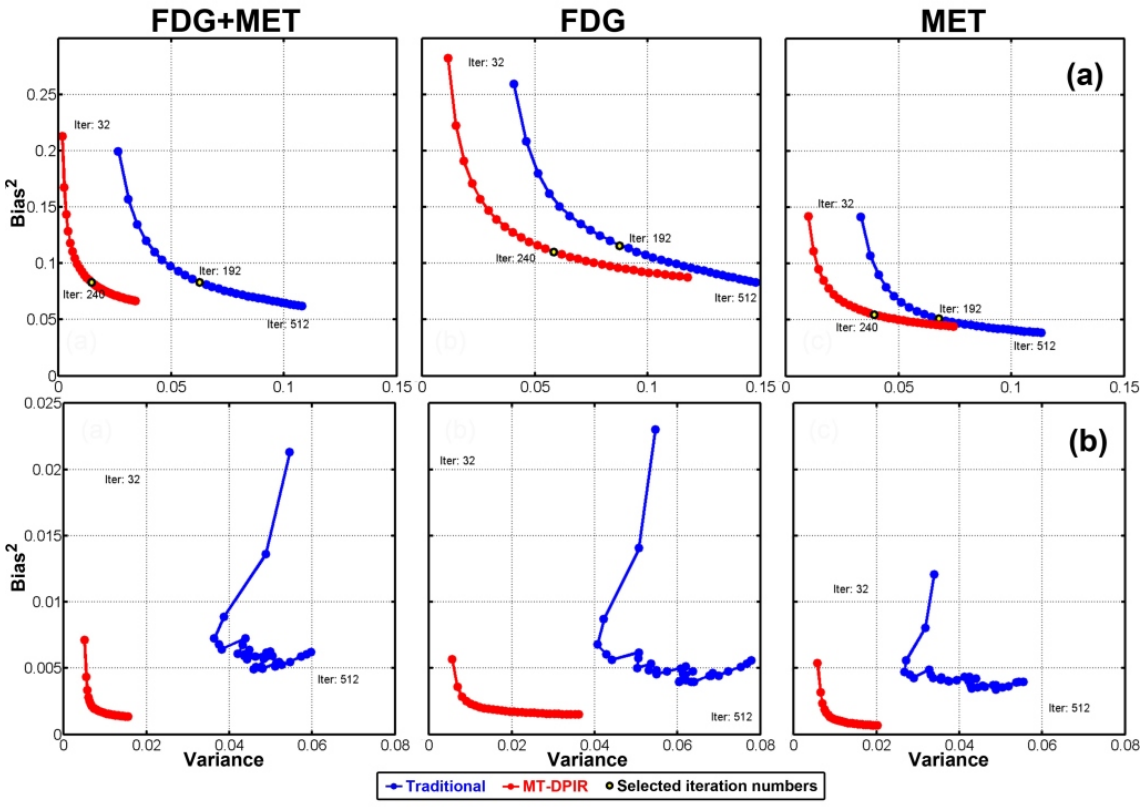

Figure 3.9: Plots of bias-variation curves of tracer activity distributions in (a) the brain phantom and (b) the tumor region with variant iterations (32 to 512) using MT-DPIR (red) and the traditional method (blue)

The separated FDG and MET activity distributions recovered from the mixed dual-tracer signals of the brain phantom are presented in Fig. 3.10 (one example frame is shown). Both, MT-DPIR and the traditional method were able to separate the overlapping tracer distributions. Separated tracer images generated by MT-DPIR shown better visual quality than those from the traditional method. The Std Dev and bias of the recovered single tracer images over the 50 datasets are shown in Fig. 3.11. The bias images for both methods are similar. Relatively high bias is observed from the ROI contours where errors may be introduced due to partial volume effects [112, 113]. A lower Std Dev are achieved with MT-DPIR than the traditional method. Over all, MT-DPIR has reduced variance for the separated FDG(MET) tracer activity distributions by 33% (42%) .

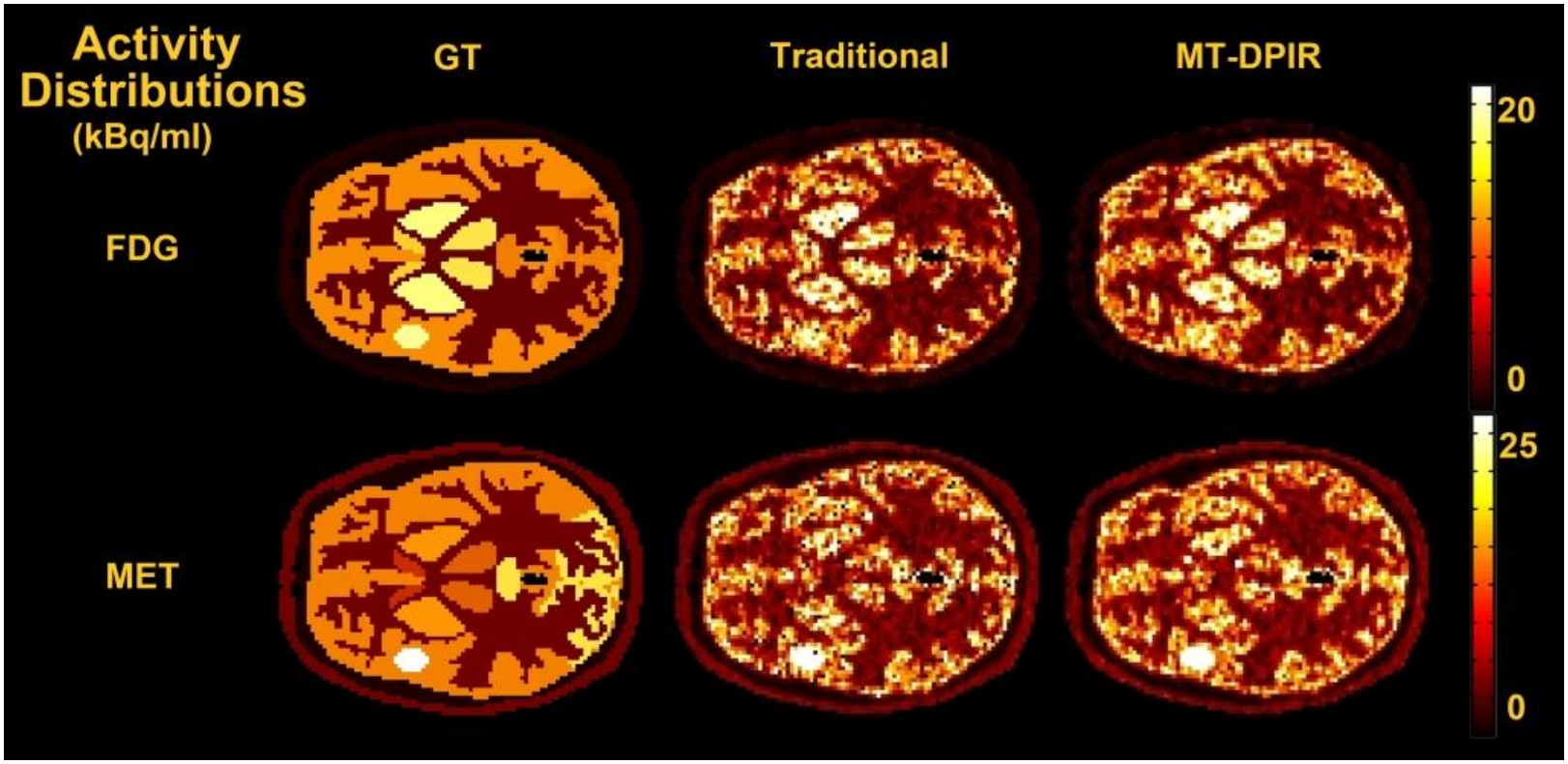

Figure 3.10: An exemplary frame ($t = 27.5$ min) of separated tracer activity distributions for FDG and MET respectively, reconstructed using the traditional method (192 iterations) and MT-DPIR (240 iterations)

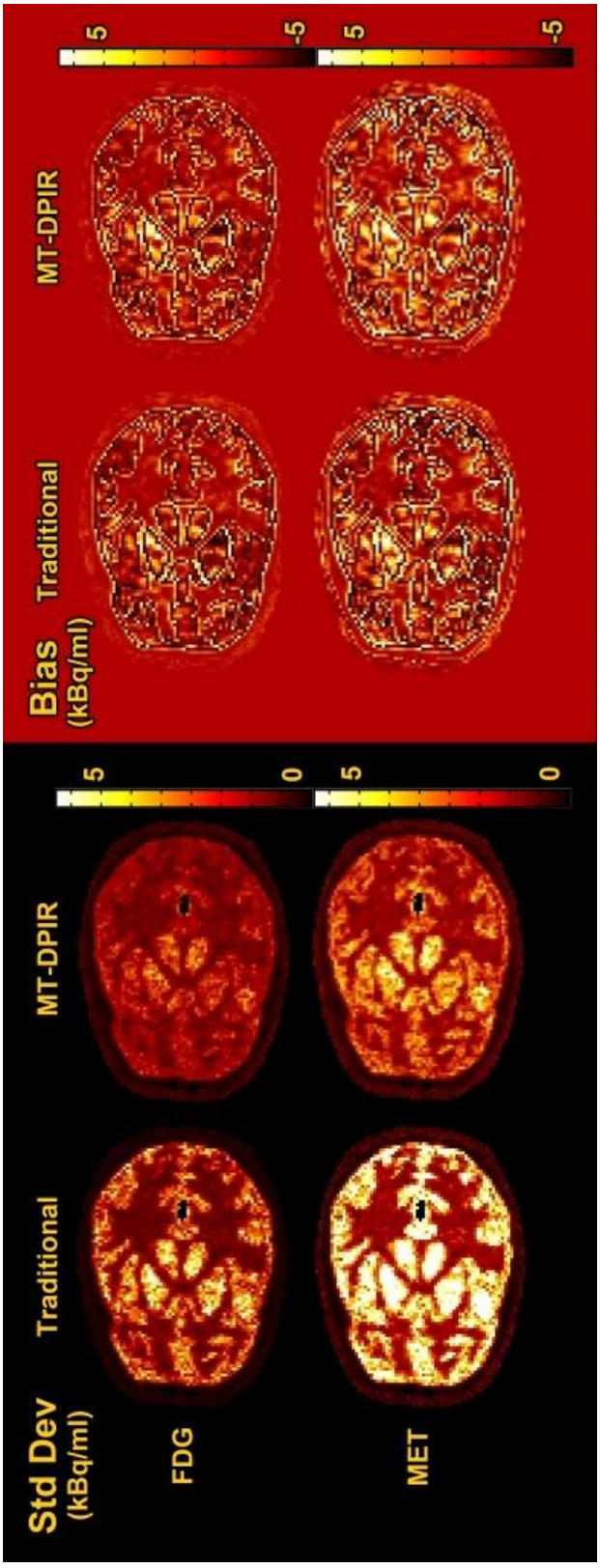

Figure 3.11: The statistical standard deviation (Std Dev) and bias maps of the example frame of tracer activity distributions ($t = 27.5$ min) generated from 50 datasets using the traditional method (192 iterations) and MT-DPIR (240 iterations)

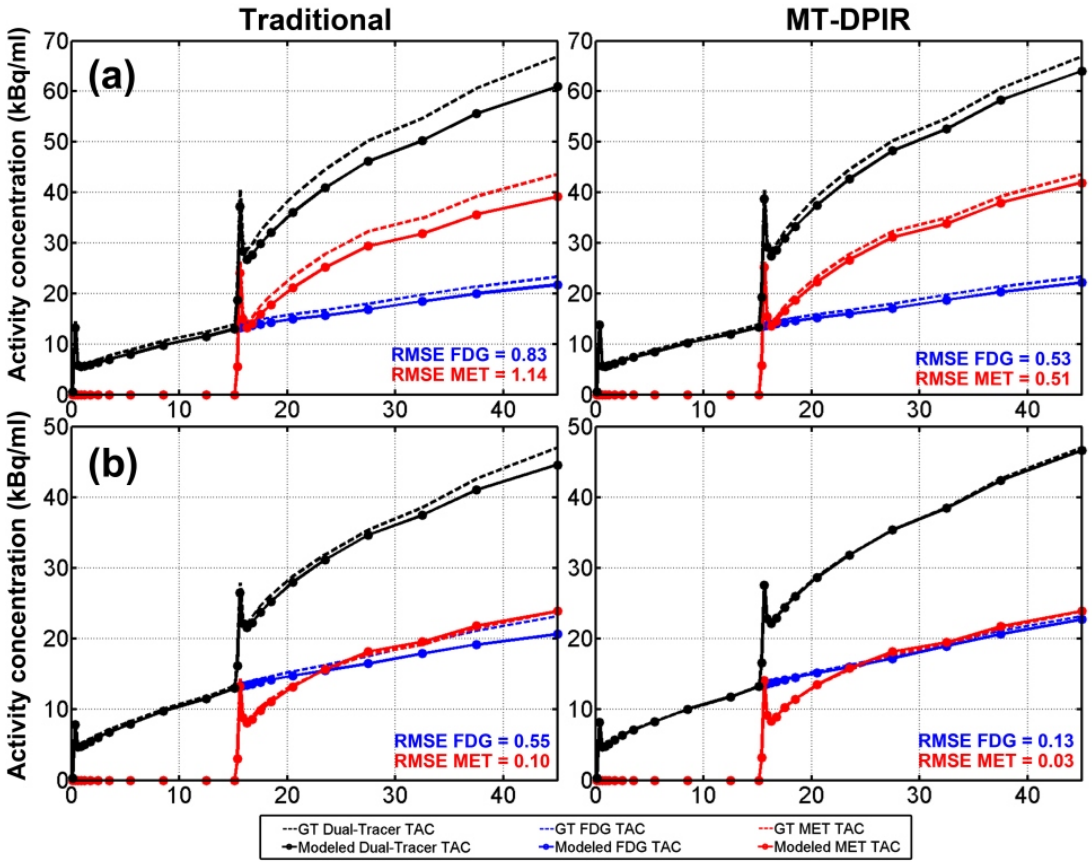

Figure 3.12: Plots of the mean TACs in the (a) tumor and (b) putamen areas over 50 datasets, showing that the FDG+MET TAC (black) was separated into 2 single FDG (blue) and MET (red) TACs, using the traditional method (192 iterations) and MT-DPIR (240 iterations) (TACs were decay corrected and compared to the ground truth (dashed lines) in terms of RMSE.)

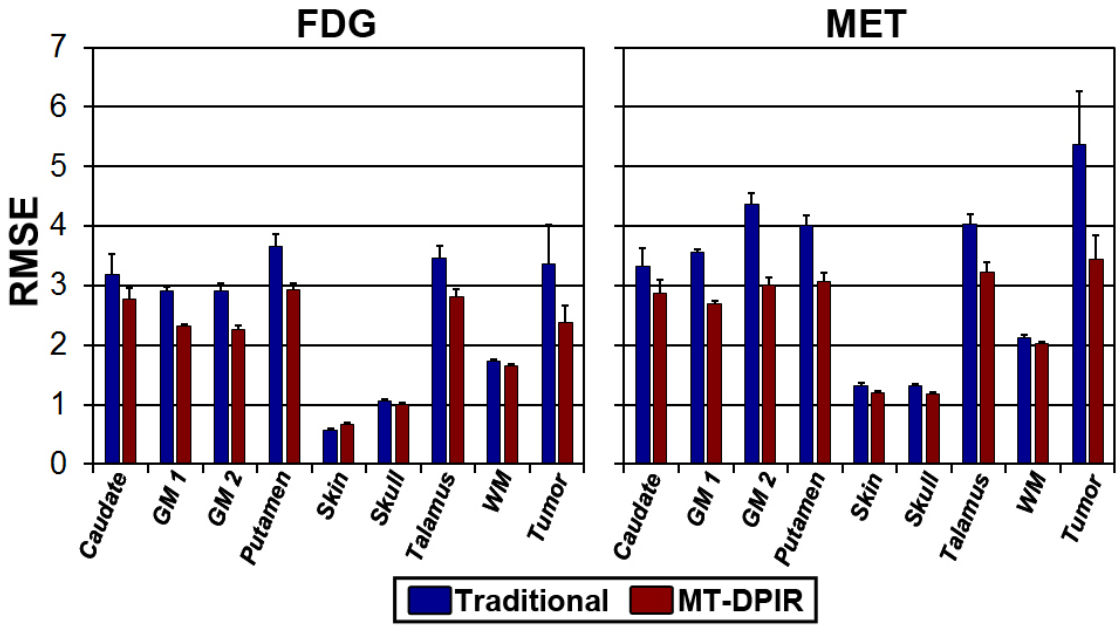

Figure 3.13: Bar plots of the root mean square error (RMSE) of TACs within each phantom regions, using the proposed MT-DPIR method (red, 240 iterations) and the traditional method (blue, 192 iterations)

Temporally, *the separated tracer TACs* within each phantom region were assessed. Fig. 3.12 demonstrates the fitting results averaged over all datasets in two example tissue regions (tumor and putamen). The reference GT curves (dashed lines) and the corresponding mean modeled TACs from the proposed and traditional methods are presented. Root mean square error (RMSE) of the mean TACs were measured for FDG and MET and are displayed accordingly. Both, MT-DPIR and the indirect method can generally resemble the reference curves. Compared to the traditional method, MT-DPIR achieved more accurate results (with less RMSE). RMSE of single tracer TACs in each phantom ROI are plotted in Fig. 3.13, where for the 50 investigated datasets, MT-DPIR was able to improve the RMSE in most ROIs. On average, a reduction of ROI RMSE by 13%±14 (FDG) and 19%±10 (MET) was achieved by MT-DPIR compared to the traditional method.

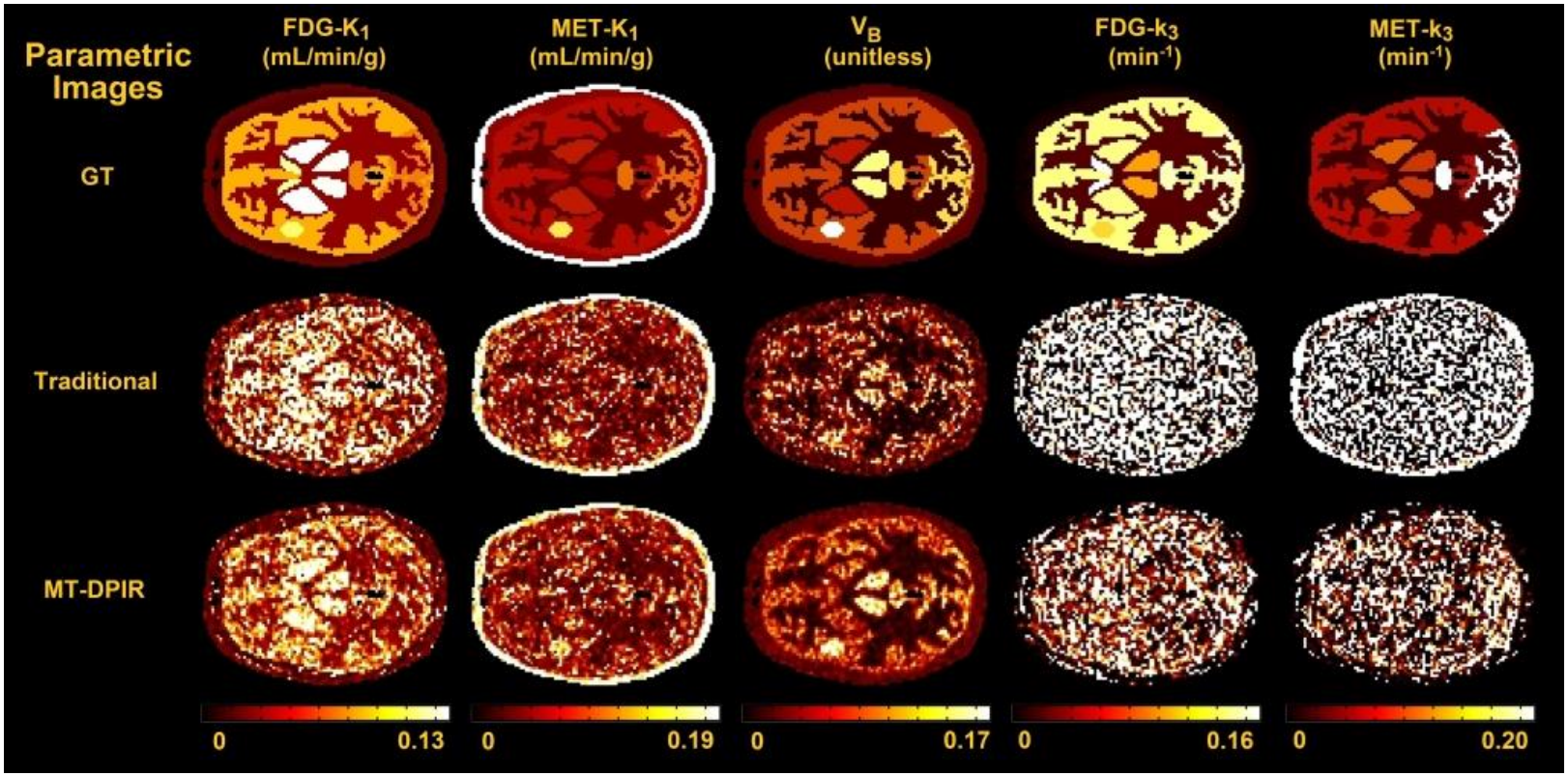

Figure 3.14: Sample parametric images of FDG and MET tracers from a randomly selected dataset, obtained from the traditional method (192 iterations) and MT-DPIR (240 iterations) (The maximum value of color bars are set to be the maximum value of $\mathbf{p}$'s as listed in Tab. 3.1.)

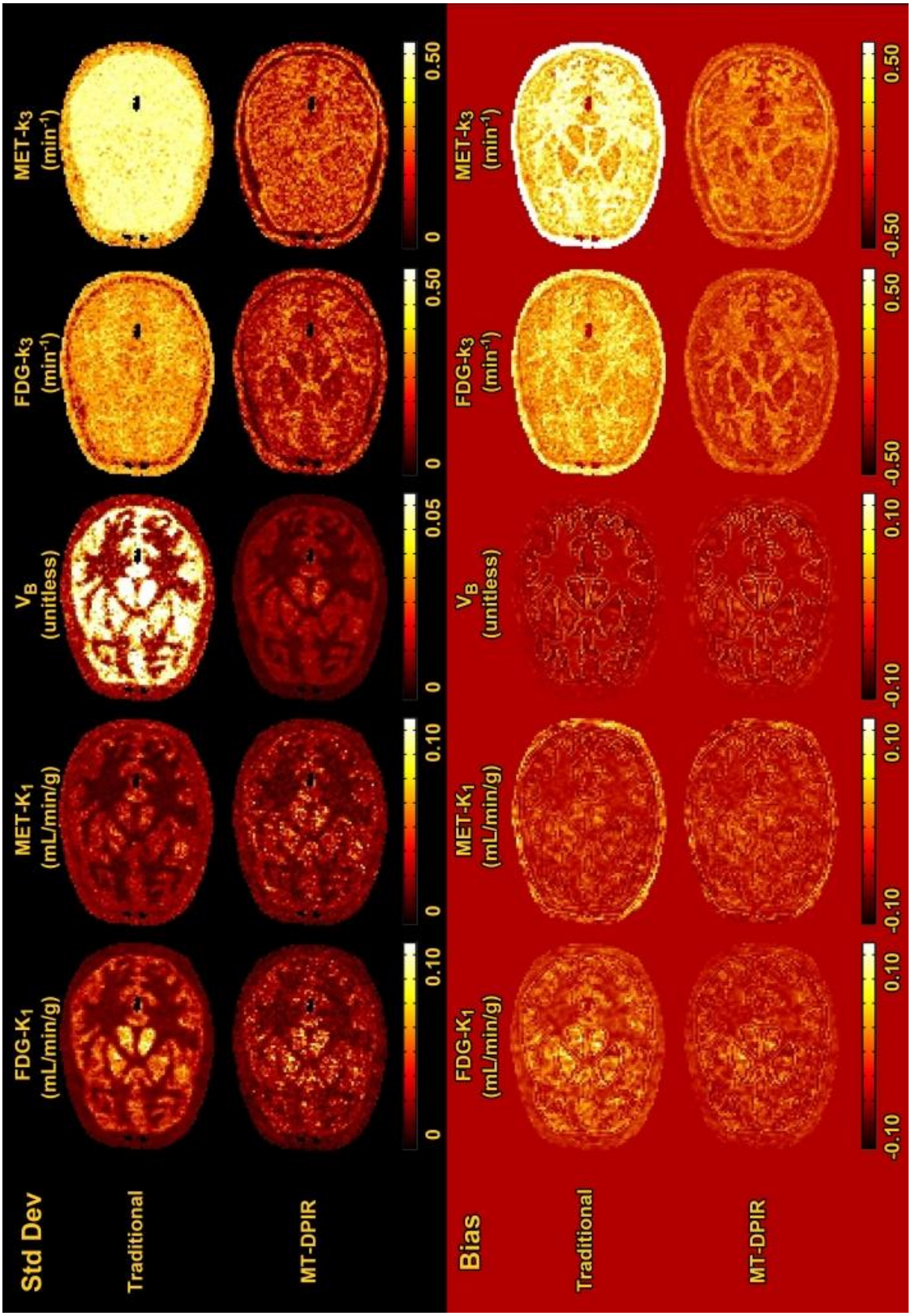

Figure 3.15: The statistical standard deviation (Std Dev) and bias maps of investigated parameters generated from 50 datasets using the traditional method (192 iterations) and MT-DPIR (240 iterations)

Table 3.2: Quantification results on parametric images over 50 noise realizations

		Parametric images								
		FDG				MET				
		K_1	k_2	k_3	k_4	K_1	k_2	k_3	k_4	V_B
standard	Traditional	0.040	0.40	0.36	0.32	0.035	0.32	0.43	0.42	0.035
deviation	**MT-DPIR**	**0.035**	**0.27**	**0.25**	**0.08**	**0.035**	**0.28**	**0.27**	**0.11**	**0.015**
Bias	Traditional	0.017	0.28	0.25	0.19	0.009	0.16	0.39	0.50	-0.005
	MT-DPIR	**0.008**	**0.08**	**0.09**	**0.02**	**0.008**	**0.10**	**0.13**	**0.03**	**-0.001**

Units: K_1: mL/min/g; k_2-k_4: min^{-1}; V_B: unitless.

3.5.4 Multi-tracer parametric image estimations

Example *parametric images* of K_1, k_3 and V_B of both FDG and MET tracers are presented in Fig. 3.14. Compared to the parametric images from the traditional method, results from MT-DPIR are relatively smooth and contain less voxels with values above the colormap maximum, which were defined as the maximum value of the corresponding kinetic parameters. However, for both methods, k_3 images are in general noisy, demonstrating that the recovery of k_2 to k_4 is still challenging.

Fig. 3.15 demonstrates the corresponding Std Dev and bias images acquired from the 50 simulated datasets. In general, parametric images reconstructed using MT-DPIR exhibit relatively lower Std Dev and bias than those from the traditional method. In particular, though the k_3 image are not satisfactory, a clear reduction in bias/Std Dev for k_3 were achieved with MT-DPIR. On average, the proposed method reduced standard deviation by 37% and bias by 65% for the resulting parametric images of the 50 simulated datasets. The mean standard deviation and bias of individual parametric image voxels are listed in Tab. 3.2.

3.5.5 Preclinical evaluation

For the preclinical data assessment (Sec. 3.4.4), the separated FLT and FDG distribution of Mice #3 are shown (one frame) in Fig. 3.16 as an example. The corresponding image of Mice #3 from the single-tracer (FDG) scan is presented as reference. In general, MT-DPIR provides relatively smoother images with less noisy points as compared to the traditional methods. Both separated FDG images have similar activity distributions as reference. In particular, the separated FLT image from MT-DPIR exhibits low uptake in the brain area, while this is not obvious in the FLT image obtained from the traditional method. The MT-DPIR results is more consistent with physiological expectations.

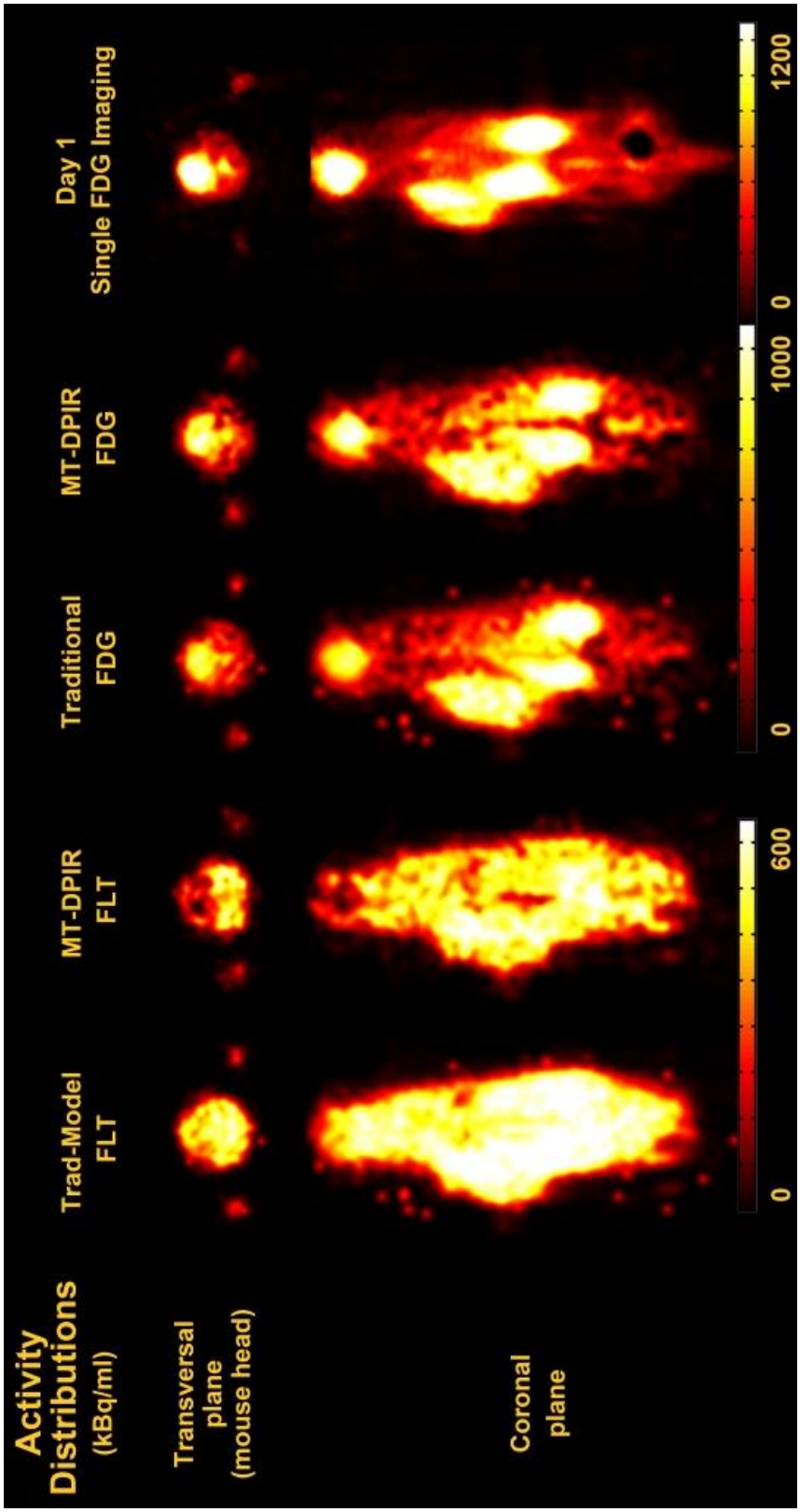

Figure 3.16: An exemplary frame ($t = 35.0$ min) of separated FLT and FDG activity distributions of Mice #3 using the traditional method (128 iterations) and MT-DPIR (128 iterations), with the FDG images (OSEM, 128 iterations) obtained from the corresponding single-tracer scan as reference

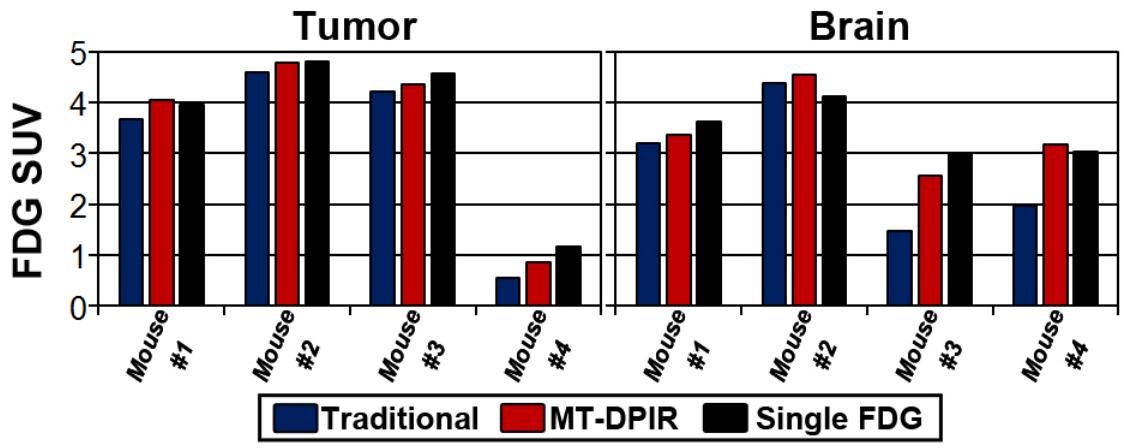

Figure 3.17: Plots of the standardized uptake values (SUV) of tumor/brain volumes outlined from the separated FDG images using the traditional method (blue, 128 iterations) or MT-DPIR (red, 128 iterations), with the reference volume SUV outlined from the single FDG tracer data (black, 128 iterations)

The FDG SUV of the tumor and brain volumes are demonstrated in Fig. 3.17. Both methods provide consistent results with the SUV measured from the single-tracer images. On average, MT-DPIR has lower absolute SUV difference to the reference in both tumor (0.16 ± 0.12) and brain (0.31 ± 0.15) volumes than the traditional method (tumor: 0.36 ± 0.18, brain: 0.81 ± 0.57).

3.6 Discussion

The identification of individual tracers from a mixed PET signal is challenging. Although the feasibility of multi-tracer pharmacokinetic modeling has been demonstrated [55], the limited SNR of PET measurements and the high complexity of fitting models still remain as the two main obstacles to a wide application of such methods. Thus, we investigated the MT-DPIR method to improve the performance of multi-tracer modeling.

3.6.1 Reformulation in reduced parameter space

Multi-tracer kinetic modeling utilizes the intrinsic pharmacokinetic differences of the physiologically distinct tracers for the recovery of individual signals from mixed PET measurements [87]. However, when more than one tracer is involved, the model complexity quickly increases along with the expansion of parameter space. Kinetic fitting of such a complicated multi-tracer model is challenging for optimization algo-

rithms. Our results in Sec. 3.5.1 show that multi-tracer pharmacokinetic modeling is unstable, sensitive to initial settings, and may suffer from local minima even at low noise level. Although some strategies may be applied to reduce local minima, such as using various initial values or even exhaustive searches, these methods are difficult to apply in clinical practice due to high computational cost.

The RPS formulation has been reported to improve the model fitting [97,98]. By expressing linear parameters using nonlinear ones, the RPS formulation normally leads to a model representation with less than half of the original number of fitting parameters. The reduction in the parameter dimensionality simplifies the topological fitting environment, and the optimization procedure of kinetic modeling has been reported to reach the solution as the original model with possibly fewer local minima [97]. This is also confirmed by our results shown in Fig. 3.6. When limited iterations were employed (without exhausted searched), the RPS-Model achieved generally lower Chi-square and lower standard deviation as compared to the Trad-Model, indicating a more stable fitting quality and less local minima for the investigated datasets.

However, the superior fitting quality of the RPS-Model may have a reduced value for tracer separation if it is employed at high noise levels. As shown in Fig. 3.6i-l, at noise level 15%, though the Chi-square of RPS-Model is still lower than the Trad-Model, a higher MPE was also obtained for either FDG+MET or separated tracer TACs. These results indicate that the performance of kinetic parameter estimation using RPS reformulation may still be restricted to cases with high SNR.

3.6.2 Direct parametric image reconstruction

It is known that the acquired number of coincident events during PET imaging is limited and errors are introduced due to attenuation, normalization, scattering, and random effects. Thus, a PET measurement usually has low SNR. Pharmacokinetic modeling on these data is often challenging. In particular, for indirect parametric image generation methods, TACs are treated independently and the spatial correlation between TACs is ignored, resulting in further limited SNR for kinetic fitting. On the other hand, direct parametric image reconstruction (DPIR) includes the kinetic modeling into reconstruction to utilize the complete 3D spatial + 1D temporal measurements simultaneously. When a nonlinear model is integrated, the spatial and temporal information is combined by cycling between reconstruction and kinetic modeling [57], which iteratively restrict/correct each other and trade off the bias and standard deviations ([49,57–59]). Thus, by exploring the spatial-temporal coherence of PET data, DPIR optimizes the SNR for both reconstruction and pharmacokinetic modeling procedures [55,56,60].

Our results show that the integration of a RPS-Model into DPIR can reduce the influence of noise and improve the performance of recovery of individual tracer signals under low SNR (Fig. 3.7 & 3.8). Thus, DPIR is beneficial or even necessary

for the application of RPS reformulation, whose performance for tracer sepration may be highly influenced under high noise levels.

3.6.3 Limitations and future work

3.6.3.1 Parametric image estimations

For the results presented in this chapter, the estimated $k_2 - k_4$ from $\boldsymbol{\nu}$ are still noisy as demonstrated in Fig. 3.14, although an improvement compared to the traditional method is observed. This can be further improved by using methods proposed in [97], adding additional constraints for the RPS-Model on the recovered $k_2 - k_4$ parameters when they are transformed back from $\boldsymbol{\nu}$ and $\boldsymbol{\theta}$. Nevertheless, in real application, the restriction added to a kinetic parameter needs to be carefully selected to avoid the introduction of errors. This can be achieved by analyzing patient data with individual tracers. For a fair comparison and also to demonstrate both the merit and limitation of the proposed algorithm, we did not include extra parameter boundaries nor extra fitting processing in this work.

3.6.3.2 Convergence properties

The convergence property and convergence speed are the two most important issues of an iterative algorithm. For both traditional and the proposed method, the employed OSEM and WNLS methods are not able to converge to the ML solution of the Poisson log-likelihood function. A better evaluation would be achieved by using the maximum likelihood expectation maximization (MLEM) algorithm combined with a more accurate optimization transfer method (e.g. [58, 59]) for parameter estimation. An ordinary subsets number was applied here to compromise on the convergence rate and computational efficiency [32, 63]. For fair comparison and simple implementation, the weighted iterative kinetic parameter estimation method was employed in MT-DPIR, which utilizes the NLS with iteration-dependent weights for parameter fitting.

To further evaluate the systematic bias that may be introduced by OSEM and WNLS as compared to MLEM. The log-likelihood differences between the 3 methods at 3 different count levels (6M, 30M and 60M) were investigated. The simulated brain phantom were reconstructed using MT-DPIR , OSEM and MLEM with variant iteration numbers (from 32 to 512 effective iterations). The plot of normalized log-likelihood function (normalized to the MLEM value at 512 iterations) at each count level is shown in Fig. 3.18.

As shown, both MT-DPIR and OSEM are biased from the MLEM results at 512 iterations. Furthermore, MT-DPIR includes WNLS and the log-likelihood is biased from the OSEM result. This problem is improved at higher count levels.

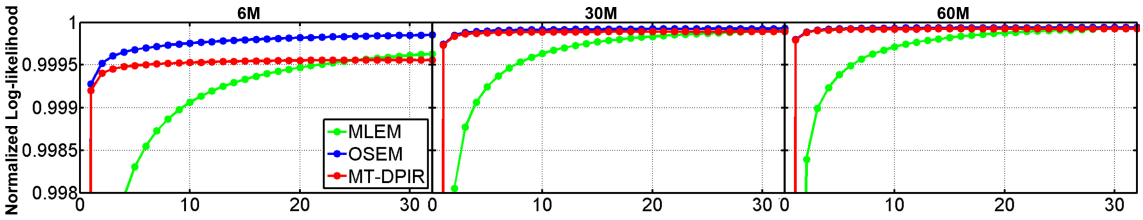

Figure 3.18: Plots of the normalized Log-likelihood comparisons of reconstructed mixed-tracer activity distributions between MLEM (reconstruction) OSEM (reconstruction) and MT-DPIR (reconstruction + WNLS fitting) methods of 1 to 32 iterations at three different noise levels

Table 3.3: The absolute differences between Log-likelihood functions

Method (iteration no.)	6M	30M	60M
MT-DPIR (32×16subsets) v. s. MLEM (512)	0.0441%	0.0106%	0.0074%
OSEM (32×16subsets) v. s. MLEM (512)	0.0148%	0.0071%	0.0059%
MT-DPIR (32×16subsets) v. s. OSEM-DPIR (32x16subsets)	0.0293%	0.0035%	0.0015%

The resulting log-likelihood functions were compared at 512 iterations as listed in Tab. 3.3. At 6M the absolute difference of the log-likelihood function between MT-DPIR and MLEM at 6M is $< 0.05\%$ (between MT-DPIR and OSEM is $< 0.02\%$). Over 30M count level, the difference is $\leq 0.01\%(< 0.01\%)$. The combination of OSEM and WNLS will not converge to the MLEM solution but can be considered as a reasonably good approximation as reported in [59, 60].

To further assess the reliability of the proposed method for PET quantification. The performance of MT-DPIR and the traditional method were evaluated at additional two count levels (6M and 30M) using the evaluation method described in 3.4.3. MT-DPIR has constantly lower variance regardless of counts level and iteration numbers as shown in Fig. 3.19 and in Tab. 3.4.

By comparing MT-DPIT and the traditional methods at the similar bias levels ($\text{Bias}^2 \approx 0.0830$), MT-DPIR has achieved 34%-76% improvements in variance of the reconstructed images for the investigated counts levels. Overall MT-DPIR can provide relatively more reliable quantification results than the traditional method.

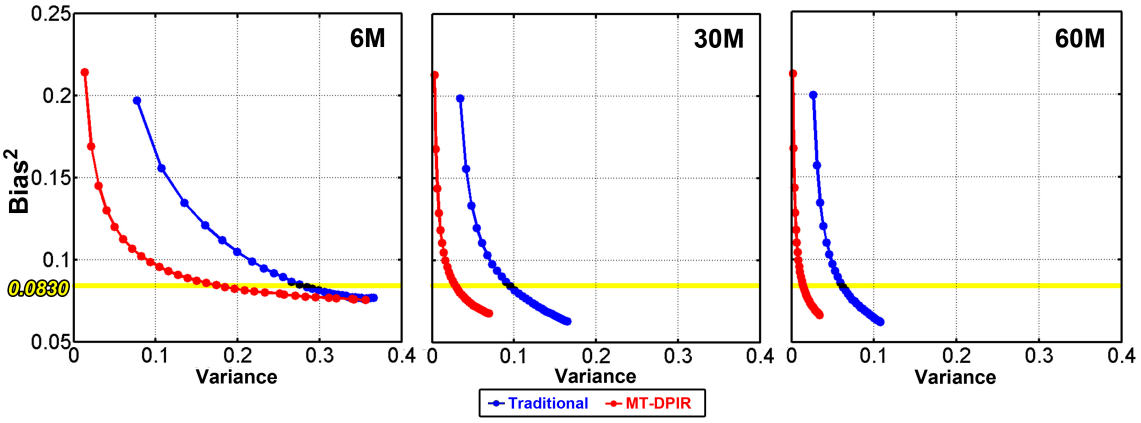

Figure 3.19: Plots of the bias-variance trade-off curved measured at different count levels (6M, 30M and 60M) with variant iteration numbers (32 to 400 iterations)

Table 3.4: Variance comparisons at similar $Bias^2$ level with different count levels

Method ($Bias^2$)	6M Variance	30M Variance	60M Variance
MT-DPIR (0.083)	0.19	0.030	0.015
Traditional (0.083)	0.29	0.098	0.063

3.6.3.3 Real data evaluations and practical applications

The preliminary evaluation uses a single FDG scan of the same mouse 1 day before as physiological reference. This is not necessarily the optimal reference due to physiological variation between the two measurements. Nevertheless, this is the optimal solution for validating a multi-tracer applications in reality.

The blood input function plays a key role in kinetic modeling for dynamic PET studies. The extraction of both AIFs for a dual-tracer study is even more challenging than in single tracer cases. The combination of image based extraction and blood samples are often used for identification of AIFs [86,88]. In the simulation studies, we focused on the validation of the algorithm and thus AIFs are assumed to be known. In real applications, we employed the thin layer chromatography for verifying the separated AIFs. This may be further improved by following the method proposed in [114].

For estimating tracer pharmacokinetics, DPIR requires dynamic acquisitions which often take about an hour. Motion may occur during clinical acquisitions which will influence the kinetic fitting and parameter estimation [115]. For direct parametric reconstruction methods, motion correction is not yet incorporated. In

our preclinical evaluations, mice were anesthetized and fixed in position during the measurement to reduce the influence of motion as much as possible. For some clinical applications, such as treatment planning before radiation therapy, patients are usually immobilized during the imaging. The proposed method can be still applied in these situations.

3.6.3.4 Algorithm configurations and future work

In theory, MT-DPIR is applicable to any tracer combination and any numbers of pharmacokinetic models. However, as more models are included, the number of fitting parameters increases also in the reduced parameter space, resulting in again a complicated fitting environment. Although the proposed method may still perform better than the traditional model, the results may not be stable for proper interpretation. In some clinical applications, the administration of 2 tracers can already improve the diagnosis or therapy planning significantly [80, 83]. Thus it is still practical to further test the proposed method for two tracers in clinical studies. In addition, the multi-tracer model is designed to be the superposition of single tracer models [88, 93]. However, the general strategy of using DPIR combined with the RPS reformulation can be extended to models that are not limited to such a structure.

The performance of the recovery of an individual tracer from mixed measurements may also be affected by the time interval between injections as well as the order of tracer injections. For the traditional method, these effects have been discussed in [88] for the combination of [^{18}F]FLT and [^{18}F]FDG. This work aims to propose and preliminarily evaluate the MT-DPIR algorithm for the tracer separations. In the future, the influences of these effects on the performance of MT-DPIR will be carefully studied and optimized before further preclinical and clinical studies.

To conclude, this chapter proposes a direct rapid multi-tracer PET reconstruction algorithm (MT-DPIR) for recovering single tracer information from overlapping acquisitions. In particular, a multi-tracer model with reduced number of parameters is integrated into parametric image reconstruction. The tests on numerical simulation data as well as on preclinical PET measurements have shown that the proposed algorithm can improve the separation of overlapping PET signals. Though it still has a long way to go, we believe the proposed method can promote the development of the multi-tracer towards real medical application.

4

Physiological Evaluation of Direct Parametric Image Reconstruction

DPIR improves parametric images with better visual quality and fewer statistical errors. For clinical applications, it is necessary to determine if these improvements can have practical advantages for physiological estimations. However, it is often challenging to verify physiological quantifications with real measurements due to lack of reference. This chapter presents a preclinical assessment of the quantification ability of DPIR on [^{18}F]FMISO PET to investigate underlying tumor hypoxia status. Hypoxia related PET quantities were acquired from both DPIR and indirect parametric image generation methods using different reconstruction algorithms (FBP & OSEM). In particular, a physiological factor obtained from immunohistochemistry staining is used as reference in this work. PET quantities were compared to the reference to evaluate the influence of reconstruction methods on physiological quantification.

Part of this work has been published in [116].

4.1 Imaging Tumor Hypoxia

Cellular hypoxia is a situation where cells have been deprived of adequate oxygen concentrations. Hypoxia is often seen in a solid tumor which rapidly outgrows its blood supply, leaving tumor cells with significantly lower oxygen levels than healthy tissues. As demonstrated in Fig. 4.1, the oxygen supply is sufficient for cells closest to vasculature, whereas it diminishes further from the blood vessels. As the oxygen supply decreases, cells become hypoxic and later necrotic. Locating hypoxic areas is of great importance. Hypoxic cells are known to be 2 to 3 times more resistant to ionizing radiation than ordinary cells, becoming the major resistance factor for radiotherapy as well as many chemotherapy approaches [117, 118]. For treatment

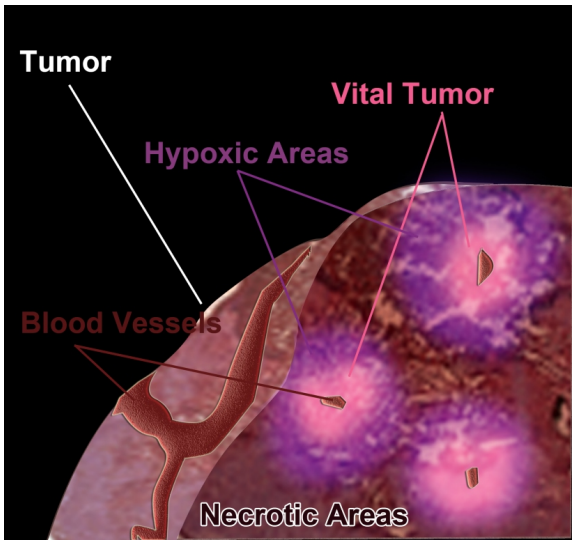

Figure 4.1: A Sketch of the tumor microenvironment

planning of radiation therapy, it is desirable to accurately outline hypoxic regions where higher does can be imposed for effective treatments [119–122].

Microscopically, tumor hypoxia can be detected by immunohistochemistry staining of biopsies or tumor slices *ex vivo* [123]. Hypoxic cells are visualized using exogenous bio-reductive markers such as pimonidazole or EF5. As an example shown in Fig. 4.2a, different antibodies have been applied to the tumor cryosection. Panel a exhibits the H&E staining image which indicates the necrosis and vital tumor areas. Panel b is the fluorescent image demonstrating the distribution of pimonidazole, Hoechst (a perfusion marker), and CD31 (a antibody for staining microvascular endothelium marker).

The detection of hypoxic cells can be achieved non-invasively by PET imaging using hypoxia-specific tracers such as [^{18}F]fluoromisonidazole ([^{18}F]FMISO) [124–129]. PET imaging is recommended as the non-invasive measurement can provide 3D information *in vivo*, conjugated with CT for the application of biologically-guided radiotherapy [130–132]. However, the image quality is limited by the intrinsic low resolution of PET. In general, hypoxic regions are seen surrounding the vessels, gradually increasing from the arterial to the venous end of the microvessels, and are distributed irregularly and discontinuously throughout a tumor. Thus a macroscopic imaging voxel of a tumor usually consists of a mixture of hypoxic and normoxic regions, making the quantification of PET images very difficult. In addition, hypoxia tracers usually have low uptake due to long diffusion distances for hypoxic regions, which are typically not located close to functional blood vessels [133]. Due to the low SNR of measurements, the quantification of hypoxia may become even more challenging and sensitive to errors from reconstruction and model fitting procedures.

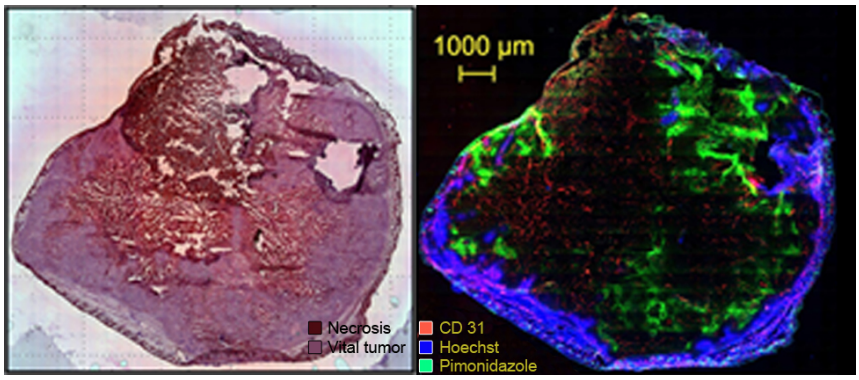

Figure 4.2: (a) An exemplary H&E tumor cryosection staining, illustrating the necrotic and vital tumor areas; (b) the microscopy view of the corresponding stained tumor slice, exhibiting CD 31, Hoechst and Pimonidazole distributions.

A physiological reference is thus desired to assess the image generation procedure and verify the PET quantities for the quantification of tumor hypoxia.

Immunohistochemistry staining provides precise information about the location of hypoxic cells. It has been considered as a physiological reference to assess hypoxia tracer uptake in autoradiography and the results of kinetic modeling in preclinical studies [134, 135]. For instance, hypoxic fraction (HF, for representing the extent of the hypoxia in immunohistochemistry data) has been used to verify the uptake of hypoxia tracers such as [^{18}F]FMISO [135], [^{18}F]FAZA [136] or [^{18}F]HX4 [137] in practice. Here the HF index is employed as a physiological reference to assess the quantification ability of [^{18}F]FMISO PET imaging and to evaluate whether DPIR has advantages for this physiological quantification compared to indirect methods.

4.2 Quantification of Hypoxia

For immunohistochemistry data, hypoxic fraction (HF) is often used to represent the relative severity (extent) of hypoxia [135–137]. It is defined as the area of hypoxic cells divided by the area of vital tumor cells:

$$HF = \frac{Area_{hypoxic}}{Area_{vital}} \tag{4.1}$$

Correspondingly, the necrotic fraction (NF) is specified as the area ratio of the necrotic region over the whole tumor region:

$$NF = \frac{Area_{necrotic}}{Area_{total}} \tag{4.2}$$

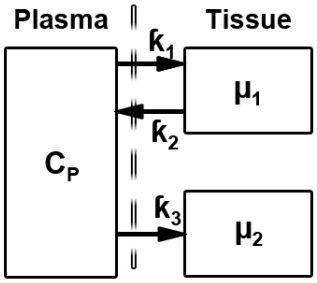

Figure 4.3: A sketch of the decoupled model, which is equivalent to the irreversible two-tissue compartment model (refer to Fig. 1.12a)

For PET measurements, dynamic analysis such as pharmacokinetic modeling is often recommended for the quantification of hypoxia PET imaging and for the extraction of [^{18}F]FMISO binding rates [126, 127, 133, 138, 139]. The irreversible two-tissue compartment model has been reported to have the best physiological correlation with immunohistochemistry staining [139] and oxygen tension (pO_2) measurements [138]. However, the nonlinear model often requires a long time for computation and is sensitive to the noise due to the high dimensional fitting space. The linearized model, such as the Patlak plot [140], is often preferred for voxel-wise computing of parametric images [47, 48, 52] and has been applied to produce the hypoxia-related physiological parameter [127].

4.2.1 The Gjedde-Patlak plot

As shown in Fig. 4.3, to achieve model linearization, a new model that decouples the exponential part and the linear part of Eqn. 1.16 is used. It contains 3 kinetic parameters $\boldsymbol{\kappa}$, which are defined as combinations of parameters $\mathbf{k}$, describing the exchange rates between new compartments μ_1 and μ_2.

$$\begin{cases} \kappa_1 = \frac{K_1 k_2}{k_2 + k_3} \\ \kappa_2 = k_2 + k_3 \\ \kappa_3 = \frac{K_1 k_3}{k_2 + k_3} \end{cases} \tag{4.3}$$

The tissue activity concentration C is calculated as the sum of activity concentration in the decoupled compartments μ_1 and μ_2, which can be simply treated as a reversible one-tissue compartment model and the integral of AIF. The Patlak plot further considers the situation when free tracer components have reached their steady state, so that the ratio $\frac{C}{C_P}$ becomes time independent. Therefore at late time points, the reversible unit μ_1 will also approach its steady state:

$$\mu_1 \rightarrow \frac{\kappa_1}{\kappa_2} C_P \tag{4.4}$$

In the steady state, the ratio $\frac{C}{C_P}$ at image voxel j is expressed as:

$$\begin{gathered} \frac{C_j(t)}{C_P(t)} = Slope_j \frac{\int_0^t C_P(\tau)d\tau}{C_P(t)} + Int_j \\ \begin{cases} Slope_j = \kappa_3 = \frac{K_1 k_3}{k_2+k_3} \\ Int_j = \frac{\kappa_1}{\kappa_2} = \frac{K_1 k_2}{(k_2+k_3)^2} \end{cases} \end{gathered} \tag{4.5}$$

Representing data in this form is called the Patlak plot. The interesting parameter Patlak *Slope* indicates the net transfer rate of the tracer in the steady state. Equality in Eqn. 4.5 is valid only when the steady state has been reached. A status evaluation is necessary before model fitting to achieve reliable results.

4.2.2 DPIR of the Patlak model

Except for the numerical stability and efficiency of calculation, linear models have their advantages for direct parametric image reconstruction. As separate coefficients exist for each linear parameters, a closed-form update function can be deduced for estimating kinetic parameters directly from projection data [47] instead of the 2-step procedure in [49, 57–59]. For instance, in the Patlak case, after multiplying with C_P on both sides of Eqn. 4.5, C can be represented by kinetic parameter weighted temporal basis functions as shown in Eqn. 4.6:

$$\begin{gathered} C_t = p_k b_{kt} = [Slope, Int][b_{1t}, b_{2t}]^T \\ \begin{cases} b_{1t} = \int_0^t C_P(\tau)d\tau \\ b_{2t} = C_{Pt} \end{cases} \end{gathered} \tag{4.6}$$

where $\mathbf{b} \in \mathbb{R}^{N_K \times N_T}$ is a matrix consisting of temporal basis functions corresponding to the parameters $[Slope, Int]$ for each image voxel. C stands for a TAC associated with a voxel. The dynamic PET images $\hat{\mathbf{X}}$ contain N_j TACs and it can be expressed as $\hat{\mathbf{X}} = \mathbf{PB} = \{p_{jk} b_{jkt}\}$. Recalling that to optimize Eqn. 1.18, $\frac{\partial \hat{x}}{\partial \mathbf{p}}$ is calculated. For linear models, since $\mathbf{B}$ is not a function of $\mathbf{P}$, there is:

$$\begin{cases} \frac{\partial \hat{x}_j}{\partial Slope_j} = b_{1jt} \\ \frac{\partial \hat{x}_j}{\partial Int_j} = b_{2jt} \end{cases} \tag{4.7}$$

Then a closed-form update function can be deduced from Eqn. 1.18 for estimating $\mathbf{P}$ directly from the projection data [47, 48], which is written as:

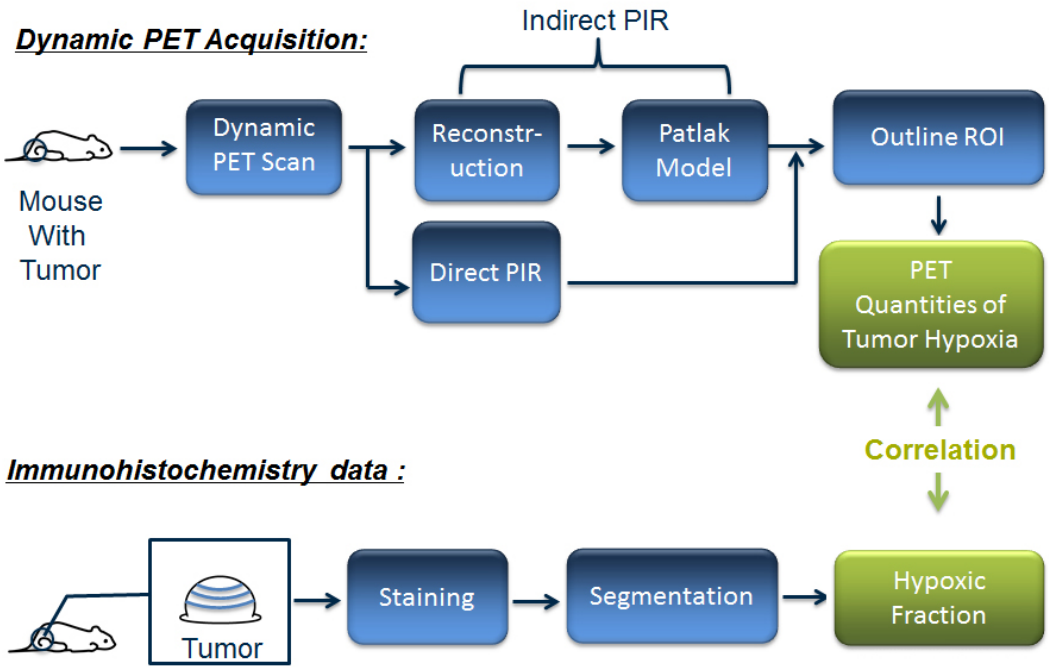

Figure 4.4: A sketch of the evaluation procedure

$$p_{jk}^{(n+1)} = p_{jk}^{(n)} \frac{1}{\sum_{t,i\in I_S} a_{ijt}/\alpha_i b_{kt}} \sum_{t,i\in I_S} \frac{a_{ijt}}{\alpha_i} \left(\frac{\alpha_i p_{jt}}{\sum_{j',k} a_{ij't} p_{j',k}^{(n)} b_{kt}/\alpha_i + r_i + s_i} b_{kt}\right) \tag{4.8}$$

4.3 Material and Methods

The preclinical evaluation procedure is presented in Fig. 4.4. In general, mice with grown tumor were scanned by PET dynamically. The Patlak *Slope* images were reconstructed by direct or indirect parametric image generation methods. For immunohistochemistry study, mice were executed and tumors were cut, sliced and stained for measuring the hypoxia fraction (HF). The *Slope* parameters were compared to HF and the Pearson correlation coefficient was computed to assess parametric image generation methods. Detailed description of each step is given below.

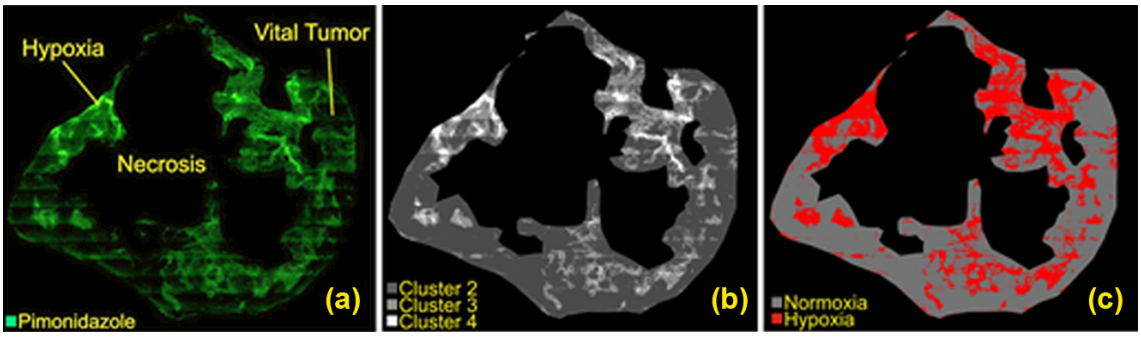

Figure 4.5: The segmentation result of the pimonidazole signal using the K-Mean clustering algorithm: (a) Pimonidazole image (b) 4 clusters (cluster 1 indicates the background) (c) cluster 2 is considered as part of vital tumor while cluster 3+4 is the hypoxic areas

4.3.1 Animal preparation

Human head and neck cancer cell lines FaDu and CAL33 (DSMZ, Braunschweig, Germany) were established for generating xenografted tumors. 2-3 days before tumor transplantation, 7-week old female NMRI nu/nu mice (n=16, Charles River Laboratories, Sulzfeld, Germany) were whole-body irradiated with 4 Gy (RS225A, Gulmay Medical Ltd., UK) at a dose rate of 1 Gy/min (200 kV X-rays) for complete immunosuppression. A 1 mm^3 tumor piece was transplanted subcutaneously into the right hind leg of each anesthetized mouse (0.714 μg/g Medetomidin +7.14 μg/g Midazolam +0.07 μg/g Fentanyl, i.v.). Tumors were allowed to grow to 7 - 10 mm in diameter [141]. The animal studies were approved according to international guidelines and German welfare regulations (EU guidelines: 86/609).

4.3.2 Immunofluorescence study

The hypoxia marker pimonidazole (Hypoxyprobe, Burlington, MA, USA) was injected i.p. at $0.1mg/g$ body weight in a volume of 0.1 mL saline directly before injecting [^{18}F]FMISO. After the PET scan, the Hoechst 33342 (Sigma, Deisenhofen, Germany) perfusion marker was injected i.v. at 15 $\mu g/g$ body weight in a volume of 0.1 mL and 1 min. later each animal was sacrificed, immediately followed by tumor excision. Thereafter, the tumors were shock frozen in liquid nitrogen and stored at -80C. Cryosections (10 μm thick) were generated from the apical, central and basal layers [142] of each tumor and stored at -80C. Shortly before staining, cryosections were fixed in cold (4C) acetone, air dried and rehydrated in phosphate buffered saline (PBS). Pimonidazole was stained with a monoclonal FITC-labeled anti-pimonidazole antibody (Hypoxyprobe, Burlington, MA, USA) diluted 1:50 in primary antibody diluent (PAD; Serotec, Oxford, UK) by incubating for 1 h at

37C in the dark. Microvascular endothelium was stained using a purified rat anti-mouse CD31 antibody (MEC 13.3, BD PharMingen, Heidelberg, Germany) diluted 1:100 in PAD. Anti-CD31 was detected using the secondary antibody AlexaFluor 594 (Invitrogen, Eugene, OR, USA) diluted 1:200 in PBS for 1 h at 37C in the dark. The cryosections were then embedded in fluorescent mounting medium (DAKO, Glostrup, Denmark) and stored at 4C [142].

For the Immunohistochemistry stained tumor slices, necrotic tumor regions in the cryosections were outlined manually based on H&E staining and excluded from the analysis and the necrotic fraction was measured. The hypoxia area can be measured by manual outline or using reproducible clustering methods applying on the pimonidazole image. Here pimonidazole signals were segmented using the k-means clustering algorithm (ImageJ 1.43m, NIH, USA) [143] and were characterized as background, moderate hypoxia and severe hypoxia as demonstrated in Fig. 4.5. The hypoxic fraction (HF) of each cryosection was defined as the ratio of the area of moderate and severe hypoxia over the area of the viable tumor.

4.3.3 PET image generation

Mice were anesthetized with isoflurane and imaged using a preclinical PET/CT (Siemens, Inveon micro PET/CT). 10-15 MBq [^{18}F]FMISO was injected intravenously after a CT scan (80 kVp, ¡ 5 mins) and dynamic PET data were acquired for 2 hours. 2 venous blood samples (2-7 μL) were taken directly after scanning, weighed, and the activity concentration of the [^{18}F]FMISO isotope in the blood was measured in a gamma-counter. The AIFs were modeled using three exponential model individually [109]. All measurements were corrected for non-uniform system response, physical decay, dead time and randoms. Attenuation coefficients were generated based on the acquired CT data. For each mouse, dynamic PET acquisitions were rebinned into 2D sinograms using single-slice rebinning (SSRB) with 128 radial bins, 160 views, 159 direct planes and 46 frames of varying durations: 20 $\times$ 1 s, 4 $\times$ 5 s, 2 $\times$ 10 s, 2 $\times$ 30 s, 4 $\times$ 60 s, 2 $\times$ 120 s, 4 $\times$ 300 s, 6 $\times$ 600 s, 2 $\times$ 900 s. Both direct and indirect parametric image generation algorithms were investigated. The derived images were composed of 128$\times$128$\times$159 voxels per frame at a voxel size of 0.78$\times$0.78$\times$0.80 mm^3.

The arterial input function (AIF) used for kinetic modeling was obtained according to the method described by Wong [144]. Concerning the restricted blood volume of mice, AIF for real data was derived based on the left ventricle (LV) data at an early time from pre-reconstructed dynamic FBP images and corrected for delay (1.77 s), dispersion (1.20 s) and partial volume (recovery coefficient = 0.83). Then the data were concatenated with the activity of the corresponding venous blood samples at the end of the scan, and interpolated using a four exponential model [145]. The coefficient of determination (R^2) was calculated to assess the fitting quality of linear regression of the Patlak model.

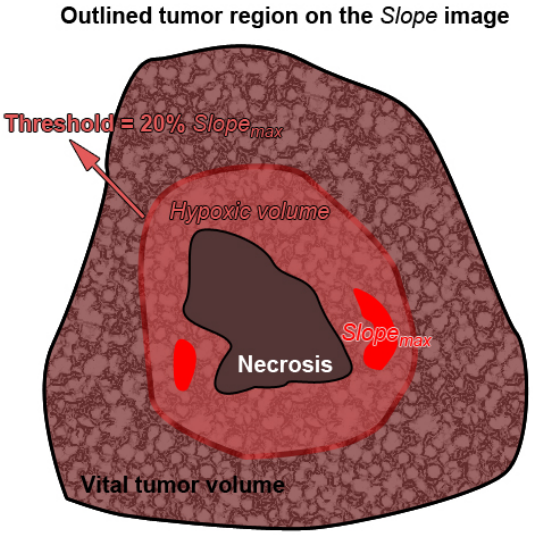

Figure 4.6: A plot demonstrating the segmentation procedure at a threshold of 20% of $Slope_{max}$ for outlining hypoxic and vital tumor volumes on PET images

The parametric *Slope* images generated from FBP+Patlak, OSEM+Patlak and POSEM with different configurations were assessed visually and quantitatively. Tumor volumes were manually outlined and their size was measured based on the fusion of CT and the average of the 46 frames of dynamic PET images using PMOD software (version 3.1; PMOD Technologies, Zurich, Switzerland). Within the whole tumor area, an adaptive threshold was applied to exclude the necrotic regions in the PET data. The threshold was adjusted to ensure that the necrotic fraction from PET was consistent with the NF derived from the microscopic images (Tab. 4.1).

The quantification of PET images was also carried on static reconstructed tracer uptake images (using either analytical or iterative reconstruction). For static analysis, the normalized standard uptake value ($SUV = \frac{Image}{InjectionDose(MBq) \times ObjectWeight(g)}$) is usually measured from reconstructed image at late time points [128]. For comparison to results of pharmacokinetic modeling, SUV was calculated based on the last frame of the dynamic PET scan (2 h p. i., duration 15 min) and the weight and injection dose of the animal as listed in Tab. 4.1.

Furthermore, the mean or maximum voxel value within a region of interest (ROI) of PET images is usually taken as a representative index for a quantity [146–148]. Thus, for the intensity-based comparison, the mean and maximum value of the quantities derived from parametric PET images were employed for the quantification of the hypoxia status. As accurately outlining hypoxic volume on the tumor area based on PET images is challenging, ten different thresholds (10, 20 and 100% of $Slope_{max}$) were tested for segmenting the tumor into hypoxic and vital tumor

volumes as demonstrated in Fig. 4.6. The mean *Slope* parameters in the resulting hypoxic volumes were measured. At last, the mean *Slope*, $Slope_{max}$ as well as SUV_{max} were then compared to HF derived from the immunohistochemistry study, and the Pearson correlation coefficient was computed to assess parametric image generation methods. p-values < 0.05 were considered to be significant.

4.4 Results

4.4.1 Tumor characteristics

The NF and HF of a tumor were assessed as the average of three selected cryosections from the apical, central and basal tumor layers. The characteristics of the investigated mice and tumors are shown in Tab. 4.1, including mice weight (10±2 g), injection dose (23±2 MBq), tumor volume (375±407 mm^3), average vital tumor area (35±20 mm^2), HF (0.27±0.08), and NF (0.36±0.13). Tumors of a large range of volumes (34-1353 mm^3) were generated, resulting in HFs from 0.14 to 0.36.

Table 4.1: General characteristics of the investigated mice

Mouse ID	Tumor line	Mouse weight (g)	Injection dose (MBq)	Tumor size (mm^3)	Average vital tumor area (mm^2)	Necrotic fraction (NF)	Hypoxic fraction (HF)
# 1	FaDu	24	11	495	66	0.326	0.140
# 2	FaDu	28	10	1287	77	0.343	0.274
# 3	CAL-33	25	7	97	23	0.284	0.224
# 4	CAL-33	26	10	359	35	0.171	0.286
# 5	CAL-33	26	9	119	21	0.250	0.195
# 6	CAL-33	23	11	477	23	0.484	0.257
# 7	CAL-33	25	9	61	12	0.613	0.149
# 8	FaDu	21	13	1354	39	0.533	0.381
# 9	FaDu	19	13	444	53	0.447	0.334
# 10	FaDu	25	11	537	46	0.321	0.314
# 11	FaDu	23	8	113	51	0.223	0.287
# 12	FaDu	20	9	151	34	0.380	0.355
# 13	FaDu	22	14	288	32	0.354	0.359
# 14	CAL-33	23	13	101	16	0.231	0.281
# 15	CAL-33	22	13	88	14	0.299	0.239
# 16	CAL-33	22	10	34	9	0.579	0.166

4.4.2 Preparations for PET parametric image reconstruction

To achieve reliable quantification results, tests were done to determine the iterative number for reconstruction and to varify the steady state for Patlak modeling. The evaluation procedures and results are described below.

4.4.2.1 Convergence evaluation for iterative reconstruction methods

The convergence properties of OSEM+Patlak and POSEM were evaluated on two data sets (mice # 2 and # 11). Both methods employed 8 subsets and were initialized with a uniform image for reconstruction. 17 different iteration numbers (from 8 to 392 subiterations per plane) were tested for reconstruction. The averaged *Slope* and Int values within the tumor area were compared with those from FBP+Patlak.

Fig. 4.7 shows the average kinetic parameters *Slope* and Int in whole tumor areas of POSEM and OSEM+Patlak with different numbers of iterations compared to FBP+Patlak for tumors from mice # 2 and # 11. The two kinetic parameters of both methods approach the values obtained from FBP+Patlak as the number of iterations increases. OSEM+Patlak converged faster than POSEM, which is consist with the results in [63, 149]. After 88 iterations, the averaged parameters of OSEM+Patlak were relatively stable ($\leq 0.1\%$) and after 344 iterations, the estimations of POSEM were relatively stable.

As the convergence speed is different, different iteration numbers were set for OSEM+Patlak and POSEM for fair comparisons. In this study, 88 and 344 iterations were chosen for OSEM+Patlak and POSEM respectively to optimize the performance of each method. Though the convergence has not been reached, both methods can provide a relatively stable estimation of kinetic parameters without exaggerating the noise [36]. Increasing the number of iterations decreases the fitting quality of OSEM+Patlak due to excessive noise [149] and may further affect the quantitative performance. To fully explore the influence of over iterated reconstruction on physiological analysis, OSEM+Patlak was additionally computed for 344 iterations and compared with the early-stopped reconstruction.

4.4.2.2 Steady state validation for Patlak modeling

The equilibrium of tracer uptake for the starting point of the Patlak plot in the tumor areas was investigated. As the steady state has been reached, the ratio $\frac{C}{C_P}$ tends to be a constant value and a linear relationship is achieved between C and C_P. Therefore a high fitting quality is expected for Patlak modeling only if the equilibrium has been reached.

The Patlak modle was applied to each TAC starting at 30 min. The coefficient of determination (R^2) was calculated to assess the fitting quality of linear regression.

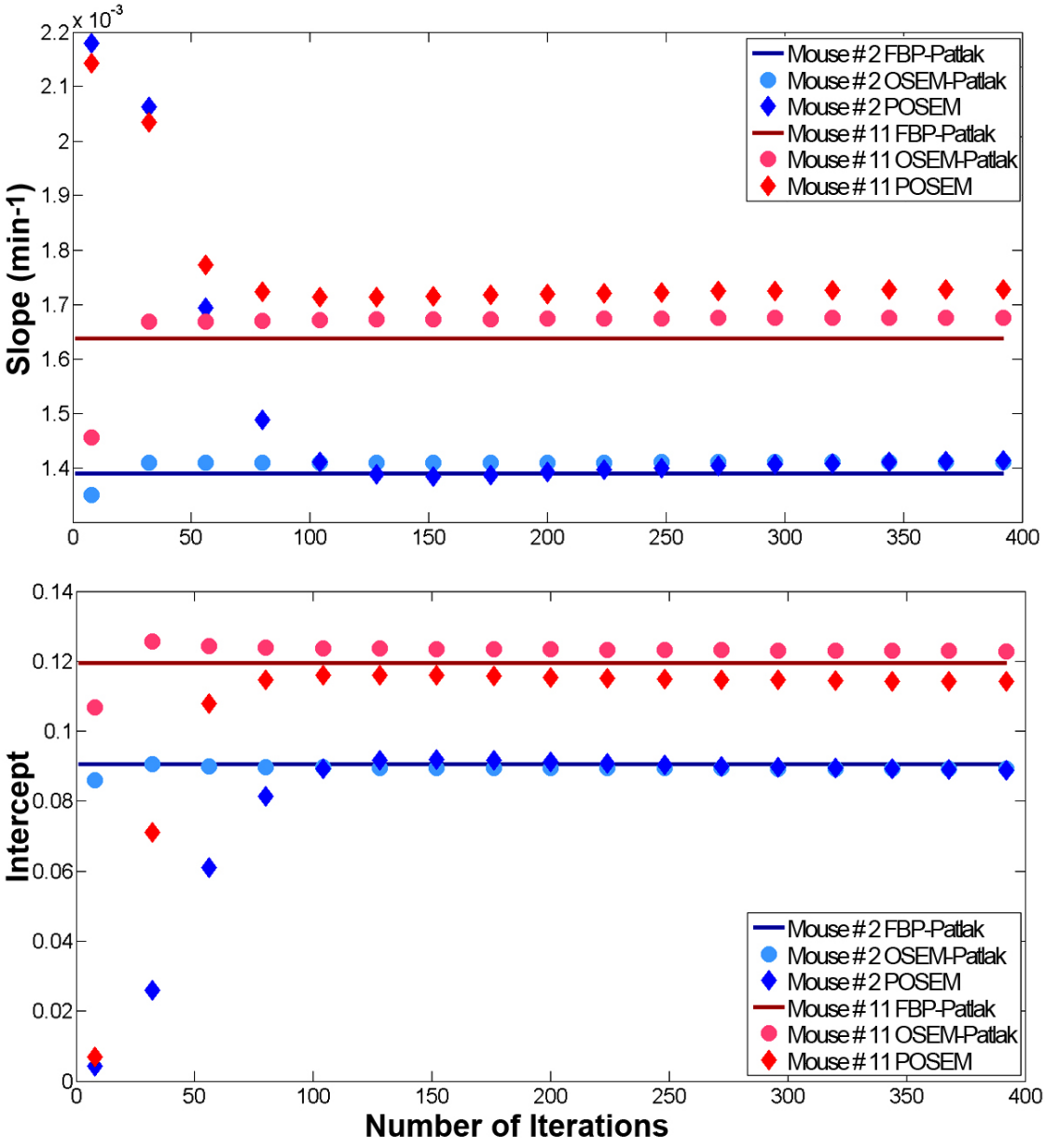

Figure 4.7: Plots of the comparison between the average slope and intercept parameters of the whole tumor of mice # 2 and # 11 using FBP+Patlak, OSEM+Patlak and POSEM

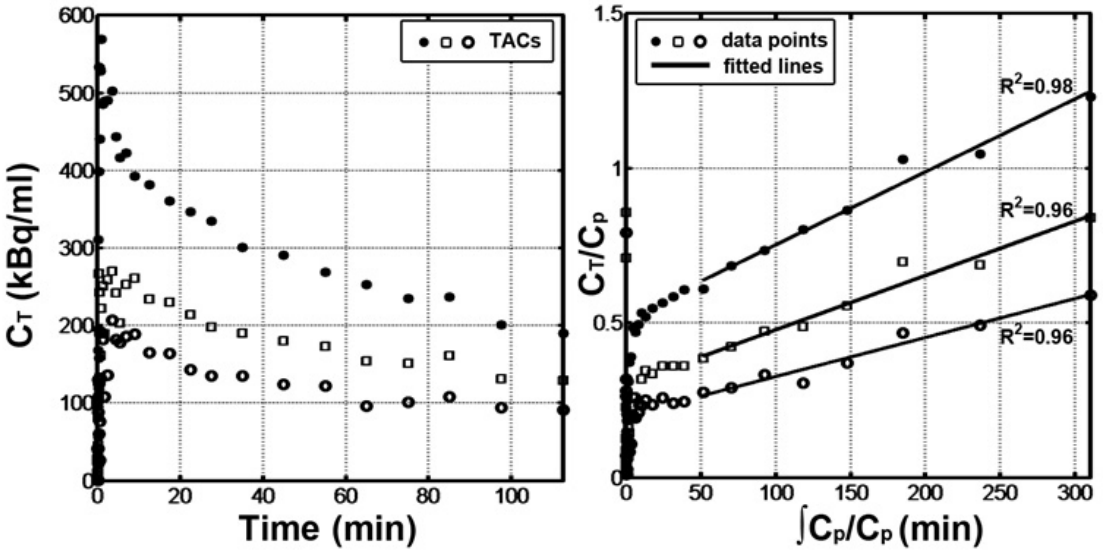

Figure 4.8: Plots of (a) example time-activity curves (TACs) from the tumor area of Mouse # 15; (b) Patlak fitting of corresponding TACs

The results has shown in Fig. 4.8, three example TACs from the tumor area of mouse # 15 and the corresponding fitting results are displayed. The high linearity ($R^2 \geq 0.96$) of the fitted line indicates that equilibrium of [^{18}F]FMISO metabolism was reached in this study.

Overall, based on the evaluation results, direct parametric image reconstruction was implemented by integrating OSEM (8 subsets, 344 subiterations) and Patlak plot as described in Sec. 4.2.2 for all mice data. Indirect parametric image generation was achieved using both FBP (ramp filter, cutoff frequency 0.5 cycles / voxel) and OSEM (8 subsets, 88 and 344 iterations) followed by kinetic fitting using Patlak model for comparison. In all cases, Patlak model was applied on late time frames (30 min p. i.) to ensure the equilibrium status has been reached.

4.4.3 PET quantification analysis

The reconstructed PET parametric images from different reconstruction methods were firstly observed and compared with corresponding tumor cryosections. Fig. 4.9a-d show the result *Slope* image of an example slice from mouse # 1 using FBP+Patlak, OSEM +Patlak (88 iterations), OSEM+Patlak (344 iterations) and POSEM (344 iterations), respectively. Streak artifacts are visible in the parametric image of FBP+Patlak due to the extreme uptake in the mouse urinary bladder.

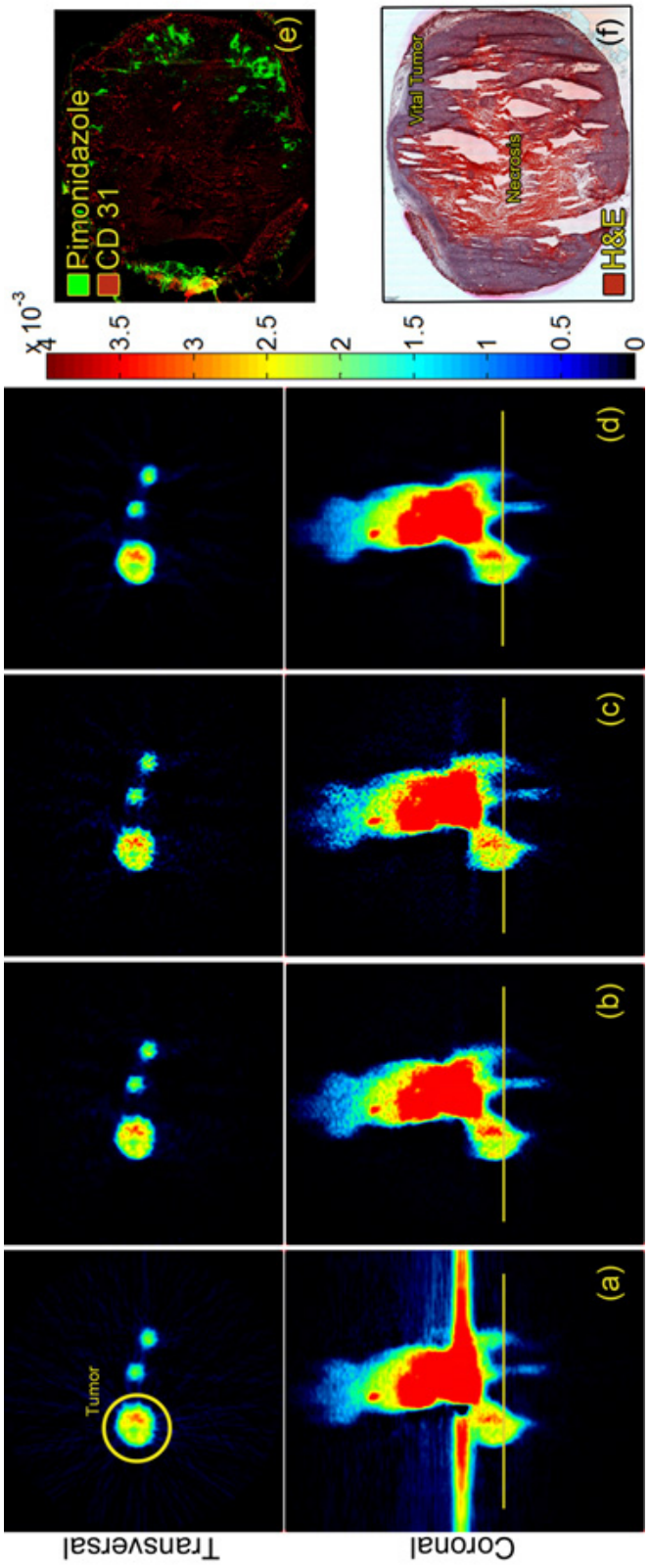

Figure 4.9: The slope parametric images of Mouse # 1 using (a) FBP+Patlak; (b) OSEM + Patlak (88 iterations); (c) OSEM + Patlak (344 iterations) and (d) POSEM (344 iterations); (e) the corresponding pimonidazole staining of the tumor and (f) H&E staining of the slice in (e)

Noise was observed in both parametric images of OSEM+Patlak. The noise increased as the number of iterations increased. The *Slope* image generated from POSEM is generally smoother than the others. It exhibits less streak artifacts and image noise, especially in the low signal areas. A necrotic core is clearly visible in the POSEM *Slope* images, which is confirmed by the large region seen in the pimonidazole and H&E staining of a cryosection from the center of the tumor (Panels d and e).

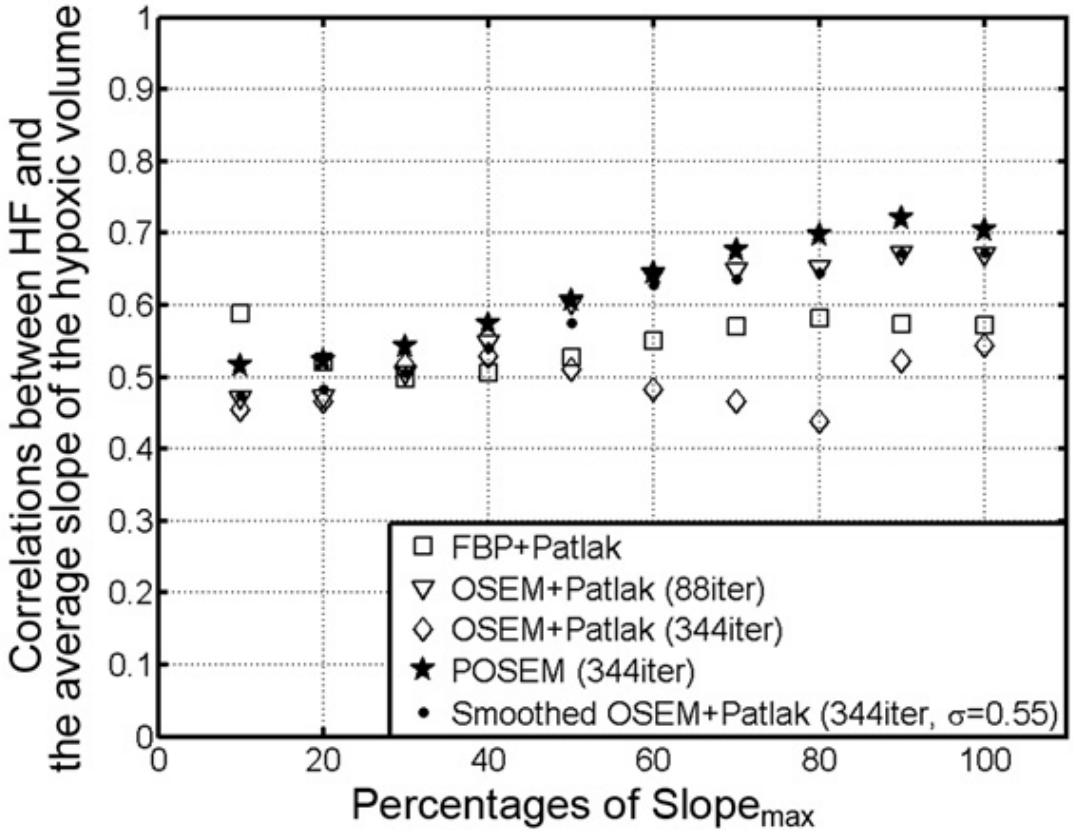

Figure 4.10: A plot of the correlations between the hypoxic fraction (HF) and the mean slope parameter of tumor hypoxia volumes delineated using different percentages of $Slope_{max}$ on slope parametric images obtained from FBP+Patlak, OSEM+Patlak (88 & 344 iterations) and POSEM (344 iterations); Real dots showing results acquired from smoothed slope parametric images of OSEM+Patlak with a Gaussian kernel of standard deviation $\sigma = 0.55$

Given the reconstructed parametric images of all mice, the correlation was evaluated between HF derived from pimonidazole staining and the average *Slope* of the hypoxic volume for each threshold level is shown in Fig. 4.10. In general,

Table 4.2: Correlations between HF and SUV_{max} or Patlak $Slope_{max}$ using FBP, OSEM (88 and 344 iterations) and POSEM (344 iterations).

		HF and SUV_{max}		HF and $Slope_{max}$ (Patlak)	
	Iteration No.	r	p	r	p
FBP	—	0.50	0.0483	0.57	0.0206
OSEM	88	0.20	0.4660	0.67	0.0045
	344	0.18	0.5030	0.54	0.0294
POSEM	344	—	—	0.70	0.0023

the average *Slope* from most investigated methods has a correlation coefficient of over 0.5 and the correlation became continually stronger as the threshold increased. The coefficients obtained from OSEM+Patlak at 344 iterations are lower at most threshold levels compared to the results at 88 iterations. The parametric images from POSEM provided the highest correlation with HF at most cut-off values. For thresholds above 50% of $Slope_{max}$, the resulting correlation coefficients were higher than 0.6.

Further more, the correlations was investigated between the maximum value of PET quantities (SUV_{max} and $Slope_{max}$) and HF as shown in Tab. 4.2 as well as in Fig. 4.11. HF and SUV_{max} were significantly correlated when FBP was used. In contrast, significant correlations were observed for $Slope_{max}$ for all of the four investigated parametric image generation methods. The $Slope_{max}$ of POSEM correlated the best with HF. Although significant correlations (Tab. 4.2) between the $Slope_{max}$ of OSEM+Patlak and HF were observed, the correlations were sensitive to the number of iterations. A relatively low correlation was obtained between the $Slope_{max}$ of FBP+Patlak and HF.

4.5 Discussion

Direct parametric image reconstruction has been reported to have improved statistical quality [48] and this work aimed to clarify whether or not this improvement can bring additional value to physiological estimations. The direct parametric image reconstruction algorithm, POSEM, was assessed for the quantitative estimation of tumor hypoxia from dynamic [^{18}F]FMISO PET. Using the hypoxic fraction (HF) from immunohistochemistry data as a physiological reference, the comparison with indirect parametric image generation methods including FBP+Patlak and OSEM+Patlaks as well as with typical SUV_{max} on static images confirmed that the direct parametric imaging reconstruction can improve the physiological quantification of tumor hypoxia based on [^{18}F]FMISO PET.

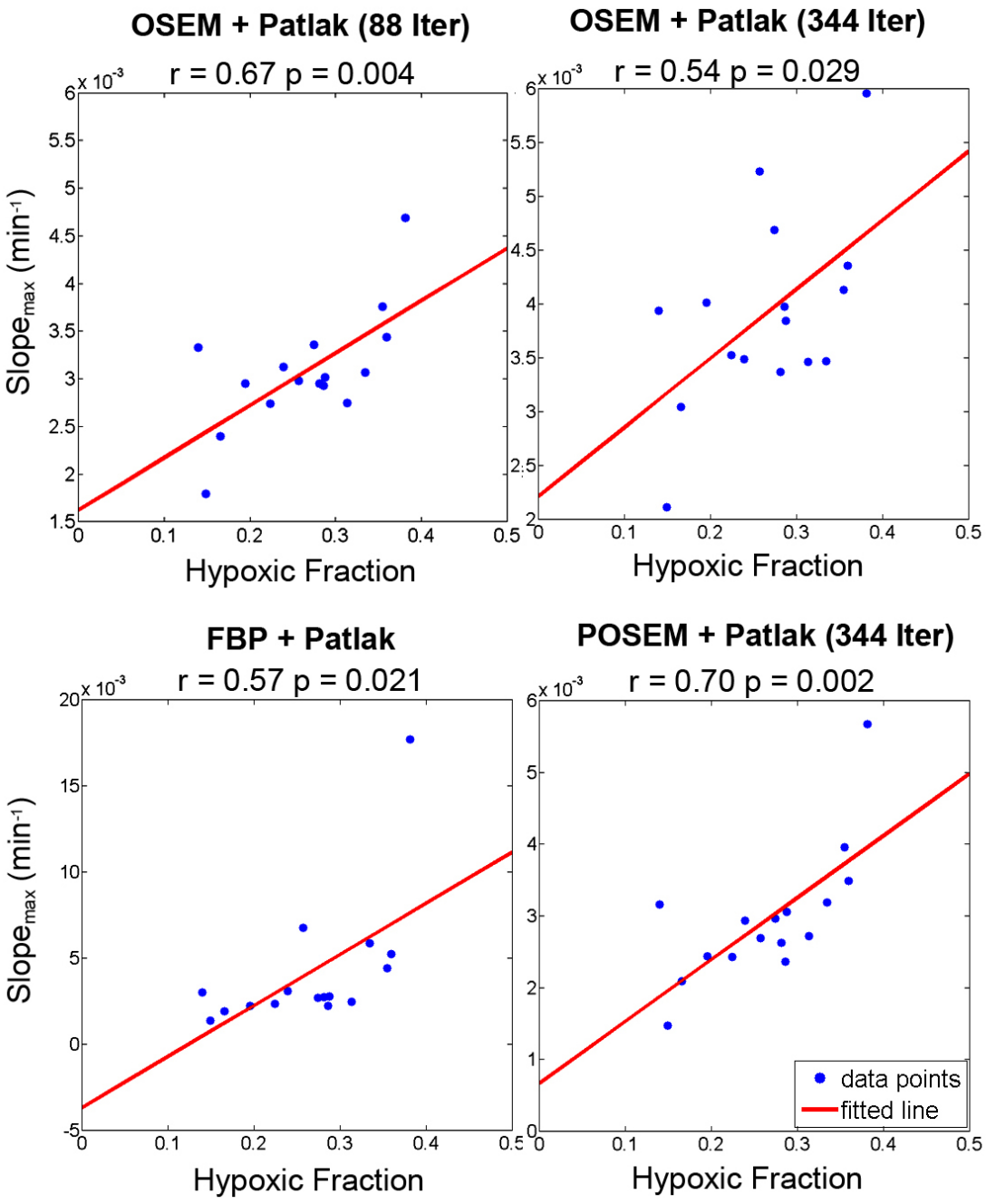

Figure 4.11: Scatter plots of the correlation between the hypoxic fraction and $Slope_{max}$ obtained from FBP+Patlak, OSEM+Patlak (88 iterations), OSEM+Patlak (344 iterations) and POSEM (344 iterations)

4.5.1 Hypoxic quantities

As introduced in Sec. 4.1, quantifying hypoxia from PET images is challenging due to the heterogenous tumor microenvironment and the limited PET spatial resolution. Thus we used this microscopic measure (the hypoxic fraction) of tumor hypoxia as a physiological reference for the quantification of [^{18}F]FMISO PET images.

The Patlak plot was chosen to characterize the underlying kinetics of [^{18}F]FMISO tracer in this study. The linear parameter Slope integrates the tracer kinetic parameters of the irreversible two tissue compartment model, which may reduce physiological interpretation. A stronger correlation may be expected using nonlinear models [126, 133]. However, it may suffer from numerical instability such as local minima due to nonlinear regression. Also, less computational time is required for linear model fitting than nonlinear regression.

To evaluate if direct parametric image reconstruction can bring additional physiological value, we investigated the *Slope* parameter from Patlak plot for quantifying hypoxia from PET. By setting the threshold at increasing percentages of $Slope_{max}$, better correlations between HF and the average *Slope* of the hypoxic volume were observed. Since r coefficients are higher at higher cut-off values (percentages of $Slope_{max}$), which generates higher signal intensity (larger mean *Slope* values), our assumption is supported that the Patlak *Slope* reflects the severity of hypoxia.

4.5.2 Errors from reconstruction

For indirect method, two main reasons that degrade the image quality. Firstly, indirect parametric generation methods estimate kinetic parameters from reconstructed data, which may suffer from streak artifacts in analytical methods or high noise as the iteration number increases for iterative methods. Voxel-wise kinetic modeling may propagate the errors from reconstruction to the resulting parametric images. The uptake of [^{18}F]FMISO in a hypoxic region is usually very low due to the larger diffusion distance of the hypoxia tracer. Therefore, these errors affect the resulting parametric images more seriously. This can be confirmed in Fig. 4.12, where the streak artifacts in FBP+Patlak and the noise in OSEM+Patlak reduce the fitting quality of the pharmacokinetic model, leading to unclear parametric images. Consequently, this limited statistical behavior influences the accuracy of the estimation of the underlying physiology, where the values of PET quantities (e.g., $Slope_{max}$) are sensitive to the errors of reconstruction. This was confirmed by the lower correlation with HF for the indirect parametric image generation methods than the direct parametric image reconstruction. Secondly, the fitting quality may be affected by the lower SNR or errors from reconstruction also, which consequently results in a inaccurate estimations of kinetic parameters. To explore the influence of noise/errors on the fitting quality, we calculated the R^2 maps of FBP+Patlak and OSEM+Patlak and displayed in Fig. 4.12. Panel a shows R^2 based on FBP+Patlak

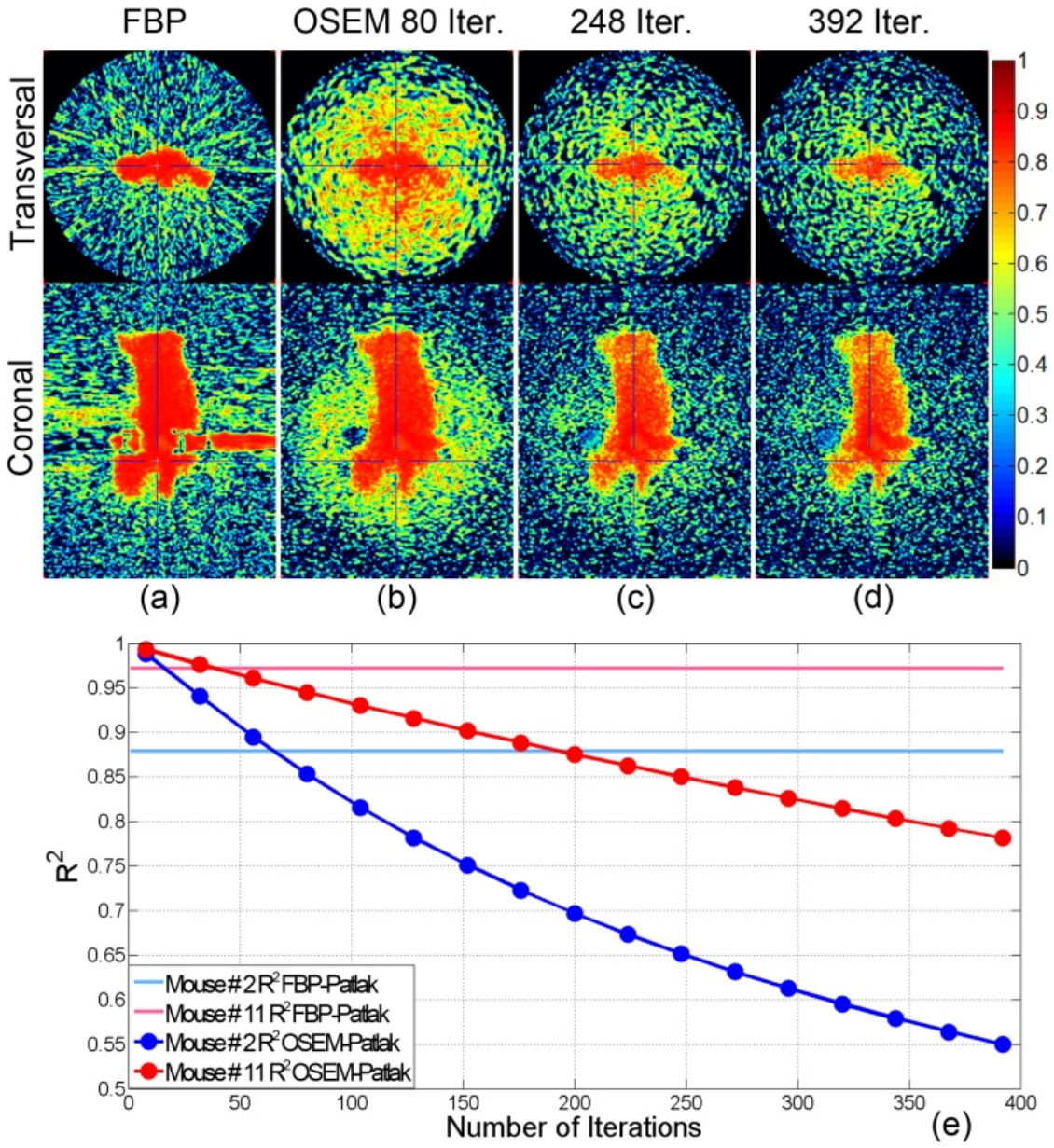

Figure 4.12: R^2 images generated from (a) FBP+Patlak; (b) OSEM+Patlak with 80 iterations; (c) OSEM+Patlak with 248 iterations; (d) OSEM+Patlak with 392 iterations; (e) plots of the average tumor R^2 values of OSEM+Patlak with different number of iterations compared to FBP+Patlak (Iter. = Iterations)

images from mouse # 11. Panels b to d are the corresponding R^2 images obtained from OSEM+Patlak using 80, 248 and 392 iterations, respectively. Panel e plots the mean R^2 values in the tumor area. The fitting quality became worse as noise increased due to the increasing number of iteration used for OSEM reconstruction.

In contrast, DPIR integrates the linear Patlak plot into the optimization function for estimating model parameters directly from projection data. As the spatial and temporal measurements are used simultaneously, improved SNR is achieved for either reconstruction or kinetic modeling, as compared to the separated 2-steps indirect methods. Thus improved statistical quality and higher contrast of images from DPIR has been observed, consisting with the results in [48]. As DPIR is less affected by the reconstruction errors and the improved SNR may potential improve the fitting quality and more accurate estimation of *Slope*, the correlation between the *Slope* of POSEM and HF and consequently the estimation of the underlying hypoxic status was enhanced.

4.5.3 Influence of iteration number

It is difficult to decide on the iteration number for an iterative reconstruction method. Generally, higher numbers of iterations results in images with a better resolution and lower bias. However, the variance of reconstructed images becomes amplified as the iterations continue. A decrease of the correlation between average *Slope* and HF using OSEM+Patlak (on average: -19.8%) was observed as the number of iterations increased from 88 to 344 for most cases in this study. Thus, the number of iterations for the iterative reconstruction methods including OSEM and POSEM need to be selected carefully. In this study, the early-stopping strategy [36] was considered to compromise between bias and noise.

Different convergence speeds were also observed between OSEM and POSEM [63, 149]. Thus, different numbers of iterations were chosen for OSEM+Patlak and POSEM for fair comparisons and comparable results were generated. The correlation between HF and $Slope_{max}$ for the OSEM+Patlak at 88 iterations was $r = 0.67, p = 0.0045$ and the result of POSEM at 344 iterations was $r = 0.70, p = 0.0023$.

If a high number of iterations is used, smoothing OSEM reconstructed images before Patlak modeling can help suppress the noise in resulting parametric images and make the image resolution consistent with other reconstruction methods [48]. As a test, 3D Gaussian kernels ($3 \times 3 \times 3$ voxels) with different standard deviations ($\sigma = 0.35, 0.55$ or 0.75) were investigated. As shown in Fig. 4.10, at a standard deviation of $\sigma = 0.55$, the highest correlation between HF and $Slope_{max}$ was observed for the smoothed OSEM+Patlak (344 iterations) ($r = 0.67, p = 0.0043$), which was similar to the result from OSEM at 88 iterations (mean difference: 0.88%). On average, 19.1% improvement in correlation between HF and the average *Slope* of hypoxic volume for all threshold levels was achieved. The correlation curve with respect to different thresholds of the smoothed OSEM-Patlak had a similar shape

as the other methods.

The tradeoff between bias and noise may also be improved by applying regularization. It is possible to suppress the noise in iterative reconstruction with properly chosen regularizers based on prior knowledge of the smoothness of the parameter image [52,150]. For example, using a maximum a posteriori (MAP) method incorporated with roughness penalty terms can directly encourage image smoothness. Both direct and indirect methods would benefit from MAP to regularize noise meanwhile preserving desired image properties (e.g., retain edges) [151]. It is not expected to change the relative performance for investigated methods [52].

4.5.4 ROI or voxel-wise analysis

The mean *Slope* values over a large region (e.g., whole vital tumor) of parametric images obtained from different methods were similar in our study. This is consistent with previous results [48, 62]. However, the values of individual voxels from the parametric images vary for each investigated method. As shown in Fig. 4.13, we compared the intensities of vital tumor voxels obtained from different reconstructions, and the largest deviation ($r = 0.76, p = 2.85e^{-6}$) was observed from mouse # 7 between different methods.

On the other hand, voxel-wise analysis may have its advantages for hypoxia studies. Hypoxic regions, either acute or chronic hypoxia, are associated with a defined area encompassing individual vessels [152]. In this way, they usually spread discontinuously across the tumor and are highly heterogeneous. In a previous study, Shi et al. undertook a modeling study using average TACs from whole vital tumor regions and no significant correlation ($r = 0.30, p = 0.26$) was reported between the Patlak *Slope* and HF for this region-wise analysis [139]. In this study, the $Slope_{max}$ of Patlak plots was found to be more representative of the severity of hypoxia. It correlated better than the region-wise analysis of the whole vital tumor. Additionally, it was observed in this study that the correlation decreased as more TAC-associated tumor voxels were included (Fig. 4.13). Although the Patlak plot may lose some physiological accuracy, it can capture the intra-tumor heterogeneity of tumor hypoxia.

Nevertheless, voxel-wise analysis suffers from low signal level and is thus more sensitive to selected parametric image generation methods. Due to reduced errors from reconstruction, the $Slope_{max}$ from direct parametric image reconstruction provided better physiological estimation than from indirect methods, thereby confirming our hypothesis.

4.5.5 Delineation of the hypoxic volume

Delineation of the hypoxic volume from PET imaging currently serves as the basis for biologically-guided radiotherapy [132]. To further compare the accuracy of indirect

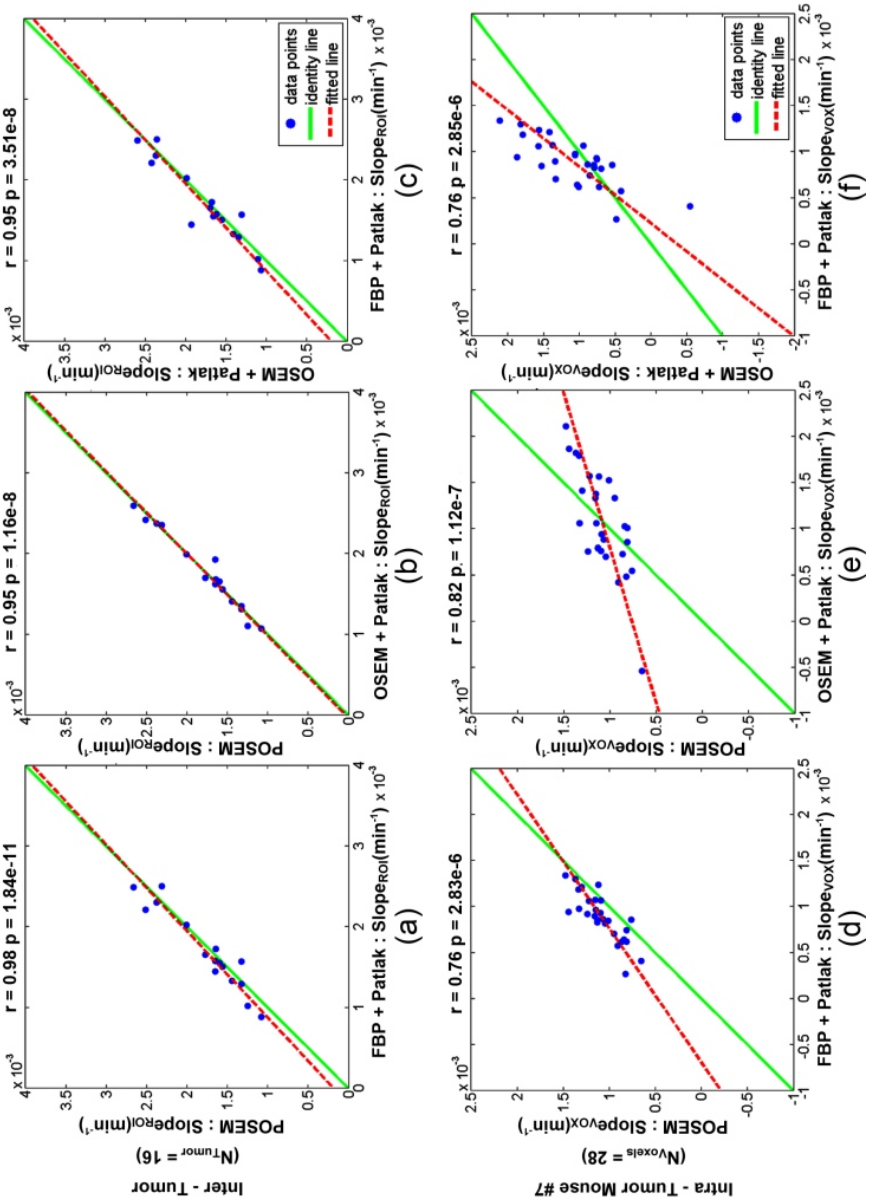

Figure 4.13: Scatter plots showing the correlation of the slope parameters between the three investigated methods: FBP+Patlak, OSEM+Patlak (344 iterations) and POSEM (344 iterations); the upper panel comparing the average slope parameters of vital tumor areas of all 16 mice; the bottom panel comparing the slope parameter of each voxel in the vital tumor area of mouse # 7

and direct methods for the delineation the hypoxic volume, parametric images using different thresholds were investigated and verified using immunohistochemistry data.

In general, direct methods have better correlations with HF than indirect methods. The results from POSEM (344 iterations) showed that a threshold value larger than 50% of $Slope_{max}$ generated hypoxic volumes whose mean Slope correlated better ($r > 0.6$) with the underlying HF. Considering the improved quantification by direct parametric image reconstruction and the high correlation obtained, a strategy for delineation of the hypoxic volume at 50% of $Slope_{max}$ of the parametric image from POSEM is recommended for further investigation in biologically-guided radiotherapy. The delineation of the hypoxic volume is a therapy related concept where voxels with higher hypoxic fractions were outlined. A proper hypoxic volume delineation needs to consider the relevant therapy effect, such as tumor control probability under radiotherapy. Nevertheless, this method has proposed a strategy to delineate the hypoxic volume with high correlation to the underlying severity of hypoxia.

Furthermore, we compared the hypoxic volume using the proposed strategy from PET images with the hypoxic volume derived from immunohistochemistry [153]. A significant correlation ($r = 0.76, p = 0.0006$) was observed. This supports our suggestion of delineating tumor hypoxia based on parametric images.

The convergence speed of POSEM can be potentially improved by using nested algorithms [53], but it is not expected to influence the quantitative performance of the direct method. This study is also limited by the comparison of the methods within a 2D reconstruction framework. The results demonstrate that the physiological interpretation benefits from the improvement of SNR. The incorporation of a 3D system matrix in the reconstruction could further improve the SNR of each investigated method [154,155]. But it is not expected to change the relative behaviors towards quantitation of the investigated methods.

To sum up, this chapter evaluates the direct parametric image reconstruction method for estimating tumor hypoxia from dynamic [^{18}F]FMISO PET, using the *ex vivo* hypoxic fraction (HF) as a physiological reference. The results of direct POSEM are compared with indirect parametric image generation methods, including FBP+Patlak and OSEM+Patlak. This assessment has demonstrated that direct parametric image reconstruction provides better image quality and better physiological estimation. Thus, POSEM is recommended for the analysis of tumor hypoxia, and a strategy of delineation of the hypoxic volume by thresholding at half of $Slope_{max}$ is proposed for further investigation. In the future, advanced registration strategies between macroscopic (e.g., PET) and microscopic (e.g., tissue staining) will be tested for further quantitative evaluation of the parametric image generation methods.

5

Conclusion

This thesis proposes mathematical algorithms to improve dynamic PET image reconstruction so as to achieve better physiological quantification for clinical diagnosis. In particular, these algorithms utilize temporal coherence and tracer pharmacokinetics to reduce reconstruction artifacts and enhance image quality. The value of the physiological quantification resulting from these improvements in reconstruction was also assessed.

Though FBP is still favored for PET imaging due to its robust performance for physiological quantification, the practical applications of this analytical method may be hampered by intrinsic streak artifacts arising from reconstruction. To overcome this obstacle, this thesis proposes a framework which utilizes the temporal coherence of dynamic PET measurements for data decomposition in the projection space. This decomposition enables separated sinograms to be processed respectively, and this consequently reduces severe streak artifacts before final image generation. This framework was evaluated using both realistic simulations and physical phantom measurements. Corrected images demonstrate a clear reduction in streak artifacts for all experiments. Furthermore, quantification results confirm that the new method produces dynamic PET images and kinetic parametric images with higher quantitative accuracy. The proposed algorithm may be limited to tomographic imaging of dynamic protocols. However, with the development of dynamic measurements such as dynamic contrast-enhanced (DCE) CT imaging, the new method may be extended to other tomographic applications.

PET imaging of multiple tracers in separated scans has exhibited its advantages in enhancing the sensitivity and specificity of tumor diagnosis in clinical studies. A simultaneous measure of overlapping tracers may further improve the diagnosis value, but only if individual components can be reliably recovered from the physically non-differentiable PET acquisitions. This thesis proposes an algorithm to improve tracer separation by investigating pharmacokinetics within the reconstruction procedure. Particularly, the algorithm integrates a multi-tracer kinetic model into iterative optimization to achieve mutual regularization and improvements in

the reconstruction of spatial and temporal components. In addition, considering the high dimensional parameter space, the multi-tracer model has been reformulated to reduce fitting dimensionality. The proposed algorithm was systematically analyzed using numerical simulations. Evaluation results of recovered single tracer images and parametric images indicate that the new method can improve the accuracy and the stability of tracer separation with less quantitative error. Validation results of preclinical PET data show that the separated tracer components are closer to physiological expectations. For practical applications, this method requires further validation with clinical data and still faces challenges from blood input functions, mutual tracer reactions, organism motions, and other practical issues. Though it still has a long way to go, we believe the proposed method can promote the development of the multi-tracer towards real medical application.

The development of direct parametric image reconstruction (DPIR) has drawn more and more attention to dynamic PET reconstruction. As the algorithm achieves spatial-temporal optimization simultaneously, the signal-to-noise ratio of PET measurements used for reconstruction is enhanced compared to the frame-by-frame reconstruction, resulting in improved kinetic parameter estimation. To evaluate if these improvements can benefit the physiological estimation of actual diagnosis, this thesis compares parametric images of preclinical PET data generated with or without DPIR. Specifically, the corresponding immunochemistry tumor staining was used as a biological reference for quantitative evaluation. Physiologically related PET quantities were acquired from parametric images. Evaluation results indicate that physiological quantities acquired from DPIR reconstruction exhibit higher correlation with the reference, confirming a more accurate physiological estimation achieved due to improvements in reconstruction. In the future, further validations of different tracers and model applied to a variety of patient data would be required for the development of DPIR towards clinical practice.

A

List of publications

A.1 Peer-Reviewed publications

- **Xiaoyin Cheng**, Nassir Navab, Sibylle I Ziegler and Kuangyu Shi, Direct parametric image reconstruction of rapid multi-tracer PET, *Medical Image Computing and Computer-Assisted Intervention MICCAI 2013*, vol. 8151, pp 155-62, 2013.

- **Xiaoyin Cheng**, Christine Bayer, Constantin-Alin Maftei, Sabrina T Astner, Peter Vaupel, Sibylle I Ziegler and Kuangyu Shi, Preclinical evaluation of parametric image reconstruction of [18F]FMISO PET: correlation with ex vivo immunohistochemistry, *Physics in Medicine and Biology*, 59(2):347, 2014.

- **Xiaoyin Cheng**, Zhoulei Li, Zhen Liu, Nassir Navab, Sung-Cheng Huang, Ulrich Keller, Sibylle I Ziegler and Kuangyu Shi, Direct Parametric Image Reconstruction in Reduced Parameter Space for Rapid Multi-Tracer PET Imaging, *IEEE Transactions on Medical Imaging*, *under revision.*

- **Xiaoyin Cheng**, Jun Liu, Jakob Vogel, Zhen Liu, Nassir Navab, Sibylle I Ziegler and Kuangyu Shi, Time-Activity Curve based Sinogram Decomposition for Streak Artifacts Reduction in Dynamic PET Reconstruction, *Computational Methods for Molecular Imaging (CMMI) Workshop - MICCAI 2014*, *in press.*

A.2 Patent applications

- **Xiaoyin Cheng**, Sibylle I. Ziegler and Kuangyu Shi, Reduction of Streak Artifacts in FBP Reconstruction based on Decomposition in Projection Space, 2012, patent pending, application ID: 201210439390.3

- Kuangyu Shi, **Xiaoyin Cheng** and Sibylle I.Ziegler, Transmission Scan in PET/MRI for Radiotherapy Treatment Planning, 2012, patent ID: XI64/2012-09.

A.3 Conference contributions

- **Xiaoyin Cheng**, Nassir Navab, Sibylle I. Ziegler and Kuangyu Shi, "Direct parametric image reconstruction and separation of simulated rapid [18F]FDG and [11C]MET PET data in a reduced parameter space", *Society of Nuclear Medicine and Molecular Imaging (SNMMI 2014)*, Jun 8-12, 2014, St. Louis, US

- **Xiaoyin Cheng**, Chuantao Zuo, Huiwei Zhang, Yi-hui Guan, Stefan Frster, Sibylle I. Ziegler and Kuangyu Shi, "Parametric images using reduced parameter space method on dynamic [11C]MET PET", *Society of Nuclear Medicine and Molecular Imaging (SNMMI 2013)*, Jun 8-12, 2013, Vancouver, Canada

- **Xiaoyin Cheng**, Jun Liu, Jakob Vogel, Zhen Liu, Nassir Navab, Sibylle Ziegler and Kuangyu Shi, "Time-Activity Curve Based Sinogram Decomposition for Streak Artifacts Reduction in Dynamic PET Reconstruction", *Institute of Electrical and Electronics Engineers Medical Imaging Conference (IEEE 2012)*, Oct 27-Nov 3, 2012, Anaheim, US

- Kuangyu Shi, **Xiaoyin Cheng**, Nassir Navab and Sibylle I. Ziegler, "Sparse Reconstruction of Transmission Scan in PET/MRI", *Institute of Electrical and Electronics Engineers Medical Imaging Conference (IEEE 2012)*, Oct 27-Nov 3, 2012, Anaheim, US

- **Xiaoyin Cheng**, Constantin-Alin Maftei, Christine Bayer, Sabrina T. Astner, Sibylle I. Ziegler and Kuangyu Shi, "Assessment of parametric image reconstruction for the application of preclinical hypoxia imaging", *Society of Nuclear Medicine and Molecular Imaging (SNM 2012)*, Jun 8-12, 2012, Miami Beach, US

- **Xiaoyin Cheng**, Kuangyu Shi, Rebekka Kraus, Gaspar Delso and Sibylle I. Ziegler, "Feasibility study of factor analysis and kinetic modeling for spatial discrimination of rapid dual-tracer PET", *Society of Nuclear Medicine and Molecular Imaging (SNM 2011)*, Jun 8-12, 2011, San Antonio, US

- **Xiaoyin Cheng**, Gaspar Delso, Rebekka Kraus and Sibylle I. Ziegle, "Monte-Carlo based system matrix generation for the Biograph mMR", *Society of Nuclear Medicine and Molecular Imaging (SNM 2011)*, Jun 8-12, 2011, San Antonio, US

Bibliography

[1] M. E. Phelps, E. J. Hoffman, N. A. Mullani, and M. M. Ter-Pogossian, "Application of annihilation coincidence detection to transaxial reconstruction tomography," *J. Nucl. Med.*, vol. 16, pp. 210–24, 1975.

[2] S. Cherry and M. Dahlbom, "PET: Physics, instrumentation, and scanners." Springer New York, 2006, pp. 1–117.

[3] D. Bailey, D. Townsend, P. Valk, and M. Maisey, *Positron emission tomography: basic sciences.* Springer-Verlag, 2005.

[4] L. A. Shepp and Y. Vardi, "Maximum likelihood reconstruction for emission tomography," *IEEE Trans. Med. Imag.*, vol. 1, pp. 113–22, 1982.

[5] D. L. Snyder and D. Politte, "Image reconstruction from list-mode data in an emission tomography system having time-of-flight measurements," *IEEE Trans. Nucl. Sci.*, vol. 30, pp. 1843–1849, 1983.

[6] Y. Vardi, L. A. Shepp, and L. Kaufman, "A statistical model for positron emission tomography," *J. Amer. Statist. Assn.*, vol. 80, pp. 8–20, 1985.

[7] S. R. Deans, *The Radon Transform and Some of Its Applications.* John Wiley and Sons, 1983.

[8] T. F. Budinger, "Time-of-flight positron emission tomography: status relative to conventional PET," *J. Nucl. Med.*, vol. 24, pp. 73–8, 1983.

[9] C. Thompson, "The problem of scatter correction in positron volume imaging," *IEEE Trans. Med. Imag.*, vol. 12, pp. 124–32, 1993.

[10] S. Cherry and S. C. Huang, "Effects of scatter on model parameter estimates in 3D PET studies of the human brain," *IEEE Trans. Nucl. Sci.*, vol. 42, pp. 1174–1179, 1995.

[11] E. Vicente, M. Soto-Montenegro, S. Espaa, J. L. Herraiz, E. Herranz, J. J. Vaquero, M. Desco, and J. Udias, "Influence of random, pile-up and scatter corrections in the quantification properties of small-animal PET scanners," in *IEEE Nucl. Sci. Symp. Conf.*, vol. 5, 2007, pp. 3964–8.

[12] S. R. Cherry, S. R. Meikle, and E. J. Hoffman, "Correction and characterization of scattered events in three-dimensional PET using scanners with retractable septa," *J. Nucl. Med.*, vol. 34, pp. 671–8, 1993.

[13] T. Hasegawa, E. Tanaka, T. Yamashita, M. Watanabe, T. Yamaya, and H. Murayama, "A monte carlo simulation study on coarse septa for scatter correction in 3D PET," *IEEE Trans. Nucl. Sci.*, vol. 49, pp. 2133–8, 2002.

[14] J. Ollinger and G. Johns, "Model-based scatter correction for fully 3D PET," in *IEEE Nucl. Sci. Symp. Med. Imag. Conf.*, 1993, pp. 1264–8.

[15] C. Levin, M. Dahlbom, and E. Hoffman, "A monte carlo correction for compton scattering effects in 3D PET brain imaging," in *IEEE Nucl. Sci. Symp. Med. Imag. Conf.*, vol. 4, 1994, pp. 1502–6.

[16] R. D. Badawi, M. P. Miller, D. L. Bailey, and P. K. Marsden, "Randoms variance reduction in 3D PET," *Phys. Med. Biol.*, vol. 44, pp. 941–54, 1999.

[17] C. Thompson, N. Ranger, and A. Evans, "Simultaneous transmission and emission scans in positron emission tomography," *IEEE Trans. Nucl. Sci.*, vol. 36, pp. 1011–6, 1989.

[18] C. Thompson, N. Ranger, A. Evans, and A. Gjedde, "Validation of simultaneous PET emission and transmission scans," *J. Nucl. Med.*, vol. 32, pp. 154–60, 1991.

[19] Y. Pawitan, S. Kohlmyer, T. Lewellen, and F. O'Sullivan, "PET system calibration and attenuation correction," *IEEE Trans. Nucl. Sci.*, vol. 44, pp. 1249–53, 1997.

[20] P. E. Kinahan, D. W. Townsend, T. Beyer, and D. Sashin, "Attenuation correction for a combined 3D PET/CT scanner," *Med. Phys.*, vol. 25, pp. 2046–53, 1998.

[21] S. S. Gambhir, J. Czernin, J. Schwimmer, D. H. Silverman, R. E. Coleman, and M. E. Phelps, "A tabulated summary of the FDG PET literature," *J. Nucl. Med.*, vol. 42, pp. 1S–93S, 2001.

[22] M. Wagner, U. Seitz, A. Buck, B. Neumaier, S. Schultheiss, M. Bangerter, M. Bommer, F. Leithauser, E. Wawra, G. Munzert, and S. N. Reske, "3'-[18F]fluoro-3'-deoxythymidine ([18F]-FLT) as positron emission tomography tracer for imaging proliferation in a murine B-Cell lymphoma model and in the human disease," *Cancer Res.*, vol. 63, pp. 2681–7, 2003.

[23] B. Henriques de Figueiredo, C. Zacharatou, S. Galland-Girodet, J. Benech, H. De Clermont-Gallerande, F. Lamare, M. Hatt, L. Digue, E. De Mones Del Pujol, and P. Fernandez, "Hypoxia imaging with [18F]-FMISO-PET for guided dose escalation with intensity-modulated radiotherapy in head-and-neck cancers," *Strahlenther Onkol.*, 2014.

[24] S. M. Deng, B. Zhang, Y. W. Wu, W. Zhang, and Y. Y. Chen, "Detection of glioma recurrence by (1)(1)c-methionine positron emission tomography and dynamic susceptibility contrast-enhanced magnetic resonance imaging: a meta-analysis," *Nucl. Med. Commun.*, vol. 34, pp. 758–66, 2013.

[25] A. C. Kak and M. Slaney, *Principles of computerized tomographic imaging.* New York: IEEE Press, 1988.

[26] K. Oda, H. Toyama, K. Uemura, Y. Ikoma, Y. Kimura, and M. Senda, "Comparison of parametric FBP and OS-EM reconstruction algorithm images for PET dynamic study," *Ann. Nucl. Med.*, vol. 15, pp. 417–23, 2001.

[27] A. Rockmore and A. Macovski, "A maximum likelihood approach to emission image reconstruction from projections," *IEEE Trans. Nucl. Sci.*, vol. 23, pp. 1428–32, 1976.

[28] F. A. Haight, *Handbook of the Poisson Distribution.* John Wiley and Sons, 1967.

[29] A. P. Dempster, N. M. Laird, and D. B. Rubin, "Maximum likelihood from imcomplete data via the EM algorithm," *Joural of the royal statistical society*, vol. 39, pp. 1–38, 1977.

[30] K. Lange and R. Carson, "EM reconstruction algorithms for emission and transmission tomography," *J. Comput. Assist. Tomogr.*, vol. 8, pp. 306–16, 1984.

[31] R. E. Carson and K. Lange, "A statistical model for positron emission tomography: Comment," *J. Amer. Statist. Assn.*, vol. 80, pp. 20–22, 1985.

[32] H. M. Hudson and R. S. Larkin, "Accelerated image reconstruction using ordered subsets of projection data," *IEEE Trans. Med. Imag.*, vol. 13, pp. 601–9, 1994.

[33] A. Seret, "Number of iterations when comparing MLEM/OSEM with FBP," *J. Nucl. Med.*, vol. 45, p. 2125, 2004.

[34] R. Boellaard, A. van Lingen, and A. A. Lammertsma, "Experimental and clinical evaluation of iterative reconstruction (OSEM) in dynamic PET: quantitative characteristics and effects on kinetic modeling," *J. Nucl. Med.*, vol. 42, pp. 808–17, 2001.

[35] J. S. Liow and S. C. Strother, "Practical tradeoffs between noise, quantitation, and number of iterations for maximum likelihood-based reconstructions," *IEEE Trans. Med. Imag.*, vol. 10, pp. 563–571, 1991.

[36] E. Veklerov and J. Llacer, "Stopping rule for the MLE algorithm based on statistical hypothesis testing," *IEEE Trans. Med. Imag.*, vol. 6, no. 4, pp. 313–9, 1987.

[37] C. Schiepers, J. Nuyts, H.-M. Wu., and R. Verma, "PET with 18F-fluoride: effects of interative versus filtered backprojection reconstruction on kinetic modeling," *IEEE Trans. Nucl. Sci.*, vol. 44, pp. 1591–1593, 1997.

[38] S. C. Huang, "Role of kinetic modeling in biomedical imaging," *Journal of medical sciences (Taipei, Taiwan)*, vol. 28, pp. 57–63, 2008.

[39] M. F. Alf, M. I. Martic-Kehl, R. Schibli, and S. D. Kramer, "FDG kinetic modeling in small rodent brain PET: optimization of data acquisition and analysis," *EJNMMI Res.*, vol. 3, p. 61, 2013.

[40] M. Bentourkia, "Kinetic modeling of PET-FDG in the brain without blood sampling," *Comput. Med. Imaging Graph*, vol. 30, no. 8, pp. 447–51, 2006.

[41] M. Muzi, D. A. Mankoff, J. R. Grierson, J. M. Wells, H. Vesselle, and K. A. Krohn, "Kinetic modeling of 3'-deoxy-3'-fluorothymidine in somatic tumors: mathematical studies," *J. Nucl. Med.*, vol. 46, pp. 371–80, 2005.

[42] S. J. Kim, J. S. Lee, K. C. Im, S. Y. Kim, S. A. Park, S. J. Lee, S. J. Oh, D. S. Lee, and D. H. Moon, "Kinetic modeling of 3'-deoxy-3'-18F-fluorothymidine for quantitative cell proliferation imaging in subcutaneous tumor models in mice," *J. Nucl. Med.*, vol. 49, pp. 2057–66, 2008.

[43] C. Kratochwil, S. E. Combs, K. Leotta, A. Afshar-Oromieh, S. Rieken, J. Debus, U. Haberkorn, and F. L. Giesel, "Intra-individual comparison of (1)(8)F-FET and (1)(8)F-DOPA in PET imaging of recurrent brain tumors," *Neuro Oncol.*, vol. 16, pp. 434–40, 2014.

[44] H. Lundqvist, "Kinetic modelling of carbon-11 labelled methionine," in *PET Studies on Amino Acid Metabolism and Protein Synthesis*, ser. Developments in Nuclear Medicine. Springer Netherlands, 1993, vol. 23, pp. 175–82.

[45] R. N. Gunn, S. R. Gunn, and V. J. Cunningham, "Positron emission tomography compartmental models," *J. Cereb. Blood Flow Metab.*, vol. 21, no. 6, pp. 635–52, 2001.

[46] W. H. Press, S. A. Teukolsky, W. T. Vetterling, and B. P. Flannery, *Numerical recipes (3rd edition)*, 3rd ed. Cambridge university press, 2007, no. 65 – 75.

[47] J. Matthews, D. Bailey, P. Price, and V. Cunningham, "The direct calculation of parametric images from dynamic PET data using maximum-likelihood iterative reconstruction," *Phys. Med. Biol.*, vol. 42, pp. 1155–73, 1997.

[48] C. Tsoumpas, F. E. Turkheimer, and K. Thielemans, "Study of direct and indirect parametric estimation methods of linear models in dynamic positron emission tomography," *Med. Phys.*, vol. 35, pp. 1299–309, 2008.

[49] A. J. Reader, J. C. Matthews, F. C. Sureau, C. Comtat, and R. Trébossen, "Iterative kinetic parameter estimation within fully 4d PET image reconstruction," *IEEE Nucl. Sci. Symp. Conf.*, pp. 1752–1756, 2006.

[50] C. Tsoumpas, F. E. Turkheimer, and K. Thielemans, "A survey of approaches for direct parametric image reconstruction in emission tomography," *Med. Phys.*, vol. 35, pp. 3963–71, 2008.

[51] A. Rahmim, Y. Zhou, J. Tang, L. Lu, V. Sossi, and D. F. Wong, "Direct 4D parametric imaging for linearized models of reversibly binding PET tracers using generalized AB-EM reconstruction," *Phys. Med. Biol.*, vol. 57, pp. 733–55, 2012.

[52] G. Wang, L. Fu, and J. Qi, "Maximum a posteriori reconstruction of the Patlak parametric image from sinograms in dynamic PET," *Phys. Med. Biol.*, vol. 53, pp. 593–604, 2008.

[53] G. Wang and J. Qi, "Acceleration of the direct reconstruction of linear parametric images using nested algorithms," *Phys. Med. Biol.*, vol. 55, pp. 1505–17, 2010.

[54] J. Tang, H. Kuwabara, D. F. Wong, and A. Rahmim, "Direct 4D reconstruction of parametric images incorporating anato-functional joint entropy," *Phys. Med. Biol.*, vol. 55, pp. 4261–72, 2010.

[55] M. E. Kamasak, C. A. Bouman, E. D. Morris, and K. Sauer, "Direct reconstruction of kinetic parameter images from dynamic PET data," *IEEE Trans. Med. Imag.*, vol. 24, pp. 636–50, 2005.

[56] J. Yan, B. Planeta-Wilson, and R. E. Carson, "Direct 4-D PET list mode parametric reconstruction with a novel EM algorithm," *IEEE Trans. Med. Imag.*, vol. 31, pp. 2213–2223, 2012.

[57] J. Matthews, G. Angelis, F. Kotasidis, P. Markiewicz, and A. Reader, "Direct reconstruction of parametric images using any spatiotemporal 4D image based model and maximum likelihood expectation maximisation," in *IEEE Trans. Nucl. Sci. Symp. Conf.*, 2010, pp. 2435 – 2441.

[58] G. Wang and J. Qi, "Generalized algorithms for direct reconstruction of parametric images from dynamic PET data," *IEEE Trans. Med. Imag.*, vol. 28, pp. 1717–26, 2009.

[59] G. Wang and J. Qi, "An optimization transfer algorithm for nonlinear parametric image reconstruction from dynamic PET data." *IEEE Trans. Med. Imag.*, vol. 31, pp. 1977–88, 2012.

[60] G. Wang and J. Qi, "Direct estimation of kinetic parametric images for dynamic PET," *Theranostics*, vol. 3, pp. 802–15, 2013.

[61] A. J. Reader, F. C. Sureau, and C. Comtat, "Joint estimation of dynamic PET images and temporal basis functions using fully 4D ML-EM," *Phys. Med. Biol.*, vol. 5455, 2006.

[62] J. Yan, B. Planeta-Wilson, J.-D. Gallezot, and R. E. Carson, "Initial evaluation of direct 4D parametric reconstruction with human PET data," *IEEE Nucl. Sci. Symp. Conf.*, vol. 2009, pp. 2503–2506, 2009.

[63] G. I. Angelis, K. Thielemans, A. C. Tziortzi, F. E. Turkheimer, and C. Tsoumpas, "Convergence optimization of parametric MLEM reconstruction for estimation of Patlak plot parameters," *Comput. Med. Imag. Grap.*, vol. 35, pp. 407–16, 2011.

[64] E. Herranz, J. L. Herraiz, E. Vicente, S. Espana, M. Desco, J. J. Vaquero, and J. M. Udias, "Quantification limits of iterative PET reconstruction algorithms and improved estimation of kinetic constants," *ISBI*, pp. SA–PS1a.4, 2011.

[65] X. Cheng, J. Liu, J. Vogel, Z. Liu, N. Navab, S. I. Ziegler, and K. Shi, "Time-activity curve based sinogram decomposition for streak artifacts reduction in dynamic PET reconstruction," in *Computational Methods for Molecular Imaging (CMMI) Workshop - MICCAI 2014*, 2014, *in press.*

[66] P. J. Keall, L. B. Chock, R. Jeraj, J. V. Siebers, and R. Mohan, "Image reconstruction and the effect on dose calculation for hip prostheses," *Med. Dosim.*, vol. 28, pp. 113–7, 2003.

[67] W. Kalender, R. Hebel, and J. Ebersberger, "Reduction of CT artifacts caused by metallic implants," *Radiology*, vol. 164, pp. 576 – 7, 1987.

[68] P. P. Bruyant, J. Sau, and J.-J. Mallet, "Streak artifact reduction in filtered backprojection using a level line-based interpolation method," *J. Nucl. Med.*, vol. 41, pp. 1913 – 9, 2000.

[69] G. Wang, D. Snyder, J. O'Sullivan, and M. Vannier, "Iterative deblurring for CT metal artifact reduction," *IEEE Trans. Med. Imag.*, vol. 15, pp. 657 –664, 1996.

[70] J. August and T. Kanade, "Fast streaking artifact reduction in CT using constrained optimization in metal masks," in *MICCAI*, 2004, vol. 3217, pp. 1044–1045.

[71] L. K. Leong, R. L. Kruger, and M. K. O'Connor, "A comparison of the uniformity requirements for SPECT image reconstruction using FBP and OSEM techniques," *J. Nucl. Med. Technol.*, vol. 29, pp. 79–83, 2001.

[72] P. Razifar, M. Sandstrom, H. Schnieder, B. Langstrom, E. Maripuu, E. Bengtsson, and M. Bergstrom, "Noise correlation in PET, CT, SPECT and PET/CT data evaluated using autocorrelation function: a phantom study on data, reconstructed using FBP and OSEM," *BMC Med. Imaging*, vol. 5, p. 5, 2005.

[73] F. H. van Velden, R. W. Kloet, B. N. van Berckel, S. P. Wolfensberger, A. A. Lammertsma, and R. Boellaard, "Comparison of 3D-OP-OSEM and 3D-FBP reconstruction algorithms for High-Resolution Research Tomograph studies: effects of randoms estimation methods," *Phys. Med. Biol.*, vol. 53, pp. 3217–30, 2008.

[74] J. MacQueen, "Some methods for classification and analysis of multivariate observations," pp. 281–97, 1967.

[75] E. Krestyannikov, J. Tohka, and U. Ruotsalainen, "Segmentation of dynamic emission tomography data in projection space," in *CVAMIA*, 2006, vol. 4241, pp. 108–119.

[76] C. R. Vogel, *Computational methods for inverse problems.* Society for Industrial and Applied Mathematics, 2002.

[77] C. Chung, B. Driscoll, A. Gorjizadeh, W. Foltz, S. Lee, C. Menard, and C. Coolens, "Early detection of tumor response using 4d dce-ct and dce-mri in patients treated with radiosurgery for brain metastases," *Pract. Radiat. Oncol.*, vol. 3, pp. S17–8, 2013.

[78] C. A. Cuenod and D. Balvay, "Perfusion and vascular permeability: basic concepts and measurement in DCE-CT and DCE-MRI," *Diagn. Interv. Imaging.*, vol. 94, pp. 1187–204, 2013.

[79] H. Wang, J. Zhang, J. Tian, B. Qu, T. Li, Y. Chen, J. Liu, and S. Wang, "Using dual-tracer PET to predict the biologic behavior of human colorectal cancer," *J. Nucl. Med.*, vol. 50, pp. 1857–64, 2009.

[80] J.-W. Park, J. H. Kim, S. K. Kim, K. W. Kang, K. W. Park, J.-I. Choi, W. J. Lee, C.-M. Kim, and B. H. Nam, "A prospective evaluation of 18F-FDG and 11C-acetate PET/CT for detection of primary and metastatic hepatocellular carcinoma." *J. Nucl. Med.*, vol. 49, pp. 1912–21, 2008.

[81] N. Tomura, Y. Ito, H. Matsuoka, T. Saginoya, S. I. Numazawa, Y. Mizuno, and K. Watanabe, "PET findings of intramedullary tumors of the spinal cord using [18F] FDG and [11C] methionine," *American Journal of Neuroradiology*, 2012.

[82] M. Shiiba, K. Ishihara, G. Kimura, T. Kuwako, H. Yoshihara, H. Sato, Y. Kondo, S. Tsuchiya, and S. Kumita, "Evaluation of primary prostate cancer using 11C-methionine-PET/CT and 18F-FDG-PET/CT," *Annals of Nuclear Medicine*, vol. 26, pp. 138–45, 2012.

[83] J. Tian, X. Yang, L. Yu, P. Chen, J. Xin, L. Ma, H. Feng, Y. Tan, Z. Zhao, and W. Wu, "A multicenter clinical trial on the diagnostic value of dual-tracer PET/CT in pulmonary lesions using 3'-deoxy-3'-18F-fluorothymidine and 18F-FDG," *J. Nucl. Med.*, vol. 49, pp. 186–94, 2008.

[84] X. Cheng, N. Navab, S. Ziegler, and K. Shi, "Direct parametric image reconstruction of rapid multi-tracer PET," in *Medical Image Computing and Computer-Assisted Intervention MICCAI 2013*. Springer Berlin Heidelberg, 2013, vol. 8151, pp. 155–162.

[85] X. Cheng, Z. Li, Z. Liu, N. Navab, S.-C. Huang, U. Keller, S. I. Ziegler, and K. Shi, "Direct parametric image reconstruction in reduced parameter space for rapid multi-tracer PET imaging," *IEEE Trans. Med. Imag.*, *under revision*, 2014.

[86] R. A. Koeppe, D. M. Raffel, S. E. Snyder, E. P. Ficaro, M. R. Kilbourn, and D. E. Kuhl, "Dual-[11C]tracer single-acquisition positron emission tomography studies." *J. Cerebral Blood Flow Metabol.*, vol. 21, pp. 1480–92, 2001.

[87] D. Kadrmas and T. Rust, "Feasibility of rapid multitracer PET tumor imaging," *IEEE Trans. Nucl. Sci.*, vol. 52, pp. 1341 – 1347, 2005.

[88] D. J. Kadrmas, T. C. Rust, and J. M. Hoffman, "Single-scan dual-tracer FLT+FDG PET tumor characterization," *Phys. Med. Biol.*, vol. 58, pp. 429–49, 2013.

[89] S. C. Huang, R. E. Carson, E. J. Hoffman, D. E. Kuhl, and M. E. Phelps, "An investigation of a double-tracer technique for positron computerized tomography," *J. Nucl. Med.*, vol. 23, pp. 816–22, 1982.

[90] T. C. Rust and D. J. Kadrmas, "Rapid dual-tracer PTSM+ATSM PET imaging of tumour blood flow and hypoxia: a simulation study." *Phys. Med. Biol.*, vol. 51, pp. 61–75, 2006.

[91] A. D. Joshi, R. A. Koeppe, J. A. Fessler, and M. R. Kilbourn, "Signal separation and parameter estimation in noninvasive dual-tracer PET scans using reference-region approaches," *J. Cerebral Blood Flow Metabol.*, vol. 29, pp. 1346 – 1357, 2006.

[92] G. E. Fakhri, I. A. Sitek, and B. Guérin, "Simultaneous dual tracer PET using generalized factor analysis of dynamic sequences," *IEEE Nucl. Sci. Symp. Med. Imag. Conf.*, pp. 2128–30, 2006.

[93] N. F. Black, S. McJames, T. C. Rust, and D. J. Kadrmas, "Evaluation of rapid dual-tracer (62)Cu-PTSM + (62)Cu-ATSM PET in dogs with spontaneously occurring tumors." *Phys. Med. Biol.*, vol. 53, pp. 217–32, 2008.

[94] N. Black, S. McJames, and D. Kadrmas, "Rapid multi-tracer PET tumor imaging with 18F-FDG and secondary shorter-lived tracers," *IEEE Trans. Nucl. Sci.*, vol. 56, pp. 2750 –2758, 2009.

[95] F. Gao, H. Liu, Y. Jian, and P. Shi, "Dynamic dual-tracer PET reconstruction," *Information Processing in Medical Imaging*, vol. 21, pp. 38–49, 2009.

[96] J. Verhaeghe and A. Reader, "Accelerated PET water activation acquisition with signal separation methodology." *Med. Phys.*, pp. 2108–2111, 2013.

[97] D. J. Kadrmas and M. B. Oktay, "Generalized separable parameter space techniques for fitting 1K-5K serial compartment models." *Med. Phys.*, vol. 40, p. 072502, 2013.

[98] M. Oktay and D. Kadrmas, "Reduced parameter space formulations for fast and robust kinetic modeling," *JNM Meeting Abstracts*, vol. 53, p. 2292, 2012.

[99] Y. T. Hong and T. D. Fryer, "Kinetic modelling using basis functions derived from two-tissue compartmental models with a plasma input function: general principle and application to [18F]fluorodeoxyglucose positron emission tomography." *NeuroImage*, vol. 51, pp. 164–72, May 2010.

[100] G. A. F. Seber and C. J. Wild, *Nonlinear Regression*. John Wiley and Sons, 1989.

[101] D. L. Snyder, "Parameter estimation for dynamic studies in emission-tomography systems having list-mode data," *IEEE Trans. Nucl. Sci.*, vol. 31, pp. 925–931, 1984.

[102] A. A. Lammertsma and S. P. Hume, "Simplified reference tissue model for PET receptor studies." *NeuroImage*, vol. 4, pp. 153–8, 1996.

[103] Y. Ikoma, H. Watabe, M. Shidahara, M. Naganawa, and Y. Kimura, "PET kinetic analysis: error consideration of quantitative analysis in dynamic studies," *Annals of nuclear medicine*, vol. 22, pp. 1–11, 2008.

[104] R. Byrd, R. Schnabel, and G. Shultz, "A trust region algorithm for nonlinearly constrained optimization," *SIAM Journal on Numerical Analysis*, vol. 24, pp. 1152–1170, 1987.

[105] I. G. Zubal, C. R. Harrell, E. O. Smith, Z. Rattner, G. Gindi, and P. B. Hoffer, "Computerized three-dimensional segmented human anatomy," *Med. Phys.*, vol. 21, pp. 299–302, 1994.

[106] G. Delso, S. Fürst, B. Jakoby, R. Ladebeck, C. Ganter, S. G. Nekolla, M. Schwaiger, and S. I. Ziegler, "Performance measurements of the Siemens mMR integrated whole-body PET/MR scanner." *J. Nucl. Med.*, vol. 52, pp. 1914–22, 2011.

[107] S. Jan, G. Santin, D. Strul, S. Staelens, and K. Assi, "GATE : a simulation toolkit for PET and SPECT," *Phys. Med. Biol.*, vol. 4543, 2004.

[108] T. Hastie, R. Tibshirani, and J. Friedman, *The Elements of Statistical Learning: Data Mining, Inference, and Prediction.*, 2nd ed. Springer-Verlag, 2009.

[109] D. Feng, S. C. Huang, and X. Wang, "Models for computer simulation studies of input functions for tracer kinetic modeling with positron emission tomography," *Int. J. Biomed. Comput.*, vol. 32, pp. 95–110, 1993.

[110] W. Chen, T. Cloughesy, N. Kamdar, N. Satyamurthy, M. Bergsneider, L. Liau, P. Mischel, J. Czernin, M. E. Phelps, and D. H. Silverman, "Imaging proliferation in brain tumors with 18F-FLT PET: comparison with 18F-FDG," *J. Nucl. Med.*, vol. 46, no. 6, pp. 945–52, 2005.

[111] M. Beheshti, *PET/CT imaging in tracers beyond FDG, an issue of PET clinics*. Elsevier, 2014.

[112] E. J. Hoffman, S. C. Huang, and M. E. Phelps, "Quantitation in positron emission computed tomography: 1. effect of object size," *J. Comput. Assist. Tomogr.*, vol. 3, pp. 299–308, 1979.

[113] R. M. Kessler, J. Ellis, J. R., and M. Eden, "Analysis of emission tomographic scan data: limitations imposed by resolution and background," *J. Comput. Assist. Tomogr.*, vol. 8, pp. 514–22, 1984.

[114] T. H. Nobuyuki Kudomi, Hiroshi Watabe and H. Iida, "Separation of input function for rapid measurement of quantitative CMRO2 and CBF in a single PET scan with a dual tracer administration method." *Phys. Med. Biol.*, vol. 52, pp. 1893–908, 2007.

[115] J. Jiao, G. E. Searle, A. C. Tziortzi, C. A. Salinas, R. N. Gunn, and J. A. Schnabel, "Spatio-temporal pharmacokinetic model based registration of 4d PET neuroimaging data," *NeuroImage*, vol. 84, pp. 225 – 235, 2014.

[116] X. Cheng, C. Bayer, C.-A. Maftei, S. T. Astner, P. Vaupel, S. I. Ziegler, and K. Shi, "Preclinical evaluation of parametric image reconstruction of [^{18}F]FMISO PET: correlation with ex vivo immunohistochemistry," *Phys. Med. Biol.*, vol. 59, p. 347, 2014.

[117] D. M. Brizel, R. K. Dodge, R. W. Clough, and M. W. Dewhirst, "Oxygenation of head and neck cancer: changes during radiotherapy and impact on treatment outcome," *Radiother Oncol.*, vol. 53, pp. 113–117, 1999.

[118] P. Vaupel and A. Mayer, "Hypoxia in cancer: significance and impact on clinical outcome," *Cancer Metastasis Rev.*, vol. 26, no. 2, pp. 225–39, 2007.

[119] J. G. Rajendran, K. R. Hendrickson, A. M. Spence, M. Muzi, K. A. Krohn, and D. A. Mankoff, "Hypoxia imaging-directed radiation treatment planning," *Eur. J. Nucl. Med. Mol. Imaging*, vol. 33 Suppl 1, pp. 44–53, 2006.

[120] D. Thorwarth and M. Alber, "Implementation of hypoxia imaging into treatment planning and delivery," *Radiother Oncol.*, vol. 97, pp. 172–5, 2010.

[121] A. Lin and S. M. Hahn, "Hypoxia imaging markers and applications for radiation treatment planning," *Semin. Nucl. Med.*, vol. 42, pp. 343–52, 2012.

[122] I. Toma-Dasu and A. Dasu, "Quantitative hypoxia imaging for treatment planning of radiotherapy," *Adv. Exp. Med. Biol.*, vol. 812, pp. 143–8, 2014.

[123] J. A. Raleigh, D. P. Calkins-Adams, L. H. Rinker, C. A. Ballenger, M. C. Weissler, J. Fowler, W. C., D. B. Novotny, and M. A. Varia, "Hypoxia and

vascular endothelial growth factor expression in human squamous cell carcinomas using pimonidazole as a hypoxia marker," *Cancer Res.*, vol. 58, pp. 3765–8, 1998.

[124] J. J. Casciari, M. M. Graham, and J. S. Rasey, "A modeling approach for quantifying tumor hypoxia with [F-18]fluoromisonidazole PET time-activity data," *Med. Phys.*, vol. 22, pp. 1127–39, 1995.

[125] D. Thorwarth, S. M. Eschmann, F. Paulsen, and M. Alber, "A model of reoxygenation dynamics of head-and-neck tumors based on serial 18F-fluoromisonidazole positron emission tomography investigations," *Int. J. Radiat. Oncol. Biol. Phys.*, vol. 68, pp. 515–21, 2007.

[126] W. Wang, N. Y. Lee, J. C. Georgi, M. Narayanan, J. Guillem, H. Schoder, and J. L. Humm, "Pharmacokinetic analysis of hypoxia 18F-fluoromisonidazole dynamic PET in head and neck cancer," *J. Nucl. Med.*, vol. 51, pp. 37–45, 2010.

[127] Y. T. Hong, J. S. Beech, R. Smith, J. C. Baron, and T. D. Fryer, "Parametric mapping of [18F]fluoromisonidazole positron emission tomography using basis functions," *J. Cereb. Blood Flow Metab.*, vol. 31, pp. 648–57, 2011.

[128] S. M. Eschmann, F. Paulsen, M. Reimold, H. Dittmann, S. Welz, G. Reischl, H. J. Machulla, and R. Bares, "Prognostic impact of hypoxia imaging with 18F-misonidazole PET in non-small cell lung cancer and head and neck cancer before radiotherapy," *J. Nucl. Med.*, vol. 46, pp. 253–60, 2005.

[129] S. A. Nehmeh, N. Y. Lee, H. Schroder, O. Squire, P. B. Zanzonico, Y. E. Erdi, C. Greco, G. Mageras, H. S. Pham, S. M. Larson, C. C. Ling, and J. L. Humm, "Reproducibility of intratumor distribution of 18F-fluoromisonidazole in head and neck cancer," *Int. J. Radiat. Oncol. Biol. Phys.*, vol. 70, pp. 235–42, 2008.

[130] N. Y. Lee, J. G. Mechalakos, S. Nehmeh, Z. Lin, O. D. Squire, S. Cai, K. Chan, P. B. Zanzonico, C. Greco, C. C. Ling, J. L. Humm, and H. Schoder, "Fluorine-18-labeled fluoromisonidazole positron emission and computed tomography-guided intensity-modulated radiotherapy for head and neck cancer: a feasibility study," *Int. J. Radiat. Oncol. Biol. Phys.*, vol. 70, pp. 2–13, 2008.

[131] M. Nordsmark, J. G. Eriksen, V. Gebski, J. Alsner, M. R. Horsman, and J. Overgaard, "Differential risk assessments from five hypoxia specific assays: The basis for biologically adapted individualized radiotherapy in advanced head and neck cancer patients," *Radiother Oncol.*, vol. 83, pp. 389–97, 2007.

[132] D. Thorwarth, S. M. Eschmann, F. Paulsen, and M. Alber, "Hypoxia dose painting by numbers: a planning study," *Int. J. Radiat. Oncol. Biol. Phys.*, vol. 68, pp. 291–300, 2007.

[133] D. Thorwarth, S. M. Eschmann, F. Paulsen, and M. Alber, "A kinetic model for dynamic [18F]FMISO PET data to analyse tumour hypoxia," *Phys. Med. Biol.*, vol. 50, pp. 2209–24, 2005.

[134] H. Cho, E. Ackerstaff, S. Carlin, M. E. Lupu, Y. Wang, A. Rizwan, J. O'Donoghue, C. C. Ling, J. L. Humm, P. B. Zanzonico, and J. A. Koutcher, "Noninvasive multimodality imaging of the tumor microenvironment: registered dynamic magnetic resonance imaging and positron emission tomography studies of a preclinical tumor model of tumor hypoxia," *Neoplasia*, vol. 11, pp. 247–59, 2009.

[135] E. G. Troost, P. Laverman, M. E. Philippens, J. Lok, A. J. van der Kogel, W. J. Oyen, O. C. Boerman, J. H. Kaanders, and J. Bussink, "Correlation of [18F]FMISO autoradiography and pimonidazole [corrected] immunohistochemistry in human head and neck carcinoma xenografts," *Eur. J. Nucl. Med. Mol. Imaging*, vol. 35, pp. 1803–11, 2008.

[136] M. Busk, M. R. Horsman, S. Jakobsen, K. V. Hansen, J. Bussink, A. van der Kogel, and J. Overgaard, "Can hypoxia-PET map hypoxic cell density heterogeneity accurately in an animal tumor model at a clinically obtainable image contrast?" *Radiother Oncol.*, vol. 92, pp. 429–36, 2009.

[137] L. J. Dubois, N. G. Lieuwes, M. H. Janssen, W. J. Peeters, A. D. Windhorst, J. C. Walsh, H. C. Kolb, M. C. Ollers, J. Bussink, G. A. van Dongen, A. van der Kogel, and P. Lambin, "Preclinical evaluation and validation of [18F]HX4, a promising hypoxia marker for PET imaging," *Proc. Natl. Acad. Sci. USA*, vol. 108, pp. 14 620–5, 2011.

[138] R. M. Bartlett, B. J. Beattie, M. Naryanan, J. C. Georgi, Q. Chen, S. D. Carlin, G. Roble, P. B. Zanzonico, M. Gonen, J. O'Donoghue, A. Fischer, and J. L. Humm, "Image-guided pO2 probe measurements correlated with parametric images derived from 18F-Fluoromisonidazole small-animal PET data in rats," *J. Nucl. Med.*, vol. 53, pp. 1608–15, 2012.

[139] K. Shi, C. A. Maftei, C. Bayer, S. Astner, F. C. Gaertner, P. Vaupel, M. Schwaiger, S. C. Huang, and S. Ziegler, "Quantitative analysis of [18F]FMISO PET for tumor hypoxia: Correlation with results using immunohistochemistry," in *JNM Meeting Abstract*, vol. 53, 2012, p. 216.

[140] C. S. Patlak and R. G. Blasberg, "Graphical evaluation of blood-to-brain transfer constants from multiple-time uptake data. Generalizations," *J. Cereb. Blood Flow Metab.*, vol. 5, pp. 584–90, 1985.

[141] C. A. Maftei, K. Shi, C. Bayer, S. T. Astner, and P. Vaupel, "Comparison of (immuno-)fluorescence data with serial [18F]Fmiso PET/CT imaging for assessment of chronic and acute hypoxia in head and neck cancers," *Radiother Oncol.*, vol. 99, pp. 412–7, 2011.

[142] C. A. Maftei, C. Bayer, K. Shi, and P. Vaupel, "Intra- and intertumor heterogeneities in total, chronic, and acute hypoxia in xenografted squamous cell carcinomas." *Strahlenther Onkol.*, vol. 188, pp. 606–15, 2012.

[143] A. A. Dima, J. T. Elliott, J. J. Filliben, M. Halter, A. Peskin, J. Bernal, M. Kociolek, M. C. Brady, H. C. Tang, and A. L. Plant, "Comparison of segmentation algorithms for fluorescence microscopy images of cells," *Cytometry A*, vol. 79, pp. 545–59, 2011.

[144] K. P. Wong, W. Sha, X. Zhang, and S. C. Huang, "Effects of administration route, dietary condition, and blood glucose level on kinetics and uptake of [18F]FDG in mice," *J. Nucl. Med.*, vol. 52, pp. 800–7, 2011.

[145] G. Z. Ferl, X. Zhang, H. M. Wu, M. C. Kreissl, and S. C. Huang, "Estimation of the 18F-FDG input function in mice by use of dynamic small-animal PET and minimal blood sample data," *J. Nucl. Med.*, vol. 48, pp. 2037–45, 2007.

[146] M. H. Cherk, S. S. Foo, A. M. Poon, S. R. Knight, C. Murone, A. T. Papenfuss, J. I. Sachinidis, T. H. Saunder, G. J. O'Keefe, and A. M. Scott, "Lack of correlation of hypoxic cell fraction and angiogenesis with glucose metabolic rate in non-small cell lung cancer assessed by 18F-Fluoromisonidazole and 18F-FDG PET," *J. Nucl. Med.*, vol. 47, pp. 1921–6, 2006.

[147] J. G. Rajendran, D. L. Schwartz, J. O'Sullivan, L. M. Peterson, P. Ng, J. Scharnhorst, J. R. Grierson, and K. A. Krohn, "Tumor hypoxia imaging with [F-18] fluoromisonidazole positron emission tomography in head and neck cancer," *Clin. Cancer Res.*, vol. 12, pp. 5435–41, 2006.

[148] P. Vera, P. Bohn, A. Edet-Sanson, A. Salles, S. Hapdey, I. Gardin, J. F. Menard, R. Modzelewski, L. Thiberville, and B. Dubray, "Simultaneous positron emission tomography (PET) assessment of metabolism with 18F-fluoro-2-deoxy-d-glucose (FDG), proliferation with 18F-fluoro-thymidine (FLT), and hypoxia with 18fluoro-misonidazole (F-miso) before and during radiotherapy in patients with non-small-cell lung cancer (NSCLC): a pilot study," *Radiother Oncol.*, vol. 98, pp. 109–16, 2011.

[149] C. Tsoumpas, S. Member, F. Turkheimer, and K. Thielemans, "Convergence properties of algorithms for direct parametric estimation of linear models in dynamic PET," *IEEE Nucl. Sci. Symp. Conf.*, pp. 3034–3037, 2007.

[150] K. Lange, "Convergence of EM image reconstruction algorithms with Gibbs smoothing," *IEEE Trans. Med. Imag.*, vol. 9, pp. 439–46, 1990.

[151] J. A. Fessler and W. L. Rogers, "Spatial resolution properties of penalized-likelihood image reconstruction: space-invariant tomographs," *IEEE Trans. Image Process*, vol. 5, pp. 1346–58, 1996.

[152] C. A. Maftei, C. Bayer, K. Shi, S. T. Astner, and P. Vaupel, "Quantitative assessment of hypoxia subtypes in microcirculatory supply units of malignant tumors using (immuno-)fluorescence techniques," *Strahlenther Onkol.*, vol. 187, pp. 260–6, 2011.

[153] L. Dubois, W. Landuyt, K. Haustermans, P. Dupont, G. Bormans, P. Vermaelen, P. Flamen, E. Verbeken, and L. Mortelmans, "Evaluation of hypoxia in an experimental rat tumour model by [(18)F]fluoromisonidazole PET and immunohistochemistry," *Br. J. Cancer*, vol. 91, pp. 1947–54, 2004.

[154] C. A. Johnson, J. Seidel, R. E. Carson, W. R. Gandler, A. Sofer, M. V. Green, and M. E. Daube-Witherspoon, "Evaluation of 3D reconstruction algorithms for a small animal PET camera," *IEEE Trans. Nucl. Sci.*, vol. 44, pp. 1303–8, 1997.

[155] P. E. Kinahan and J. S. Karp, "Analytic 3D image reconstruction using all detected event," *IEEE Trans. Nucl. Sci.*, vol. 36, pp. 964–8, 1988.